

# **POLINSAR BASED SCATTERING INFORMATION AND PHYSICAL PROPERTY RETRIEVAL OF VEGETATION**

Thesis submitted to the Andhra University, Visakhapatnam  
in partial fulfillment of the requirement for the award of  
Master of Technology in Remote Sensing and GIS



## **Submitted By:**

Unmesh Govind Khati

## **Supervised By:**

Mr. Shashi Kumar  
Scientist SD  
Photogrammetry and Remote Sensing  
Department

Ms. Shefali Agrawal  
Scientist SG & Head  
Photogrammetry and Remote Sensing  
Department



**Indian Institute of Remote Sensing, ISRO,  
Dept. of Space, Govt. of India, Dehradun – 248001  
Uttarakhand, India**

**August, 2014**

## *Acknowledgement*

This thesis arose as a part of M.Tech project work carried out at Indian Institute of Remote Sensing. This thesis would not have materialized without the guidance and support of many people. Their contribution in the making of this thesis deserves a special mention. This is a humble acknowledgement to convey my gratitude to them all.

I am thankful to my supervisor, Mr. Shashi Kumar, Scientist SD', PRSD, IIRS. This research work would not have been possible without his valuable guidance, support and motivation throughout the duration of the research work. He gave me the freedom to do mistakes and learn from them. His patience and care in supporting me cannot be valued.

I am thankful to my supervisor Ms. Shefali Agrawal, Scientist SG', Head PRSD and M.Tech Course Director, IIRS for her valuable guidance, expert advice and deep insight. Her guidance has not only helped me in my research but also helped me develop better qualities as an individual.

I am thankful to Mr. P.L.N. Raju, Group Director, RSGG, IIRS, Dr. S.K. Saha, Dean (Academics) and Dr. Y.V.N. Krishnamurthy, Director, IIRS for their valuable advices and insightful observations during the intermediate presentations which provided direction for mid-course corrections during the course of the research work. I am also grateful to them for providing an energetic and conducive research environment at IIRS.

I would like to thank the Librarian, IIRS for providing all the necessary research materials and books required during the duration of course. I would also like to thank Mr. Kailash and Mr. Srinivasa for their help and assistance in library.

I submit my sincere thanks to Principal Chief Conservator of Forests, Uttarakhand for providing the necessary forest data and permitting me to carry out the field work for the project.

I am obliged to Dr. R.S. Pande, Vice-Principal, SRKNEC, my *Alma mater* for his support during this project and for extending the facilities at SRKNEC for facilitating my research work.

I fall short of words to thank my parents Dr. G. Y. Khati and Dr. Mrs. V. G. Khati for supporting me through this despite great difficulties. Without their moral and mental support and guidance this research would not be possible. I also thank my loving brother Kaustubh, who is always available for me through good and bad times. My family is my greatest support and source of inspiration.

I am especially thankful to Lt. Col. Sanjay Mohan and Mr. Manoj Semwal, Scientist CSIR. Fruitful discussions with them throughout the duration of my stay at IIRS are highly acknowledged. Their continued guidance and advice have helped during the course work. Special thank is due to Mr. Aniruddha Deshmukh and Vinayak for all the good memories.

Friends are a great support system in itself. I thank Amit, Parag, and my seniors Vimal and Shikhar for providing a great atmosphere in the hostel. Their enthusiasm in exploring this beautiful city and its bountiful surrounding helped unwind after a hectic work schedule. I express my thanks to my friends Shashi, Piyush, Shishant, Ankur Amreesh, Sai, Rohit, Mayank, Akansha, Ponraj, Yeshu and Joyson and juniors, Rigved and Vikrant for all the good times spent during the stay at IIRS.

Lastly, I offer my regards to all those who knowingly and unknowingly have supported me during the completion of this research project.

**Unmesh Khati**

**CERTIFICATE**

This is to certify that **Mr. Unmesh Govind Khati** has carried out the dissertation entitled **“PolInSAR based scattering information and physical property retrieval of vegetation”** in partial fulfillment of the requirements for the award of **M.Tech in Remote Sensing and GIS**. This work has been carried out under the supervision of **Mr. Shashi Kumar**, Scientist ‘SD’ and **Ms. Shefali Agrawal**, Scientist ‘SG’, Photogrammetry and Remote Sensing Department, Indian Institute of Remote Sensing, ISRO, Dehradun, Uttarakhand, India.

Mr. Shashi Kumar  
Project Supervisor  
Photogrammetry and Remote Sensing  
Department  
IIRS, Dehradun

Ms. Shefali Agrawal  
Project Supervisor and Head  
Photogrammetry and Remote Sensing  
Department  
IIRS, Dehradun

Dr. S. K. Saha  
Group Director ER & SS Group & Dean  
(Academics)  
IIRS, Dehradun

Dr. Y. V. N. Krishna Murthy  
Director  
IIRS, Dehradun

## **Declaration**

I, *Unmesh Govind Khati*, hereby declare that this dissertation entitled “*PolInSAR based scattering information and physical property retrieval of vegetation*” submitted to Andhra University, Visakhapatnam in partial fulfilment of the requirements for the award of *M.Tech in Remote Sensing and GIS*, is my own work and that to the best of my knowledge and belief. It is a record of original research carried out by me under the guidance and supervision of **Mr. Shashi Kumar**, Scientist ‘SD’ and **Ms. Shefali Agrawal**, Scientist ‘SG’, Photogrammetry and Remote Sensing Department, Indian Institute of Remote Sensing, ISRO, Dehradun. It contains no material previously published or written by another person nor material which to a substantial extent nor material which to a substantial extent has been accepted for the award of any other degree or diploma of the university or other institute of higher learning, except where due acknowledgement has been made in the text.

Place: Dehradun

Mr. Unmesh Govind Khati

Date:

*Dedicated to my family*

## **Abstract**

---

The thesis is aimed at two major studies – to analyze the effect of shift in polarization orientation angle on multi-frequency PolSAR data, and to examine the application of PolInSAR techniques for the scattering information retrieval and height estimation of forested areas. Polarization orientation angle shift on airborne SAR data has been researched leading to analyses of its effects on coherence matrix and topographic analysis. The analysis of the effect of orientation angle shift on space-borne PolSAR data, is a novel study presented in this thesis. Important observations are drawn on the effect of the orientation angle shift on space-borne PolSAR data, which differ from those earlier observed for airborne data. The effect is demonstrated using space-borne data acquired by ALOS PALSAR, RADARSAT-2 and TERRASAR-X platforms. Orientation angle shift compensation is also applied, for the first time, to PolInSAR data. A preliminary analysis is presented in the present work, on the effects of orientation angle shift on PolInSAR based scattering information and also on the estimated forest stand height.

PolInSAR data is utilized for estimation of forest stand height. Two techniques – Coherence Amplitude Inversion and Three Stage Inversion – for forest height estimation are discussed, compared and validated. These techniques allow estimation of forest stand height and true ground topography. Complex coherences are calculated in all the possible polarization combinations. Ground-to-volume scattering ratio is used for accurate estimation of polarizations which represent surface and top of canopy scattering. The accuracy of the forest height estimated is assessed using ground based measurements. The inability of the forest height estimation techniques in identification of forested areas and overestimation of height in non-forested regions is also addressed through this thesis. Based on coherence and backscatter approach, a threshold based technique for forested area identification and accurate height estimation in non-forested regions is introduced.

The performance of the forest height estimation techniques and the coherence and backscatter based approach are demonstrated using fully polarimetric single baseline data acquired over the tropical forests of Barkot and Thano range, using RADARSAT-2 at C-band.

## **TABLE OF CONTENTS**

---

<b>1. INTRODUCTION</b>	<b>1</b>
1.1 MOTIVATION	1
1.2 INNOVATION AIMED AT	2
1.3 OBJECTIVES OF THE THESIS	2
1.4 RESEARCH QUESTIONS	3
1.5 SYNOPSIS	3
<b>2. LITERATURE REVIEW AND BACKGROUND</b>	<b>3</b>
2.1 BASICS OF ELECTROMAGNETICS	4
2.2 POLARIZATION ELLIPSE	5
2.3 SCATTERING MATRIX	6
2.4 POLSAR DECOMPOSITION TECHNIQUES	8
2.5 POLARIZATION BASIS TRANSFORMATIONS	9
2.6 POLARIZATION ORIENTATION ANGLE SHIFT	11
2.7 POLARIMETRIC SAR INTERFEROMETRY (POLINSAR)	13
2.8 VEGETATION HEIGHT ESTIMATION USING POLINSAR	16
<b>3. STUDY AREA AND MATERIALS</b>	<b>18</b>
3.1 STUDY AREA	18
3.2 MATERIALS	19
3.2.1 SATELLITE DATA	19
3.2.2 FIELD SURVEY	20
<b>4. METHODOLOGY</b>	<b>25</b>
4.1 ORIENTATION ANGLE SHIFT	25
4.1.1 ESTIMATION OF INDUCED SHIFT IN ORIENTATION ANGLE AND ITS COMPENSATION	25
4.1.2 EFFECT OF ORIENTATION ANGLE SHIFT ON POLINSAR DATA AND HEIGHT RETRIEVAL	26
4.2 POLINSAR BASED TREE HEIGHT ESTIMATION	26
4.3 IMPROVED ‘THREE STAGE INVERSION’ TECHNIQUE FOR VEGETATION HEIGHT ESTIMATION	30
<b>5. RESULTS AND DISCUSSION</b>	<b>34</b>
5.1. EFFECT OF SHIFT IN POA ON MULTI-FREQUENCY SAR DATA	34
5.1.1 POLARIZATION ORIENTATION ANGLE (POA) SHIFT	35
5.1.2 YAMAGUCHI DECOMPOSITION	36

5.1.3 EFFECT OF SHIFT IN POA ON YAMAGUCHI DECOMPOSED PRODUCTS	37
5.2. POLARIMETRIC INTERFEROMETRIC SYNTHETIC APERTURE RADAR (POLINSAR)	43
5.2.1 CO-REGISTRATION OF SCATTERING MATRICES	43
5.2.2 ESTIMATION OF BASELINE	44
5.2.3 GENERATION OF VERTICAL WAVENUMBER $k_z$	45
5.2.4 MULTI-LOOKING AND GENERATION OF $T_6$ MATRIX	45
5.2.5 CALCULATION OF COMPLEX COHERENCE IN DIFFERENT POLARIZATION BASIS	46
5.2.6 COHERENCE AS A FUNCTION OF GROUND-TO-VOLUME SCATTERING RATIO	53
5.3 ESTIMATION OF FOREST STAND HEIGHT	56
5.3.1 DEM DIFFERENCING HEIGHT	56
5.3.2 COHERENCE AMPLITUDE INVERSION HEIGHT	57
5.3.3 THREE STAGE INVERSION TECHNIQUE	60
5.3.4 IMPROVED THREE STAGE INVERSION TECHNIQUE	65
<b>6. CONCLUSION AND RECOMMENDATIONS</b>	<b>70</b>
CONCLUSIONS	70
RECOMMENDATIONS	73
<b>REFERENCES</b>	<b>I</b>
<b>APPENDICES</b>	<b>VI</b>
APPENDIX 1: PLOT WISE FIELD MEASURED TREE HEIGHT	VI
APPENDIX 2: ‘THREE STAGE INVERSION’ TECHNIQUE	IX
APPENDIX 3: EFFECT OF POA SHIFT ON POLINSAR DATA	XII
A3.1 EFFECT ON COMPLEX COHERENCES IN DIFFERENT POLARIZATION BASIS	XIII
A3.2 EFFECT OF DEORIENTATION ON ESTIMATED FOREST HEIGHT	XVI
APPENDIX 4: PAULI DECOMPOSED IMAGES OF MULTI-FREQUENCY POLSAR DATA	XVIII
APPENDIX 5: THREE DIMENSIONAL VIEW OF ESTIMATED HEIGHT	XX

## List of Figures

Figure 2.1 Graphical representation of the Polarization Ellipse. ‘A’ is the amplitude of the ellipse given by Eq. (2.5), $\theta$ is the orientation angle defined by Eq. (2.6) and $\tau$ is the ellipticity also called as ellipse aperture given in Eq. (2.7) .....	6
Figure 2.2 Poincare Sphere depicting all the possible polarization basis. CL and CR are the left and right circular polarization basis respectively. The elliptical and linear polarizations can also be observed.....	10
Figure 2.3 Pictorial representation of the three dominant scattering mechanisms occurring in forest-stand and the equivalent Random Volume Over Ground Scattering model.....	16
Figure 3.1 Study Area - Barkot and Thano Forest Range. The figure presents LISS IV acquired FCC image of the study area. The forest range in the center of the image is the Barkot forest range. Thano forest range lies to the north of the Barkot forest range.....	18
Figure 3.2 Forest Type map for Barkot and Thano forest range. Sal species dominates the forest ranges. Teak species dominates the Dry Mixed Miscellaneous forest regions and the other major species are the Khair and Sisoo. ....	19
Figure 3.3 Left: Barkot Forest Range. Right: Forest stand comprising chiefly of Sal trees. ....	21
Figure 3.4 Pie chart showing the area wise distribution of different species in the study area. ....	21
Figure 3.5 Left: Field plots of 12.5 meter each were plotted as shown. The GPS location was obtained using Trimble Juno SB handheld GPS. The average positional error observed is 8 meter as depicted using the circle. Right: The field height measurements in each plot. The measurements are noted for the highest tree – H_100, average tree height – H_avg and the understory height – H_under of the plot. ....	22
Figure 3.6 Field work and in situ data collection. ....	23
Figure 3.7a Field Photographs depicting the understory in forest area. ....	23
Figure 4.1 Methodology flow chart for Forest-stand height retrieval and study of POA shift on PolInSAR data. ....	27
Figure 4.2 Flow chart for the ‘Improved Three Stage Inversion Technique’ for accurate estimation of height in forested and non-forested regions. The thresholds for Coherence and Backscatter are $t_1$ and $t_2$ respectively.....	31
Figure 4.3 Span coherence values for different land cover regions. The value for forested regions $\in(0.2,0.8)$ , water regions $\in(0.1,0.6)$ and dry land areas $\in(1.0,2.4)$ .....	32
Figure 4.4 Threshold for backscattering power. The water and non-water regions result in distinctly different backscattering values. For water regions the backscattering power lies between (0, 0.1). For non-water, i.e. Forest and Urban areas, the backscatter power is more than 0.3.....	33
Figure 5.1 Left: Google Earth Imagery of Manali, Himachal Pradesh. Right: Three major areas of interest – Urban city region, Parks and the River Beas.....	34
Figure 5.2 Histograms and Statistics of the POA induced in multi-frequency data sets.....	35
Figure 5.3 Yamaguchi decomposed color coded images for three SAR sensors before orientation angle compensation. ....	36
Figure 5.4 Comparison of Yamaguchi decomposed products Pre- and Post-orientation angle compensation. Color coding used- Double-bounce scattering– red; Volume scattering– green; Surface scattering – blue. ....	38
Figure 5.5 Effect of Orientation Angle Shift on double-bounce Scattering Power. Sample points 1-50 belong to River area; 51-100 to Urban region; 101-150 to Park region. As shown the double-bounce scattering consistently increases after de-orientation.....	39
Figure 5.6 Effect of Orientation Angle Shift on Surface Scattering Power. Sample points 1-50 belong to River area; 51-100 to Urban region; 101-150 to Park region. Scattering power below -50dB is considered as noise and ignored.....	40

Figure 5.7 Effect of Orientation Angle Shift on Volume Scattering Power. Sample points 1-50 belong to River area; 51-100 to Urban region; 101-150 to Park region. The volume scattering power shows appreciable decrease post-compensation. .... 41

Figure 5.8 Effect of Orientation Angle Shift on Helix Scattering Power. Sample points 1-50 belong to River area; 51-100 to Urban region; 101-150 to Park region. The helix scattering power shows appreciable decrease post-compensation. The scattering power for TERRASAR-X is below -100dB and considered noise and ignored for analysis. .... 42

Figure 5.9 Pauli basis images of two acquisitions. .... 43

Figure 5.10 Shift in rows after co-registration. A) The co-registered slave image. The black rows at the top are the rows which are shifted after co-registration with the master image. B) A zoomed portion of the top left corner can be viewed showing the 88 rows shift leading to black portion at the top. .... 44

Figure 5.11 Pauli basis images after multi-looking and generation of [T6] matrix. The images for two acquisitions A and B are presented above. .... 46

Figure 5.12 Coherence maps in H, V-polarization basis. .... 47

Figure 5.13 Coherence histograms in H, V-polarization basis. Blue – HH; Green – HV; Black – VV. .... 47

Figure 5.14 Color composite coherence map in H, V-polarization. Red – HH; Green – HV; Blue – VV. .... 48

Figure 5.15 Coherence maps in Pauli-polarization basis. .... 49

Figure 5.16 Coherence histograms in Pauli-polarization basis. Blue – HH+VV; Green – HV+VH; Black – HH-VV. .... 49

Figure 5.17 Color composite coherence map in Pauli-polarization basis. Red – HH-VV; Green – HV+VH; Blue – HH+VV. .... 50

Figure 5.18 Coherence maps in Circular-polarization basis. .... 51

Figure 5.19 Coherence histograms in Circular-polarization basis. Blue – LL; Green – LR; Black – RR. .... 51

Figure 5.20 Color composite coherence map in Circular-polarization basis. Red –LL; Green – LR; Blue – RR. .... 52

Figure 5.21 Coherence maps in Optimal-polarization basis. .... 52

Figure 5.22 Coherence histograms in Optimal (Opt)-polarization basis. Blue – Opt1; Green – Opt2; Black – Opt3. .... 53

Figure 5.23 Color composite coherence map in Optimal-polarization basis. Red –Opt1; Green – Opt2; Blue – Opt3. .... 53

Figure 5.24 Forest region - scatter plots of ground-to-volume scattering ratio with coherence in different polarizations. The x-axis denotes the ground-to-volume scattering ratio in dB scale and the y-axis has coherences in different polarizations. The red-to-blue colors define the density of the points with red representing high density and blue representing low density. .... 54

Figure 5.25 DEM Difference height. Top DEM: HV; Bottom DEM: HH+VV. .... 56

Figure 5.26 Coherence Amplitude Inversion height with using HV+VH polarization for volume dominated coherence and HH+VV polarization for surface coherence. .... 57

Figure 5.27 Coherence Amplitude Inversion height histogram. The descriptive statistics are provided on the right side. .... 58

Figure 5.28 Histogram of Field measured forest height. .... 58

Figure 5.29 Histogram of derived forest height using Coherence Amplitude inversion technique. .... 59

Figure 5.30 Box plot plot of the Coherence amplitude inversion forest height and field measured tree height. .... 59

Figure 5.31 Scatter plot for the height derived using the Coherence Amplitude Inversion Technique. The solid line is the line at 45° and the dotted line is the best fit line through the plots. The R<sup>2</sup> value is low at 0.1159 corresponding to a correlation of 0.34. .... 60

Figure 5.32 Forest Stand Height estimated using ‘Three Stage Inversion’ technique. .... 61

Figure 5.33 Histogram of ‘Three Stage Inversion’ technique derived Forest Height. .... 62

Figure 5.34 Box plot of the ‘Three Stage Inversion’ technique derived Forest height and the field measured tree height ..... 62

Figure 5.35 Scatter Plot - Three Stage Inversion Height vs Field Measured Average height (H-avg). The solid line is the line at 45° and the dotted line is the best fit line through the plots. The R2 value is 0.3877 corresponding to a correlation of 0.623. .... 63

Figure 5.36 Scatter plot for ‘Three Stage Inversion’ technique after excluding the outliers ..... 65

Figure 5.37 Forest Height Map generated using ‘Three Stage Inversion’ technique. Transect-1 is at the top of the image, passes through dry-river. Transect-2 at the center of the images passes through urban regions and River Ganga. .... 66

Figure 5.38 Transect-1 Height Profile ..... 66

Figure 5.39 Transect-2 Height Profile ..... 66

Figure 5.40 Forest Height Map generated using Improved ‘Three Stage Inversion’ technique. The coherence threshold is applied. Transect-1 is at the top of the image, passes through dry-river. Transect-2 at the center of the images passes through urban regions and River Ganga. .... 67

Figure 5.41 Transect-1 Height Profile ..... 67

Figure 5.42 Transect-2 Height Profile ..... 67

Figure 5.43 Forest Height Map generated using Improved ‘Three Stage Inversion’ technique. Coherence and Backscatter threshold are applied. Transect-1 is at the top of the image, passes through dry-river. Transect-2 at the center of the images passes through urban regions and River Ganga. .... 68

Figure 5.44 Height Profile Transect-1 ..... 68

Figure 5.45 Height Profile Transect-2 ..... 68

Figure 5.46 Three-dimensional representation of the height difference between effective phase scattering centers of the Barkot forest area. .... 69

Figure A2.1 Schematic representation of the two layer model. .... IX

Figure A2.2 Representation of the ‘Three Stage Inversion’ technique (Cloude and Papathanassiou, 2003). .... X

Figure A2.3 An example of the coherences plotted on the complex plane. .... XI

Figure A2.4 Geometrical interpretation of the height and extinction estimation (Cloude and Papathanassiou, 2003). .... XII

Figure A3.1 Comparative color composite Coherence map in Linear (H,V) polarization basis. A. Shows coherence map pre-OAS compensation and B. shows coherence map post-OAS compensation. The color composition is Red-HH coherence; Green-HV coherence and Blue-VV coherence. . VIII

Figure A3.2 Comparative color composite Coherence map in Pauli polarization basis. A. Shows coherence map pre-OAS compensation and B. shows coherence map post-OAS compensation. The color composition is Red-HH-VV coherence; Green-HV+VH coherence and Blue-HH-VV coherence. .... IX

Figure A3.3 Comparative color composite Coherence map in Circular (L,R) polarization basis. A. Shows coherence map pre-OAS compensation and B. shows coherence map post-OAS compensation. The color composition is Red-LL coherence; Green-LR coherence and Blue-RR coherence. .... IX

Figure A3.4 Field photographs of dry riverbed. The figure on the left shows the boulders in the riverbed. On the right the dry riverbed is seen in the backdrop of the foothills of the Himalayas. .... XI

Figure A4.1 Pauli decomposed color composite sar images in L-, C-, and X-band ..... XIII

Figure A5.1 3D representation of Forest Height. .... XIV

Figure A5.2 Three dimensional view of Bakot forest and Rishikesh City. The LISS IV imagery is overlaid on PolInSAR based forest height and SRTM DEM height ..... XV

## **List of Tables**

<i>Table 2.1 Polarization Ellipse parameters for some common canonical polarization states. ....</i>	<i>10</i>
<i>Table 3.1 Data Characteristics of Multi-frequency PolSAR Data .....</i>	<i>20</i>
<i>Table 3.2 Data Characteristics of PolInSAR Data Pair .....</i>	<i>20</i>
<i>Table 3.3 Criterion RD1000 Laser Dendrometer Specifications .....</i>	<i>22</i>
<i>Table 5.1 Change in double-bounce scattering power post-POA compensation.....</i>	<i>39</i>
<i>Table 5.2 Change in surface scattering power post-POA compensation.....</i>	<i>40</i>
<i>Table 5.3 Change in volume scattering power post-POA compensation.....</i>	<i>41</i>
<i>Table 5.4 Change in helix scattering power post-POA compensation. ....</i>	<i>42</i>
<i>Table 5.5 Co-registration: Shift in rows and columns .....</i>	<i>43</i>
<i>Table 5.6 Baseline Estimation.....</i>	<i>44</i>
<i>Table 5.7 Statistics – Coherence amplitude inversion height and Field height (H_avg).....</i>	<i>58</i>
<i>Table 5.8 Test of Normality of Data for coherence amplitude inversion height and Field height (H_avg) .....</i>	<i>59</i>
<i>Table 5.9 Accuracy assessment results for coherence amplitude inversion height.....</i>	<i>60</i>
<i>Table 5.10 Statistics – Three Stage inversion height and Field height (H_avg).....</i>	<i>61</i>
<i>Table 5.11 Test of Normality of Data for Three Stage Inversion height and Field Height (H_avg) .....</i>	<i>62</i>
<i>Table 5.12 Accuracy Assessment Results for ‘Three Stage Inversion’ technique height.....</i>	<i>62</i>
<i>Table 5.13 Groups of Plots with high error in height estimation.....</i>	<i>63</i>
<i>Table 5.14 Accuracy assessment after excluding the outlier plots. ....</i>	<i>64</i>
<i>Table A1.0.1 Plot wise field measured tree height .....</i>	<i>VI</i>
<i>Table A3.1 Change in Coherence pattern post compensation for OAS.....</i>	<i>X</i>
<i>Table A3.2 Descriptive Statistics - Forest height estimated pre- and post-deorientation.....</i>	<i>XI</i>
<i>Table A3.3 Accuracy assessment for derived forest height after deorientation .....</i>	<i>XII</i>

## List of Symbols and Notations Used

Symbol / Notation	Meaning	First Appearance
$\vec{E}(\vec{r}, t)$	Wave electric field	4
$H(\vec{r}, t)$	Wave magnetic field	4
$\vec{D}(\vec{r}, t)$	Wave electric induction	4
$\vec{B}(\vec{r}, t)$	Wave magnetic induction	4
$\Lambda$	Cross product	4
$(\cdot)$	Dot product	4
$\vec{E}$	Electric field	5
$\vec{H}$	Magnetic field	5
$\beta$	Phase constant	5
$f$	Frequency	5
$\lambda$	Wavelength	5
$\omega$	Angular frequency	5
$k$	Wavenumber	5
$\theta$	Orientation angle	5
$\tau$	Ellipticity angle	5
[S]	Scattering matrix	7
$k_p$	Pauli basis scattering vector	7
$k_L$	Lexicographic scattering vector	7
$\langle \cdot \rangle$	Ensemble averaging	7
*	Complex conjugation	8
[C]	Covariance Matrix	8
[T]	Coherence Matrix	11
$\theta_0$	Radar Look angle	11
$\gamma$	Complex coherence	15
$\omega_1, \omega_2$	Polarization basis	15
H_avg	Average tree height in a plot	22
H_100	Highest tree height in a plot	22
H_under	Understory height	22
[U]	Unitary matrix	24
$\phi$	Interferometric phase	25
$k_z$	Interferometric wavenumber`	25
$\theta_1, \theta_2$	Incidence angles	26
p-value	Value of Significance	58
$N$	Number of samples	58
$\sigma_M$	Average Accuracy	59
$\varphi$	Vegetation bias	IV

## **Abbreviations**

CAI – *Coherence Amplitude Inversion*

DEM – *Digital Elevation Model*

FCC – *False Color Composite*

GPS – *Global Positioning System*

InSAR – *Interferometric SAR*

POA – *Polarization Orientation Angle*

PolInSAR – *Polarimetric Interferometry SAR*

PolSAR – *Polarimetric SAR*

RADAR – *Radio Detection And Ranging*

RMSE – *Root Mean Square Error*

RVoG – *Random Volume over Ground*

SLC – *Single Look Complex*

SNR – *Signal to Noise Ratio*

SAR – *Synthetic Aperture Radar*

SRTM – *Shuttle Radar Topographic Mission*

SU – *Special Unitary matrix*

TSI – *Three Stage Inversion*

## **1. INTRODUCTION**

---

Polarimetric Synthetic Aperture Radar Interferometry (PolInSAR) is a relatively new and advanced SAR technique. PolInSAR is sensitive to the vertical distribution of scatterers. It combines the advantages of Polarimetry and Interferometry. Polarimetric SAR (PolSAR) techniques are used to extract the different scattering patterns of targets. The extraction of scattering information about a target can help in determining various physical properties of the scatterer, such as shape, orientation and dielectric property. Interferometric SAR (InSAR) is sensitive to the scatterer's position in the vertical plane. Combining the PolSAR techniques with InSAR leads to better estimation of location of different types of scatterers along the vertical axis. PolInSAR techniques use this principle to estimate the height of structures such as forests.

### **1.1 Motivation**

Various forest height estimation algorithms have been proposed by Cloude and Papathanassiou (Cloude and Papathanassiou, 2003; Cloude and Papathanassiou, 1998; Papathanassiou and Cloude, 2001). These techniques have been applied on air-borne PolInSAR data in various studies in the past years. However very few studies (Krieger *et al.*, 2005; Li *et al.*, 2014; Zou *et al.*, 2013) have been carried out using space-borne PolInSAR data. Airborne data has several advantages over space-borne acquired data such as spatial resolution, signal-to-noise ratio (SNR) and temporal resolution (Lee, 2012). Space-borne PolInSAR data, on the other hand, provides global coverage. Difficulties in procurement of airborne data in India, necessitates the need for utilization of space-borne data. Fully polarimetric space-borne SAR systems such as ALOS-2, RADARSAT-3 will be launched in the near future. It is essential to study space-borne PolInSAR techniques and analyze the derived forest stand height.

The present work applies PolInSAR techniques to space-borne C-band RADARSAT-2 data. It has been recommended (Lee and Ainsworth, 2011; Lee *et al.*, 2002) to compensate the PolSAR data for shift induced in the Polarization Orientation Angle (POA) for accurate estimation of geophysical parameter extraction. The POA is the angle between the semi-major axis and the line of sight of the polarization ellipse. A shift in POA is induced when the SAR wave interacts with certain types of scattering media. The volume scattering power increases and double-bounce scattering power decreases after compensating for the POA shift. Previous work on POA shift has analyzed the effect on air-borne PolSAR data in P-, L- and C-bands. The effect of POA shift on space-borne PolSAR and PolInSAR data needs to be studied. In the present work, the effect of POA shift (deorientation) is studied on space-borne PolSAR data in all the available frequency bands. L-, C- and X-band PolSAR data is utilized to study the effect of POA shift. This study also analyses the effects of POA shift on PolInSAR data and the forest height estimated using PolInSAR techniques.

Forests and vegetated areas are a complex scattering media. It comprises of volume scattering due to randomly oriented leaf and branch interactions, double bounce scattering from trunk and ground and surface scattering from the ground surface. This complex medium can be modelled as a Random Volume over Ground (RVoG). ‘Coherence Amplitude Inversion technique’(CAI) for forest height estimation assumes the RVoG to model the vegetation layer whereas the ‘Three Stage Inversion’ (TSI) technique applies the algorithm considering the two-layer model of vegetation developed by (Treuhaft *et al.*, 1996). Non-forest regions, especially dry riverbed areas and urban structures may act as volume scatterers. In dry riverbeds, the stones in the dry river are randomly oriented and closely packed. This sometimes leads to dominant double-bounce and volume scattering. In high density urban areas, the multiple scattering from closely spaced structures leads to higher volume scattering. These features, in such cases present with all three scattering mechanisms, much the same way as the forests. This may lead to the height estimation algorithms modeling these features as forest layers, leading to overestimation in the height. This leads to errors in estimation of tree height using the different PolInSAR based algorithms. The backscatter and coherence patterns of the vegetated and non-vegetated areas are different. This work analyses the suitability of coherence and backscatter based approaches for improvements in the algorithms for PolInSAR based tree height estimation.

## **1.2 Innovation**

The present research work aims to analyze the available tree height estimation techniques and innovatively develop a coherence and backscatter based approach for improvements in algorithm for PolInSAR based tree height. The approach also aims to improve the existing algorithm’s suitability for application, and accurate estimation of tree height in forest as well as non-forest areas.

## **1.3 Objectives of the thesis**

The main objective of this thesis is to study the PolSAR and PolInSAR techniques for extraction of scattering information of different targets and the retrieval of the physical properties of the natural scattering media. For this purpose following sub-objectives are formulated:

- Investigation of PolSAR and PolInSAR techniques for scattering information retrieval of different targets.
- Estimation of coherences contributed by different land use land cover features in all possible polarization combinations.
- Effect of polarization orientation angle shift on PolSAR and PolInSAR data products.
- Estimation of forest height using PolInSAR based ‘Coherence Amplitude Inversion’ technique and ‘Three Stage Inversion’ technique.
- Validation and accuracy assessment of the estimated forest height.
- Suitability of backscatter and coherence based approaches for improvement in the algorithm for vertical tree height estimation.

## **1.4 Research Questions**

The research work aims to answer the following research questions through this thesis.

- How do complex coherence in different polarizations, vary for different scattering media?
- What will be the effect of POA shift on multi-frequency PolSAR data?
- Does POA shift compensation affect the PolInSAR data?
- What is the effect of deorientation on the modeled forest height?
- Which among CAI and TSI technique is more robust and better suited for estimation of forest stand height?
- What is the accuracy of the estimated forest height using both the CAI and TSI techniques when compared with field measured height?
- Is backscatter and coherence based approach suitable for improvements in the algorithm for vertical tree height estimation?

## **1.5 Synopsis**

The thesis comprises of the introduction and the following five chapters:

Chapter 2 starts with background in basics of electromagnetics, polarization ellipse and the scattering matrix. The chapter also provides a brief overview of the research carried out in the fields of PolSAR decomposition and Polarization orientation angle shift. PolSAR and InSAR are introduced and their combination in the form of PolInSAR, used in this study is reviewed in detail in this chapter.

Chapter 3 gives a brief description of the study area used for this study and the data sets utilized during the research work. It also describes the field survey carried out for validation of the results.

Chapter 4 provides the methods employed for achieving the goals of this study. It is divided into three parts. The first part describes the methods employed for study of orientation angle shift on PolSAR and PolInSAR data. The second part provides the existing methods used for estimation of forest height while the third part proposes an improved technique for forest height measurement which identifies the vegetated areas and applies the technique selectively.

Chapter 5 presents the results of the methods described in the preceding chapter. Results for the forest height estimation, its validation using the field survey data and accuracy assessment are also presented in this chapter.

Chapter 6 provides the conclusions derived from the present study and recommendations for future work based on the presented findings.

## **2. LITERATURE REVIEW AND BACKGROUND**

---

## State of the Art

An overview of the current state of investigations in the fields of PolSAR based orientation angle shift and PolInSAR based forest-stand height retrieval are presented in this chapter. For detailed history and evolution of radar and SAR systems and its applications in earth remote sensing techniques refer to (Ulaby *et al.*, 1986, 1982, 1981). SAR remote sensing is an important tool for geo-physical parameter extraction from natural and man-made features. Fully polarimetric SAR (PolSAR) systems are capable of transmitting and receiving SAR signals in both horizontal (H) and vertical (V) polarizations. The information of the target is captured by the Scattering matrix explained in Section 2.3. The concept of polarization orientation angle shift is introduced in Section 2.6 and the methods for determining the shift and compensating for the same are also presented in this section.

Polarimetric SAR Interferometric (PolInSAR) is a Radar remote sensing technique which combines the advantages of two SAR remote sensing technologies of Polarimetric SAR (PolSAR) and Interferometric SAR (InSAR) (Cloude, 2006, 2005). PolInSAR is introduced in Section 2.7 and methods for forest stand height determination are also presented.

## 2.1 Basics of Electromagnetics

RADAR (henceforth written as ‘radar’) stands for **RA**Dio **D**etection **A**nd **R**anging. A radar system transmits an electromagnetic signal and detects the received backscattered signal (Skolnik, 2008; Skolnik, 2003). The echo signal backscattered from the target provides information about the target. The time taken by the electromagnetic wave to travel from the transmitter back to it provides the distance of the target. Directive antennas are used to detect the location of the object and its angular direction. Radar systems were largely developed during the second World War for military purposes (Skolnik, 2008). The technology was opened for civilian applications in later years.

The electromagnetic waves are governed by the Maxwell equation set defined as (Lee and Pottier, 2009):

$$\begin{aligned}
 \vec{\nabla} \Lambda \vec{E}(\vec{r}, t) &= -\frac{\delta \overline{B}(\vec{r}, t)}{\delta t} \\
 \vec{\nabla} \Lambda \vec{H}(\vec{r}, t) &= \vec{J}_T(\vec{r}, t) + \frac{\delta \overline{D}(\vec{r}, t)}{\delta t} \\
 \vec{\nabla} \cdot \vec{D}(\vec{r}, t) &= \rho(\vec{r}, t) \\
 \vec{\nabla} \cdot \vec{B}(\vec{r}, t) &= 0
 \end{aligned}
 \tag{2.1}$$

Where,  $\vec{E}(\vec{r}, t)$  – wave electric field,  $H(\vec{r}, t)$  – wave magnetic field,  $\vec{D}(\vec{r}, t)$  – wave electric induction and  $\vec{B}(\vec{r}, t)$  – wave magnetic induction,  $\Lambda$  – signifies cross multiplication of vectors and dot (.) signifies the dot multiplication. Electromagnetic field is composed of electric field ( $\vec{E}$ )

and magnetic field ( $\vec{H}$ ) perpendicular to each other. The electric and magnetic fields can be expressed by the following expressions (Richards, 2009):

$$\begin{aligned}\vec{E} &= E_0 \cos(\omega t - \beta R + \phi_e) \\ \vec{H} &= H_0 \cos(\omega t - \beta R + \phi_h)\end{aligned}\quad (2.2)$$

$\beta$  is phase constant (measured in radians per meter) also written as the wave number k. In free space,

$$\beta = \frac{\omega}{c} = \frac{2\pi f}{\lambda f} = \frac{2\pi}{\lambda}\quad (2.3)$$

Where f- frequency of operation and  $\lambda$ - is the wavelength of the electromagnetic signal. As the electric field and magnetic fields are perpendicular to each other, only the description of electric field can suffice to provide complete characteristics of electromagnetic waves. Consider an electromagnetic wave travelling along the positive z direction. The electric field can be expressed in vectorial form (Lee and Pottier, 2009):

$$\vec{E}(z, t) = \begin{bmatrix} E_{0x} e^{-az} \cos(\omega t - kz + \delta_x) \\ E_{0y} e^{-az} \cos(\omega t - kz + \delta_y) \\ 0 \end{bmatrix}\quad (2.4)$$

It can be observed that the electric field can be decomposed into fields in  $\bar{x}$  and  $\bar{y}$  directions. The spatial evolution of the resultant electric field follows a helical trajectory. As it is difficult to visualize a helical trajectory, the concept of polarization ellipse is introduced.

## 2.2 Polarization Ellipse

The path of the electric field is traced over a time period  $t_0$ .  $t_0$  is the time taken for the wave to go through one complete cycle. This gives a loci of the path of the field location along the z-axis. This path is called the polarization ellipse. The ellipse is defined by the semi-major axis, its orientation angle and ellipticity. Figure 2.1 provides a graphical representation of the Polarization ellipse. The amplitude of the ellipse, 'A' can determined from the ellipse axis as:

$$A = \sqrt{E_{0x}^2 + E_{0y}^2}\quad (2.5)$$

The orientation angle of polarization ellipse is defined as the angle the semi-major axis tends with the horizontal axis. It is represented by the symbol  $\theta$ .

$$\tan 2\theta = 2 \frac{E_{0x} E_{0y}}{E_{0x}^2 - E_{0y}^2} \cos \delta \quad \text{with } \delta = \delta_y - \delta_x\quad (2.6)$$

Ellipticity is defined as

$$|\sin 2\tau| = 2 \frac{E_{0x} E_{0y}}{E_{0x}^2 + E_{0y}^2} |\sin \delta|\quad (2.7)$$

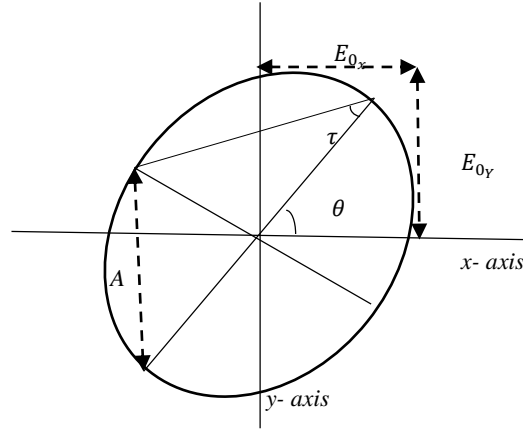


Figure 2.1 Graphical representation of the Polarization Ellipse. ‘A’ is the amplitude of the ellipse given by Eq. (2.5),  $\theta$  is the orientation angle defined by Eq. (2.6) and  $\tau$  is the ellipticity also called as ellipse aperture given in Eq. (2.7)

In Eq. (2.6)  $\delta$  represents the phase difference between the horizontal and vertical components of the electric field. The radar system can transmit electromagnetic waves in a particular polarization- horizontally or vertically. Thus we obtain the H (horizontally) and V (vertically) polarized signals. However, the radar system can receive only those signals which are in the same polarization as the receiving antenna.

### 2.3 Scattering Matrix

The scattering matrix [S] provides the relationship between the incident and scattered electromagnetic wave from a target/resolution cell (Jin and Xu, 2013).

$$[S] = \begin{bmatrix} S_{HH} & S_{HV} \\ S_{VH} & S_{VV} \end{bmatrix} \quad (2.9)$$

Consider that the antenna is transmitting in two polarizations H and V. Then their direction vectors are given by  $\hat{e}_H$  and  $\hat{e}_V$ . If a wave of polarization  $\hat{e}_h$  is transmitted, then the returned wave under basis  $(\hat{e}_H, \hat{e}_V)$  is written as (Jin and Xu, 2013):

$$E_s = S_{HH}\hat{e}_H + S_{VH}\hat{e}_V \quad (2.10)$$

Similarly it can be stated that

$$E_s = S_{VV}\hat{e}_V + S_{HV}\hat{e}_H \quad (2.11)$$

Hence, Eq. (2.8) and Eq. (2.9) can be reformed to define

$$E_s = \begin{bmatrix} S_{HH} & S_{HV} \\ S_{VH} & S_{VV} \end{bmatrix} E_i \quad (2.12)$$

In this study, backscattering reciprocity is assumed, *i.e.*  $S_{HV} = S_{VH}$ . The scattering matrix [S] can be vectorized using two basis, the Pauli basis and the Lexicographic straightforward vectorization (Cloude and Pottier, 1996; Jin and Xu, 2013)

$$k_P = \frac{1}{\sqrt{2}} [S_{HH} + S_{VV} \quad S_{HH} - S_{VV} \quad 2S_{HV}]^T$$

$$k_L = [S_{HH} \quad \sqrt{2}S_{HV} \quad S_{VV}]^T \quad (2.13)$$

Where the subscript P and L denote Pauli and Lexicographic basis respectively. The covariance matrices of the two basis are defined as

$$[T] = \langle k_P, k_P^\dagger \rangle, \quad [C] = \langle k_L, k_L^\dagger \rangle \quad (2.14)$$

The symbol  $\dagger$  stands for conjugate transpose operator. [T] is the coherence matrix and [C] is the covariance matrix. The nomenclature is different only to differentiate the vectorization basis (Jin and Xu, 2013). The Pauli vector  $k_P$  can be represented in terms of  $\alpha$  and  $\beta$  angles (Cloude and Pottier, 1996; Feng Xu and Ya-Qiu Jin, 2005).  $\alpha$  and  $\beta$  represent the relative scale of each complex element of  $k_P$  in the Pauli space while angles  $\phi_1, \phi_2, \phi_3$  are the phase of each element.  $k_P$  can be represented in terms of  $\alpha, \beta, \phi_1, \phi_2, \phi_3$  as (Cloude and Pottier, 1996; Feng Xu and Ya-Qiu Jin, 2005)

$$k_P = ||k_P|| \cdot \begin{bmatrix} \cos \alpha e^{j\phi_1} \\ \sin \alpha \cos \beta e^{j\phi_2} \\ \sin \alpha \sin \beta e^{j\phi_3} \end{bmatrix} \quad (2.15)$$

A similar parameterization of  $k_L$  was presented by Xu and Jin (Feng Xu and Ya-Qiu Jin, 2005; Jin and Xu, 2013)

$$k_L = ||k_L|| \cdot \begin{bmatrix} \sin c \cos a e^{j\phi_0} \\ \cos c e^{j\phi_x} \\ \sin c \sin a e^{j(\phi_0+2b)} \end{bmatrix} \quad (2.16)$$

Using the definition of  $k_L$  and the above equation, the terms a, b, c can be defined as

$$\begin{aligned} a &= \tan^{-1} \left( \frac{|S_{VV}|}{|S_{HH}|} \right) \\ b &= \frac{1}{2} \arg \left( \frac{S_{VV}}{S_{HH}} \right) \\ c &= \cos^{-1} (\sqrt{2} |S_{HV}| / ||k_L||) \end{aligned} \quad (2.17)$$

Where the term  $\arg(\cdot)$  means the phase angle of a complex number. It can be observed that ‘a’ is the ratio of the amplitudes of co-polarized scattering components; ‘b’ is the phase difference between co-polarized terms and ‘c’ indicates cross-polarized scattering. The terms a, b and c can be expressed in terms of  $\alpha$  and  $\beta$  as

$$\begin{aligned} \cos \alpha &= \sqrt{\frac{1 + \sin 2a \cos 2b}{2 + 2/\tan^2 c}} \\ \cos \beta &= \sqrt{\frac{1 - \sin 2a \cos 2b}{1 - \sin 2a \cos 2b + 2/\tan^2 c}} \end{aligned} \quad (2.18)$$

The coherence matrix [T] and the covariance matrix [C] in H,V-polarization are represented as (Yamaguchi *et al.*, 2006, 2005) given in Eq. 2.19 and Eq. 2.20. Here  $\langle \cdot \rangle$  represents ensemble averaging during data processing and the superscript \* stands for complex conjugation. The superscript <sup>H,V</sup> denote the polarization basis for the matrices. It will be shown in later sections that the different polarization basis can be transformed into one another to obtain different scattering and coherence/ covariance matrices.

$$\langle [C] \rangle^{H,V} = \begin{bmatrix} \langle |S_{HH}|^2 \rangle & \sqrt{2}\langle (S_{HH}S_{HV}^*) \rangle & \langle (S_{HH}S_{VV}^*) \rangle \\ \sqrt{2}\langle (S_{HV}S_{HH}^*) \rangle & \langle 2|S_{HV}|^2 \rangle & \sqrt{2}\langle (S_{HV}S_{VV}^*) \rangle \\ \langle (S_{VV}S_{HH}^*) \rangle & \sqrt{2}\langle (S_{VV}S_{HV}^*) \rangle & \langle |S_{VV}|^2 \rangle \end{bmatrix} \quad (2.19)$$

$$\langle [T] \rangle^{H,V} = \begin{bmatrix} \frac{1}{2}\langle |S_{HH} + S_{VV}|^2 \rangle & \frac{1}{2}\langle (S_{HH} + S_{VV})(S_{HH} - S_{VV})^* \rangle & \langle (S_{HH} + S_{VV})S_{HV}^* \rangle \\ \frac{1}{2}\langle (S_{HH} - S_{VV})(S_{HH} + S_{VV})^* \rangle & \frac{1}{2}\langle |S_{HH} - S_{VV}|^2 \rangle & \langle (S_{HH} - S_{VV})S_{HV}^* \rangle \\ \langle S_{HV}(S_{HH} + S_{VV})^* \rangle & \langle S_{HV}(S_{HH} - S_{VV})^* \rangle & \langle 2|S_{HV}|^2 \rangle \end{bmatrix} \quad (2.20)$$

## 2.4 PolSAR Decomposition Techniques

A PolSAR system captures the scattering behavior of targets in all possible polarizations. As the target behaves differently with signals in different polarizations, the PolSAR data acquires significance (Woodhouse, 2006). This dependence of PolSAR data with target properties is the basis of target decomposition techniques. Target decomposition techniques were first formalized by Huynen (Huynen, 1970) in his doctoral dissertation. A review of the decomposition techniques is presented in (Cloude and Pottier, 1996).

Target decomposition techniques provide a dominant scattering mechanism for a pixel or a group of pixels (Cloude and Pottier, 1996). Freeman and Durden (Freeman and Durden, 1998) developed a model-based incoherent decomposition technique which decomposes the target into three scattering mechanisms- volume scattering, double-bounce scattering and surface scattering. This scattering mechanism considers the case of reflection symmetry which corresponds to  $\langle S_{HH}S_{HV}^* = 0 \rangle$  and  $\langle S_{VV}S_{HV}^* = 0 \rangle$  in the covariance matrix. However, this condition does not hold true in case of urban areas and in case of more complicated geometric features (Yamaguchi *et al.*, 2005). Yamaguchi *et al.* (Yamaguchi *et al.*, 2005) introduced the fourth scattering mechanism of helix scattering which often appears in urban areas and is less prominent in natural features. This Yamaguchi four component decomposition technique was later extended for coherence matrix (Yamaguchi *et al.*, 2006). Yamaguchi decomposition technique decomposes the coherence matrix into (Yamaguchi *et al.*, 2006)

$$[T] = \frac{f_s}{1 + |\beta|^2} \begin{bmatrix} 1 & \beta^* & 0 \\ \beta & |\beta|^2 & 0 \\ 0 & 0 & 0 \end{bmatrix} + \frac{f_d}{1 + |\alpha|^2} \begin{bmatrix} |\alpha|^2 & \alpha & 0 \\ \alpha^* & 1 & 0 \\ 0 & 0 & 0 \end{bmatrix} + \frac{f_v}{4} \begin{bmatrix} 2 & 0 & 0 \\ 0 & 1 & 0 \\ 0 & 0 & 1 \end{bmatrix} + \frac{f_c}{2} \begin{bmatrix} 0 & 0 & 0 \\ 0 & 1 & \pm j \\ 0 & \mp j & 1 \end{bmatrix} \quad (2.21)$$

Where  $\alpha, \beta$  are complex observables defined by (Yamaguchi *et al.*, 2006) and  $f_s, f_v, f_d$  and  $f_c$  are the powers of surface, volume, double-bounce and helix scattering respectively. They are given in terms of elements of scattering matrix as under:

$$\begin{aligned} f_c &= 2|Im\langle S_{HV}^*(S_{HH} - S_{VV}) \rangle| \\ f_v &= 8\langle |S_{HV}|^2 \rangle - 4|Im\langle S_{HV}^*(S_{HH} - S_{VV}) \rangle| \\ f_s &= B, f_d = A, \alpha = \frac{C}{A}, \beta^* = \frac{C}{B} \end{aligned} \quad (2.22)$$

Where A, B and C are given by:

$$\begin{aligned}
 A &= \frac{1}{2} \langle |S_{HH} - S_{VV}|^2 \rangle - 2 \langle |S_{HV}|^2 \rangle \\
 B &= \frac{1}{2} \langle |S_{HH} + S_{VV}|^2 \rangle - 4 \langle |S_{HV}|^2 \rangle + 2 |Im \langle S_{HV}^* (S_{HH} - S_{VV}) \rangle| \\
 C &= \frac{1}{2} \langle (S_{HH} + S_{VV})(S_{HH} - S_{VV})^* \rangle
 \end{aligned} \tag{2.23}$$

The effect of shift in POA (Lee and Ainsworth, 2011) on decomposition technique was later incorporated in (Yamaguchi *et al.*, 2011). The POA shift is discussed in Section 2.6. For the present study, the Yamaguchi decomposition technique is used to study the effects of POA shift on multi-frequency SAR data. (J. David Ballester-Berman and Lopez-Sanchez, 2010; J.D. Ballester-Berman and Lopez-Sanchez, 2010) have applied the concept of Freeman-Durden (Freeman and Durden, 1998) Target decompositions to PolInSAR data. This technique retrieves not only the magnitude but also the interferometric phase of the scattering mechanisms. However further insights into the technique are beyond the scope of present work.

## 2.5 Polarization Basis Transformations

Change of Polarization basis formalism is required in order to provide proper comparisons of measurements taken with SAR systems using different basis (Kostinski and Boerner, 1986). The different possible polarization basis can be viewed on the Poincare Sphere (Figure 2.2). In Figure 2.2, the notation ‘CR’ stands for Right Circular polarization, ‘CL’ stands for Left Circular polarization. The ‘CR’ and ‘CL’ polarizations along with left and right handed elliptical polarizations are also visualized.

Once a scattering matrix is obtained in a polarization basis, the matrix can be obtained in any other basis using simple mathematical transformations (Lee and Pottier, 2009). For transformation from one polarization basis to other, a special unitary matrix, SU(2) group is used (Lee and Pottier, 2009). For any elliptical basis change, the special unitary matrix is defined with

$$\begin{aligned}
 U_2(\theta, \tau, \alpha) &= U_2(\theta)U_2(\tau)U_2(\alpha) \\
 &= \begin{bmatrix} \cos \theta & -\sin \theta \\ \sin \theta & \cos \theta \end{bmatrix} \begin{bmatrix} \cos \tau & j \sin \tau \\ j \sin \tau & \cos \tau \end{bmatrix} \begin{bmatrix} e^{+j\alpha} & 0 \\ 0 & e^{-j\alpha} \end{bmatrix} \\
 &= \frac{1}{\sqrt{1 + |\rho|^2}} \begin{bmatrix} 1 & -\rho^* \\ \rho & 1 \end{bmatrix} \begin{bmatrix} e^{+j\xi} & 0 \\ 0 & e^{-j\xi} \end{bmatrix}.
 \end{aligned} \tag{2.24}$$

Where,  $\theta$ ,  $\tau$  and  $\alpha$  are the geometric parameters of the polarization ellipse described by the Jones vector of the new polarization basis (Lee and Pottier, 2009).  $\theta, \tau$  are the orientation angle, ellipticity angle of the Polarization ellipse as defined in Eq. (2.6) and Eq. (2.7) respectively, and the term  $\alpha$  is the absolute phase of the Jones vector (Jin and Xu, 2013; Lee and Pottier, 2009; Richards, 2009) resulting from any propagation path (Richards, 2009).

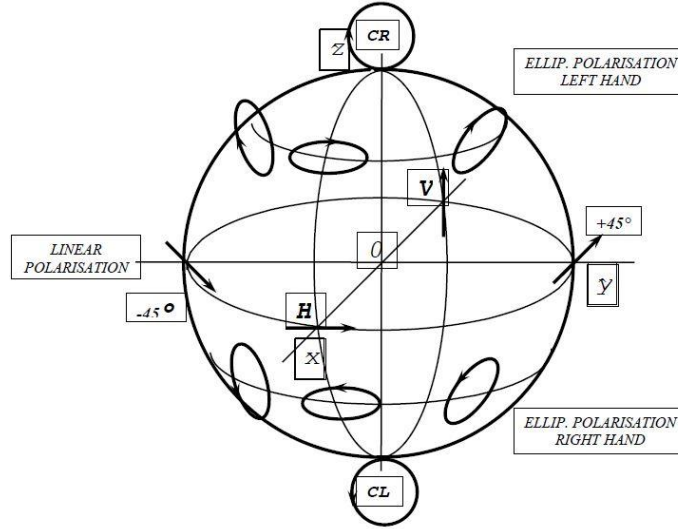


Figure 2.2 Poincare Sphere depicting all the possible polarization basis. CL and CR are the left and right circular polarization basis respectively. The elliptical and linear polarizations can also be observed

The Jones vector describes the wave polarization of the electric field using minimum information (Lee and Pottier, 2009). It can be written as:

$$\vec{E} = Ae^{j\alpha} \begin{bmatrix} \cos \theta & -\sin \theta \\ \sin \theta & \cos \theta \end{bmatrix} \begin{bmatrix} \cos \tau \\ j \sin \tau \end{bmatrix} \quad (2.25)$$

Where, ‘A’ is the amplitude of the electric field vector  $\vec{E}$ .

Now, in Eq. (2.24), the special unitary matrix is defined in terms of  $\rho$  and  $\xi$ , which are related to the terms of  $\theta, \tau$  and  $\alpha$  by the equation (2.20)(Lee and Pottier, 2009).

$$\rho = \frac{\tan \theta + j \tan \tau}{1 - j \tan \theta \tan \tau} \quad \xi = \alpha - \tan^{-1}(\tan \theta \tan \tau) \quad (2.26)$$

The following table presents the polarization ellipse parameters for some commonly used canonical polarization states (Jin and Xu, 2013; Lee and Pottier, 2009; Richards, 2009)

Table 2.1 Polarization Ellipse parameters for some common canonical polarization states.

Polarization State	Unit Jones Vector $\hat{u}_{x,y}$	Orientation Angle $\theta$	Ellipticity Angle $\tau$
Horizontal (H)	$\hat{u}_H = \begin{bmatrix} 1 \\ 0 \end{bmatrix}$	0	0
Vertical (V)	$\hat{u}_V = \begin{bmatrix} 0 \\ 1 \end{bmatrix}$	$\frac{\pi}{2}$	0
Linear (+45°)	$\hat{u}_{+45^\circ} = \frac{1}{\sqrt{2}} \begin{bmatrix} 1 \\ 1 \end{bmatrix}$	$\frac{\pi}{4}$	0
Linear (-45°)	$\hat{u}_{-45^\circ} = \frac{1}{\sqrt{2}} \begin{bmatrix} 1 \\ -1 \end{bmatrix}$	$-\frac{\pi}{4}$	0
Left Circular	$\hat{u}_L = \frac{1}{\sqrt{2}} \begin{bmatrix} 1 \\ j \end{bmatrix}$	$[-\frac{\pi}{2} \dots \frac{\pi}{2}]$	$\frac{\pi}{4}$
Right Circular	$\hat{u}_R = \frac{1}{\sqrt{2}} \begin{bmatrix} 1 \\ -j \end{bmatrix}$	$[-\frac{\pi}{2} \dots \frac{\pi}{2}]$	$-\frac{\pi}{4}$

Using the elements from Table 2.1 in Eq. 2.24 special unitary matrix can be constructed for polarization basis transformation. These unitary matrices are used for changing the polarization basis on the scattering matrix. For example, for changing the basis to left-left orthogonal circular basis, the unitary basis change matrix is given as (Lee and Pottier, 2009)

$$\begin{aligned} \theta = 0, \tau = +\frac{\pi}{4}, \alpha = 0 &\Rightarrow U_{2\hat{n}_\perp} = \frac{1}{\sqrt{2}} \begin{bmatrix} 1 & j \\ j & 1 \end{bmatrix} \\ \therefore U_{2(\hat{x},\hat{y}) \rightarrow (\hat{n}_\perp)} = U_{2\hat{n}_\perp}^{-1} &= \frac{1}{\sqrt{2}} \begin{bmatrix} 1 & -j \\ -j & 1 \end{bmatrix} \end{aligned} \quad (2.27)$$

A similar extension of the Special unitary matrix can be constructed for 3x3 matrix case. The 3x3 Special unitary matrix is given by (Cloude and Papathanassiou, 1998; Cloude and Pottier, 1996; Jin and Xu, 2013; Lee and Pottier, 2009)

$$U_3 = \frac{1}{2(1 + \rho\rho^*)} \begin{bmatrix} 2 + \rho^2 + \rho^{*2} & \rho^{*2} - \rho^2 & 2(\rho - \rho^*) \\ \rho^2 - \rho^{*2} & 2 - (\rho^2 + \rho^{*2}) & 2(\rho + \rho^*) \\ 2(\rho - \rho^*) & -2(\rho + \rho^*) & 2(1 - \rho\rho^*) \end{bmatrix} \quad (2.28)$$

The  $[U_3]$  matrix is used for transformation of one polarization basis coherence matrix into other basis. In section 1.2.2, in the steps to retrieve physical information from the PolInSAR data, this basis transformation is utilized. As an extension of the example in Eq. 2.28, the  $[U_3]$  matrix for left-left orthogonal basis becomes

$$\begin{aligned} U_{3\hat{n}_\perp} \left( \theta = 0, \tau = +\frac{\pi}{4}, \alpha = 0 \right) \\ = \frac{1}{2(1 + ii^*)} \begin{bmatrix} 2 + i^2 + i^{*2} & i^{*2} - i^2 & 2(i - i^*) \\ i^2 - i^{*2} & 2 - (i^2 + i^{*2}) & 2(i + i^*) \\ 2(i - i^*) & -2(i + i^*) & 2(1 - ii^*) \end{bmatrix} \end{aligned} \quad (2.29)$$

## 2.6 Polarization Orientation Angle Shift

POA is the angle subtended by the semi-major axis of the polarization ellipse with the X-axis (Woodhouse, 2006). On interaction with certain types of target features, a shift is induced in the POA of the incident SAR wave. The POA shift is induced by terrain slopes in azimuth and range directions (Lee *et al.*, 2002, 2000; Schuler *et al.*, 1996). It has been demonstrated (Lee and Ainsworth, 2011; Lee and Pottier, 2009) that the POA shift is induced in SAR signal after interaction with rugged terrain, surfaces with non-zero azimuth and range slopes and urban areas with structures non-aligned in the along-track direction of the satellite pass. The induced shift in POA due to azimuth and range slopes is given by (Lee and Ainsworth, 2011)

$$\tan \theta = \frac{\tan \omega}{- \tan \gamma \cos \theta_0 + \sin \theta_0} \quad (2.30)$$

Where  $\theta$  - orientation angle,  $\theta_0$  - radar look angle,  $\tan \omega$  - ground slope in the azimuth direction and  $\tan \gamma$  - slope in ground range direction. The POA shift is defined as the angular shifting of the horizontal and vertical planes of a SAR antenna configuration to maximize the  $S_{HH}$  return signal (Lee *et al.*, 2002). The induced shift in orientation angle has a direct impact on the elements of scattering matrix, with the cross-component (HV) scattering power increasing (Lee and Ainsworth, 2011) and the covariance or coherence matrix being reflection asymmetrical (Lee and Ainsworth, 2011; Lee *et al.*, 2000). This leads to inaccurate information extraction from the

coherence or covariance matrix. It is observed that the double-bounce scattering power reduces and volume scattering power increases due to shift in POA shift (Lee and Ainsworth, 2011).

Various techniques for estimation of orientation angle shift have been listed by Lee and Ainsworth (Lee and Ainsworth, 2011). The circular polarization technique developed by Lee *et al.* (Lee *et al.*, 2002, 2000) is used in the present work. A brief review of the algorithm as provided in (Lee and Ainsworth, 2011), is presented here.

The circular polarization method uses the circular basis of  $LL$  and  $L_{\perp}L_{\perp}$  in the monostatic backscattering alignment convention. The relation between the scattering matrix components in linear basis and circular basis are given as

$$\begin{aligned} S_{L_{\perp}L_{\perp}} &= \frac{S_{VV} - S_{HH} + i2S_{HV}}{2} \\ S_{L_{\perp}L_{\perp}} &= \frac{S_{VV} - S_{HH} + i2S_{HV}}{2} \end{aligned} \quad (2.31)$$

Eq. (2.27) provides the relationship between the rotated  $S_{LL}$  and  $S_{L_{\perp}L_{\perp}}$  and non-rotated scatterer,  $\bar{S}_{LL}$  and  $\bar{S}_{L_{\perp}L_{\perp}}$  of a scattering medium rotated by an angle  $\theta$  about the line of sight.

$$\langle S_{LL} S_{L_{\perp}L_{\perp}}^* \rangle \approx \langle \bar{S}_{LL} \bar{S}_{L_{\perp}L_{\perp}}^* \rangle e^{-i4\theta} \quad (2.32)$$

From (2.2), the orientation angle can be easily computed and presented as

$$\tan(-4\theta) = \frac{-4\text{Re}(\langle (S_{HH} - S_{VV}) S_{HV}^* \rangle)}{-\langle |S_{HH} - S_{VV}|^2 \rangle + 4\langle |S_{HV}|^2 \rangle} \quad (2.33)$$

The orientation angle is phase unwrapped by adding  $\pi$  as explained in (Lee and Ainsworth, 2011; Lee *et al.*, 2002). The phase unwrapped orientation angle corresponds to the orientation angle induced due to terrain slope in azimuth and range direction as well as that induced by buildings not aligned along the azimuth direction. The orientation angle is given by (2.34)

$$\eta = \frac{1}{4} \left[ \tan^{-1} \left( \frac{-4\text{Re}(\langle (S_{HH} - S_{VV}) S_{HV}^* \rangle)}{-\langle |S_{HH} - S_{VV}|^2 \rangle + 4\langle |S_{HV}|^2 \rangle} \right) + \pi \right] \quad (2.34)$$

where,

$$\theta = \begin{cases} \eta, & \text{if } \eta \leq \pi/4 \\ \eta - \frac{\pi}{2}, & \text{if } \eta > \pi/4 \end{cases}$$

The derived coherence matrix [T] is rotated by angle  $\theta$  using unitary rotation operator [U] as given by

$$[\bar{T}] = [U][T][U^T], \text{ with } [U] = \begin{bmatrix} 1 & 0 & 0 \\ 0 & \cos 2\theta & \sin 2\theta \\ 0 & -\sin 2\theta & \cos 2\theta \end{bmatrix} \quad (2.35)$$

where [T] and  $[\bar{T}]$  are coherence matrices before and after rotation by angle  $\theta$ , respectively and the unitary matrix is represented by [U]. A simpler equation for estimation of orientation angle is presented in (Lee and Ainsworth, 2011) as:

$$\theta = \frac{1}{4} \left[ \tan^{-1} \left( \frac{-4\text{Re}(\langle (S_{HH} - S_{VV}) S_{HV}^* \rangle)}{-\langle |S_{HH} - S_{VV}|^2 \rangle + 4\langle |S_{HV}|^2 \rangle} \right) + \pi \right] \quad (2.36)$$

The addition of  $\pi$  term ensures that the coherence matrix is rotated towards the correct axis (Lee and Ainsworth, 2011). Using Eq. 2.36, the shift in orientation angle is calculated and the coherence matrix is compensated by rotating it by an equivalent angle as shown in Eq. 2.35. This technique is used to find the effect of shift in POA on multi-frequency, PolSAR data (Khati *et al.*,

2013). A study on the effect of POA shift on Yamaguchi decomposition products of multifrequency data, was presented by Khati *et al.* (Khati *et al.*, 2013). A similar approach is used in the present study.

## **2.7 Polarimetric SAR Interferometry (PolInSAR)**

Polarimetric SAR Interferometry (PolInSAR) is an advanced technique (Cloude and Papathanassiou, 1998) of Radar remote sensing that combines the advantages of Polarimetry and Interferometry. Using SAR Polarimetry target characteristics such as its orientation, material constituents (Boerner, 2006, 2004), shape and dielectric properties (Krieger *et al.*, 2005), permittivity as well as ensemble average entropy (Lee *et al.*, 2002; Neumann *et al.*, 2010) can be estimated. SAR Interferometry provides information on the coherence of the scattering mechanisms (Hellmann and Cloude, 2007) and the object's spatial (range/in-depth) structure (Boerner, 2004) and estimates the location of the scatterer in vertical plane through the phase difference in the images acquired from spatially separated apertures at either ends of a baseline (Krieger *et al.*, 2005). Combination of polarimetry and interferometry leads to separation of scattering mechanisms within a resolution cell. For complex scattering media such as forests, various types of scatterers are present below the canopy. The underlying scattering mechanisms can be interpreted using PolInSAR (Hellmann and Cloude, 2007) as the scattering media physical properties are closely related to the polarimetric features observed. The polarimetric and interferometric information are complementary to each other which leads to the combination of both approaches in Polarimetric SAR Interferometry (PolInSAR). Cloude and Papathanassiou formulated the PolInSAR theory (Cloude and Papathanassiou, 1998) and demonstrated its applications using single-baseline PolInSAR data (Papathanassiou and Cloude, 2001) and its extension to multi-baseline data is presented in (Neumann *et al.*, 2010).

PolInSAR data is studied in a number of application areas such as forest-stand /tree height retrieval (Li *et al.*, 2013; Luo *et al.*, 2010; Minh and Zou, 2013; Minh *et al.*, 2012; Nghia *et al.*, 2012; Tan and Yang, 2008), agricultural height estimation (Lopez-Sanchez and Ballester-Berman, 2009; Lopez-Sanchez *et al.*, 2012), crop parameter estimation (Ballester-Berman *et al.*, 2005), building parameter (Cai *et al.*, 2011; Zou *et al.*, 2013) and building height estimation (Colin-Koeniguer and Trouve, 2014), forest biomass estimation (Mette, 2006), forest parameter estimation (Frey *et al.*, 2012; Lee, 2012) and ground topography estimation (Lopez-Martinez and Papathanassiou, 2013; Zou *et al.*, 2011), among others. Forest parameters such as height, extinction and ground topography (Lopez-Martinez *et al.*, 2009) can also be estimated using PolSAR and PolInSAR data. However, the present work exclusively focuses on forest-stand retrieval using PolInSAR techniques.

Two PolSAR acquisitions are carried out using the exact same geometric configuration viz. Beam mode, Incidence angle, and Polarization mode. The scattering matrix for each pixel can be derived for both the acquisitions.  $[S_1]$  and  $[S_2]$  are the scattering matrices for the two acquisitions and the vectorized form can be represented by the scattering vectors  $\underline{k}_1$  and  $\underline{k}_2$  respectively (Schuler *et al.*, 1996). The 6x6 coherence matrix  $[T_6]$  is the main observable in PolInSAR. The Hermitian

positive semidefinite matrix  $[T_6]$  is generated from the outer product formed from the scattering vector  $\underline{k}_1$  and  $\underline{k}_2$  in Pauli Basis (Cloude and Papathanassiou, 1998)

$$[T_6] := \left\langle \begin{bmatrix} \underline{k}_1 \\ \underline{k}_2 \end{bmatrix} \begin{bmatrix} \underline{k}_1^{*T} & \underline{k}_2^{*T} \end{bmatrix} \right\rangle = \begin{bmatrix} [T_{11}] & [\Omega_{12}] \\ [\Omega_{12}]^{*T} & [T_{22}] \end{bmatrix} \quad (2.37)$$

$\underline{k}_1 = [S_{HH}^1 + S_{VV}^1 \quad S_{HH}^1 - S_{VV}^1 \quad 2S_{HV}^1]^T$  and  $\underline{k}_2 = [S_{HH}^2 + S_{VV}^2 \quad S_{HH}^2 - S_{VV}^2 \quad 2S_{HV}^2]^T$   
 Where the superscripts <sup>1</sup> and <sup>2</sup> represent the acquisitions from two ends of the baseline.

$$[T_6] = \left\langle \begin{bmatrix} S_{HH}^1 + S_{VV}^1 \\ S_{HH}^1 - S_{VV}^1 \\ 2S_{HV}^1 \\ S_{HH}^2 + S_{VV}^2 \\ S_{HH}^2 - S_{VV}^2 \\ 2S_{HV}^2 \end{bmatrix} [S_{HH}^{1*} + S_{VV}^{1*} \quad S_{HH}^{1*} - S_{VV}^{1*} \quad 2S_{HV}^{1*} \quad S_{HH}^{2*} + S_{VV}^{2*} \quad S_{HH}^{2*} - S_{VV}^{2*} \quad 2S_{HV}^{2*}] \right\rangle$$

$$[T_6] = \begin{bmatrix} [T_{11}] & [\Omega_{12}] \\ [\Omega_{12}]^{*T} & [T_{22}] \end{bmatrix} \quad (2.38)$$

In Eq. 2.38 - Eq. 2.39,  $[T_{11}]$  and  $[T_{22}]$  are the Hermitian coherence matrices for the two acquisitions and describe the polarimetric properties of each acquisition while  $[\Omega_{12}]$  is a non-hermitian complex matrix which contains both polarimetric and interferometric information.

SAR measurements are not directly related to the physical parameters of the targets, hence extraction of bio- and geo-physical parameters require the inversion of scattering models (Krieger *et al.*, 2005). These scattering models relate the physical parameters of the scattering processes to the observables from the SAR data. Complex structures such as forests act as a group of multiple scatterers – the tree trunk and ground acts as a dihedral surface leading to double-bounce scattering; ground near the tree acts as specular surface leading to surface scattering; leaves, twigs and branches lead to volume scattering in the higher canopy (S. Cloude and K. P. Papathanassiou, 2003; Tebaldini, 2010) (Figure 2.3). The scattering phase center is the location at which a particular scattering mechanism is dominant in the media. Using PolInSAR techniques, it becomes possible to identify the locations of the different scattering mechanism occurring in the target. This becomes possible as the SAR Polarimetry identifies the scattering mechanism and SAR Interferometry can locate it in vertical space (in-depth). In Figure 2.3, a pictorial representation is provided for the different scattering mechanisms occurring at different locations of a forest-stand.

This vegetation/forest structure can be modelled using the Random Volume over Ground (RVoG) scattering model (S. Cloude and K. P. Papathanassiou, 2003; Cloude, 2008, 2006; Mette, 2006; Papathanassiou and Cloude, 2001) which considers a vegetation layer of thickness  $h_v$  containing randomly oriented dipoles, located over a surface scattering media presented by a ground layer, positioned at height  $Z=Z_0$  as depicted in Figure 2.3.

$$\begin{aligned}
 [T_{11}] &= \begin{bmatrix} \langle |S_{HH}^1 + S_{VV}^1|^2 \rangle & \langle (S_{HH}^1 + S_{VV}^1)(S_{HH}^1 - S_{VV}^1)^* \rangle & 2\langle (S_{HH}^1 + S_{VV}^1)S_{HV}^{1*} \rangle \\ \langle (S_{HH}^1 - S_{VV}^1)(S_{HH}^1 + S_{VV}^1)^* \rangle & \langle |S_{HH}^1 - S_{VV}^1|^2 \rangle & 2\langle (S_{HH}^1 - S_{VV}^1)S_{HV}^{1*} \rangle \\ 2\langle S_{HV}^1 (S_{HH}^1 + S_{VV}^1)^* \rangle & 2\langle S_{HV}^1 (S_{HH}^1 - S_{VV}^1)^* \rangle & \langle 4|S_{HV}^1|^2 \rangle \end{bmatrix} \\
 [T_{22}] &= \begin{bmatrix} \langle |S_{HH}^2 + S_{VV}^2|^2 \rangle & \langle (S_{HH}^2 + S_{VV}^2)(S_{HH}^2 - S_{VV}^2)^* \rangle & 2\langle (S_{HH}^2 + S_{VV}^2)S_{HV}^{2*} \rangle \\ \langle (S_{HH}^2 - S_{VV}^2)(S_{HH}^2 + S_{VV}^2)^* \rangle & \langle |S_{HH}^2 - S_{VV}^2|^2 \rangle & 2\langle (S_{HH}^2 - S_{VV}^2)S_{HV}^{2*} \rangle \\ 2\langle S_{HV}^2 (S_{HH}^2 + S_{VV}^2)^* \rangle & 2\langle S_{HV}^2 (S_{HH}^2 - S_{VV}^2)^* \rangle & \langle 4|S_{HV}^2|^2 \rangle \end{bmatrix} \\
 [\Omega_{12}] &= \begin{bmatrix} \langle (S_{HH}^1 + S_{VV}^1)(S_{HH}^{2*} + S_{VV}^{2*}) \rangle & \langle (S_{HH}^1 + S_{VV}^1)(S_{HH}^{2*} - S_{VV}^{2*}) \rangle & 2\langle (S_{HH}^1 + S_{VV}^1)S_{HV}^{2*} \rangle \\ \langle (S_{HH}^1 - S_{VV}^1)(S_{HH}^{2*} + S_{VV}^{2*}) \rangle & \langle (S_{HH}^1 - S_{VV}^1)(S_{HH}^{2*} - S_{VV}^{2*}) \rangle & 2\langle (S_{HH}^1 - S_{VV}^1)S_{HV}^{2*} \rangle \\ 2\langle S_{HV}^1 (S_{HH}^{2*} + S_{VV}^{2*}) \rangle & 2\langle S_{HV}^1 (S_{HH}^{2*} - S_{VV}^{2*}) \rangle & \langle 4S_{HV}^1 S_{HV}^{2*} \rangle \end{bmatrix}
 \end{aligned} \tag{2.39}$$

$$\begin{aligned}
 [T_6] &= \begin{bmatrix} \langle |S_{HH}^1 + S_{VV}^1|^2 \rangle & \langle (S_{HH}^1 + S_{VV}^1)(S_{HH}^1 - S_{VV}^1)^* \rangle & 2\langle (S_{HH}^1 + S_{VV}^1)S_{HV}^{1*} \rangle & \langle (S_{HH}^1 + S_{VV}^1)(S_{HH}^{2*} + S_{VV}^{2*}) \rangle & \langle (S_{HH}^1 + S_{VV}^1)(S_{HH}^{2*} - S_{VV}^{2*}) \rangle & 2\langle (S_{HH}^1 + S_{VV}^1)S_{HV}^{2*} \rangle \\ \langle (S_{HH}^1 - S_{VV}^1)(S_{HH}^1 + S_{VV}^1)^* \rangle & \langle |S_{HH}^1 - S_{VV}^1|^2 \rangle & 2\langle (S_{HH}^1 - S_{VV}^1)S_{HV}^{1*} \rangle & \langle (S_{HH}^1 - S_{VV}^1)(S_{HH}^{2*} + S_{VV}^{2*}) \rangle & \langle (S_{HH}^1 - S_{VV}^1)(S_{HH}^{2*} - S_{VV}^{2*}) \rangle & 2\langle (S_{HH}^1 - S_{VV}^1)S_{HV}^{2*} \rangle \\ 2\langle S_{HV}^1 (S_{HH}^1 + S_{VV}^1)^* \rangle & 2\langle S_{HV}^1 (S_{HH}^1 - S_{VV}^1)^* \rangle & \langle 4|S_{HV}^1|^2 \rangle & 2\langle S_{HV}^1 (S_{HH}^{2*} + S_{VV}^{2*}) \rangle & 2\langle S_{HV}^1 (S_{HH}^{2*} - S_{VV}^{2*}) \rangle & \langle 4S_{HV}^1 S_{HV}^{2*} \rangle \\ \langle (S_{HH}^1 + S_{VV}^1)^*(S_{HH}^{2*} + S_{VV}^{2*}) \rangle & \langle (S_{HH}^1 + S_{VV}^1)^*(S_{HH}^{2*} - S_{VV}^{2*}) \rangle & 2\langle (S_{HH}^1 + S_{VV}^1)^* S_{HV}^{2*} \rangle & \langle |S_{HH}^2 + S_{VV}^2|^2 \rangle & \langle (S_{HH}^2 + S_{VV}^2)(S_{HH}^2 - S_{VV}^2)^* \rangle & 2\langle (S_{HH}^2 + S_{VV}^2)S_{HV}^{2*} \rangle \\ \langle (S_{HH}^1 - S_{VV}^1)^*(S_{HH}^{2*} + S_{VV}^{2*}) \rangle & \langle (S_{HH}^1 - S_{VV}^1)^*(S_{HH}^{2*} - S_{VV}^{2*}) \rangle & 2\langle (S_{HH}^1 - S_{VV}^1)^* S_{HV}^{2*} \rangle & \langle (S_{HH}^2 - S_{VV}^2)(S_{HH}^2 + S_{VV}^2)^* \rangle & \langle |S_{HH}^2 - S_{VV}^2|^2 \rangle & 2\langle (S_{HH}^2 - S_{VV}^2)S_{HV}^{2*} \rangle \\ 2\langle S_{HV}^1 (S_{HH}^{2*} + S_{VV}^{2*}) \rangle & 2\langle S_{HV}^1 (S_{HH}^{2*} - S_{VV}^{2*}) \rangle & \langle 4S_{HV}^1 S_{HV}^{2*} \rangle & 2\langle S_{HV}^2 (S_{HH}^2 + S_{VV}^2)^* \rangle & 2\langle S_{HV}^2 (S_{HH}^2 - S_{VV}^2)^* \rangle & \langle 4|S_{HV}^2|^2 \rangle \end{bmatrix}
 \end{aligned}$$

PolInSAR coherence ( $\gamma$ ) is a complex vector quantity described in (S. Cloude and K. P. Papathanassiou, 2003) Eq. 2.40.

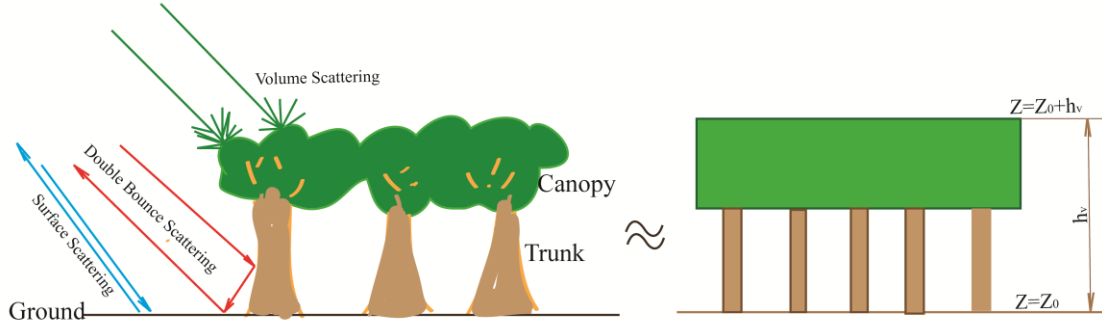


Figure 2.3 Pictorial representation of the three dominant scattering mechanisms occurring in forest-stand and the equivalent Random Volume Over Ground Scattering model.

$$\frac{|\langle \omega_1^{*T} [\Omega_{12}] \omega_2 \rangle|}{\sqrt{\langle \omega_1^{*T} [T_{11}] \omega_1 \rangle \langle \omega_2^{*T} [T_{22}] \omega_2 \rangle}} \quad (2.40)$$

The two normalized complex vectors  $\omega_1$  and  $\omega_2$  represent different polarization basis. The derivation of the complex vectors is provided in Sec. 4.2. Coherence maps in different polarizations depict the scattering contributions of different scatterers (Cloude and Papathanassiou, 1998). Coherences in different polarizations such as HH, HV, VH and VV can be obtained for H, V-polarization basis. Basis transformations (Sec. 2.5) are applied for estimation of coherence in different polarization basis such as Linear, Pauli, Circular and Optimal. Each coherence represents a dominant scattering mechanism. For e.g., the cross-polarized HV coherence generally represents the dominant volume scattering. Separation of underlying scattering mechanisms require coherence optimization as proposed in (Cloude and Papathanassiou, 1998) for Gaussian distribution of PolInSAR data. Yong and Mercer (Yong Bian and Mercer, 2010) have generalized the optimization process which also applies to non-Gaussian PolInSAR data. Various alternative approaches for coherence optimization are proposed in (Yong Bian and Mercer, 2010) while (Binghuang and Bing, 2007) presents a comparative study of optimization techniques. The coherence optimization approach of (Cloude and Papathanassiou, 1998) has been utilized in the present work for estimation of three optimum coherences.

The present work utilizes the acquired PolInSAR data for estimation of forest-stand height and vertical structure. It utilizes the techniques developed in (S. Cloude and K. P. Papathanassiou, 2003; Cloude and Papathanassiou, 1998; Cloude, 2006) for the study. The next section details the forest stand height estimation techniques.

## 2.8 Vegetation height estimation using PolInSAR

The training course on PolInSAR (Cloude, 2005) provides an insight into techniques and algorithms developed for forest-stand height estimation. A very simple technique for vegetation height estimation is to generate DEM's corresponding to two polarizations representing the scattering at top and bottom of the vegetation layer, and to differentiate them to find the height of the vegetation layer (Cloude, 2006, 2005). However, the scattering phase center was found to lie

(Cloude, 2006, 2005) anywhere between the top of the canopy and half the tree height and the location depended on the wave extinction in the scattering media and the structure of the vertical canopy. Various techniques (S. Cloude and K. P. Papathanassiou, 2003; Mette, 2006; Neumann et al., 2010; Papathanassiou and Cloude, 2001) have been proposed to factor the effects of wave extinction and vertical canopy structure. A second technique applied in this work is the ‘Coherence Amplitude Inversion’ (CAI) technique. The coherence is inversely related to the volume density or density of vegetation/forest layer. As the density of forests increases, the volume decorrelation also increases leading to decrease in coherence. CAI applies this phenomenon to estimate the height of the vegetation layer. Two polarization channels are selected much the same as for DEM differencing height, one dominated by surface scattering and the other by volume scattering. CAI can be applied to estimate the height using estimates for extinction in the volume layer. The present work investigates the ‘Three-stage inversion’ technique (S. Cloude and K. P. Papathanassiou, 2003). The ‘Three-stage inversion’ (TSI) technique uses the two-layer model for vegetation (S. Cloude and K. P. Papathanassiou, 2003). TSI technique observes the complex coherence in different polarizations and predicts the ground topography and polarization-independent volume coherence using least squares technique. The technique considers the effects of temporal decorrelation on estimation of height of the vegetation layer. (Lee *et al.*, 2006) presents a detailed study on the effects of temporal decorrelation on PolInSAR data. A detailed mathematical approach on Three Stage Inversion technique is provided in Appendix 2.

This brief literature can also include several research works carried out in the past and the present. The reader is referred to the material cited in the references at the end of the thesis. The next section presents the study area for the current research work and the data sets employed for achieving the objectives.

### 3. STUDY AREA AND MATERIALS

This chapter provides insight into the study area for the present work and details the data sets utilized. The chapter is divided into two sections – Section 3.1 provides details on the study area and Section 3.2 on the satellite and field based data used for the study.

#### 3.1 Study Area

The present work was carried out on Barkot and Thano Forest range in Uttarakhand State, India. The Barkot and Thano forest ranges are tropical forests located between the Shivalik and Gharwal ranges of the Himalayas. The Barkot forest range is shown in Figure 3.1 bordered to the east by the River Ganges and Rishikesh city. The Thano forest range lies to the north-west of Barkot forest range and to the north of Jollygrant Airport, Dehradun.

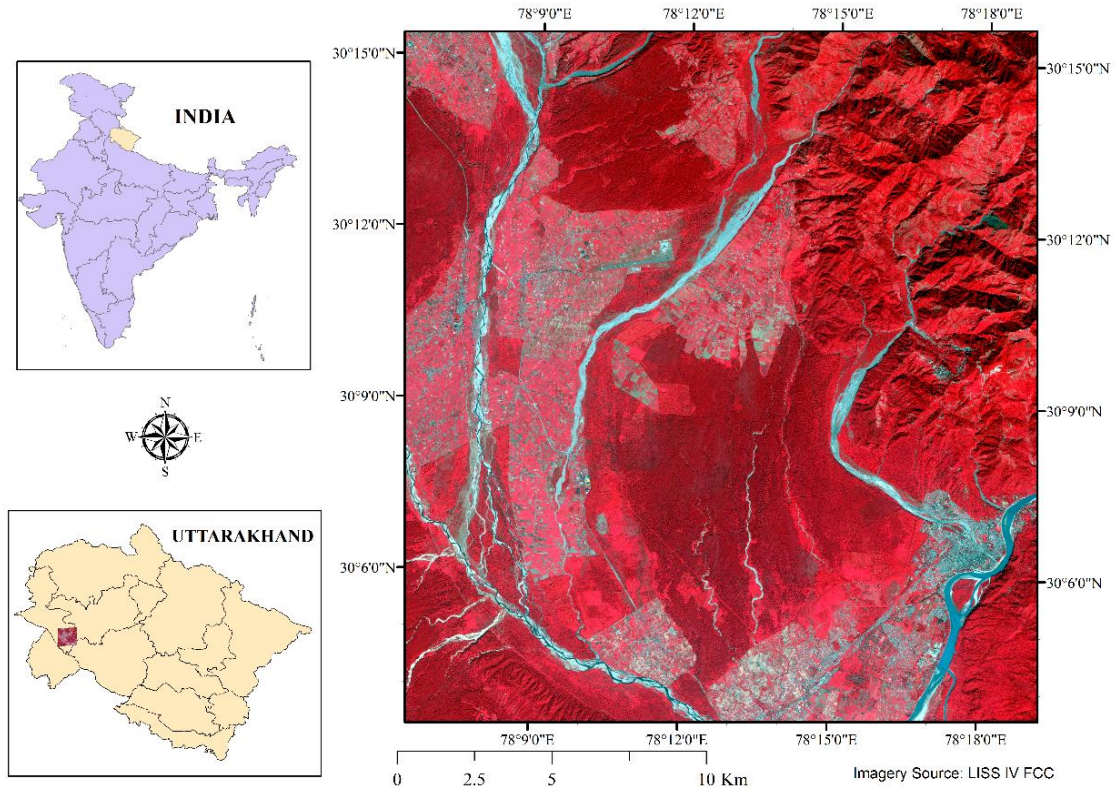


Figure 3.1 Study Area - Barkot and Thano Forest Range. The figure presents LISS IV acquired FCC image of the study area. The forest range in the center of the image is the Barkot forest range. Thano forest range lies to the north of the Barkot forest range.

The forest range is dominated by Sal (*Shorea robusta*) trees with the other dominating species being Teak (*Tectona grandis*), Sisoo (*Dalbergia sisoo*) and Khair (*Senegalia catechu*). The forest ranges cover a total area of around 150 sq.km.

Figure 3.2 provides the distribution of the major forest species in the Barkot and Thano forest ranges. The data is courtesy Forest Department, Uttarakhand State.

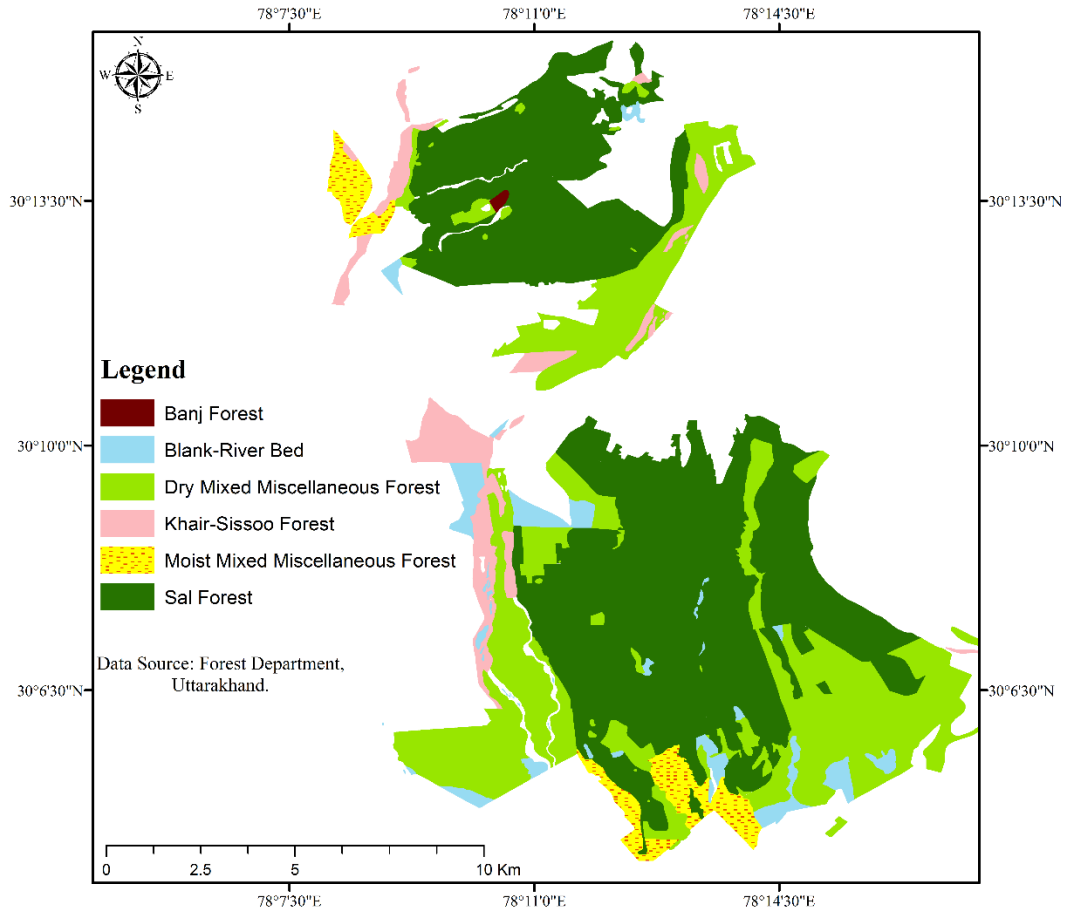


Figure 3.2 Forest Type map for Barkot and Thano forest range. Sal species dominates the forest ranges. Teak species dominates the Dry Mixed Miscellaneous forest regions and the other major species are the Khair and Sissoo.

### 3.2 Materials

This section provides information on the various data sets used. The first section details the satellite data utilized and the second section provides information on the *in situ* data collected for validation.

#### 3.2.1 Satellite data

Fully polarimetric, space borne data acquired from ALOS PALSAR, RADARSAT-2 and TERRASAR-X have been used for the study on the effect of POA shift. A brief on the data sets is provided in Table 3.1. The data sets used are of level 1.1 which signify that the data are not geocoded and in SLC (Single Look Complex) format. Each pixel information is provided in complex format which contains the phase and the amplitude information.

Polarimetric Interferometric SAR data from RADARSAT-2 satellite is acquired over Barkot forest range in Uttarakhand State of India during March 2013 (see Table 3.2). The RADARSAT-2 is a Canadian satellite launched on December 14, 2007. It has a Synthetic Aperture Radar (SAR) Sensor operating in C-band with capability to acquire data in all the four polarizations - HH, HV, VH and VV. The data used for this study is a SAR data pair acquired in Fine Quad-polarization with similar geometrical configuration over a temporal baseline of 24 days, to generate a PolInSAR data pair. The characteristics of this PolInSAR data is presented in Table 3.2.

Table 3.1 Data Characteristics of Multi-frequency PolSAR Data

Satellite-Sensor	ALOS/ PALSAR	RADARSAT-2	TERRASAR -X
Wavelength (cm)	23.6	5.55	3.10
Frequency Band	L Band	C Band	X - Band
Date of Acquisition	09-Dec-2009	07-Nov-2012	30-Apr-2010
Polarization	Quad -pol	Quad -pol	Quad -pol
Orbit Direction	Ascending	Descending	Descending
Incidence Angle (°)	23.13	30.26	38.05
Centre Latitude (°)	32.3648	32.2675	32.381216
Centre Longitude (°)	77.08	77.1575	77.1352

Table 3.2 Data Characteristics of PolInSAR Data Pair

Acquisition	Pass I	Pass II
Satellite-Sensor	RADARSAT-2	RADARSAT-2
Wavelength (cm)	5.55	5.55
Frequency Band	C Band	C Band
Date of Acquisition	04-Mar-2013	28-Mar-2013
Polarization	Quad -pol	Quad -pol
Antenna Pointing	Right	Right
Near Incidence Angle (°)	39.2836	39.2875
Far Incidence Angle (°)	40.7299	40.7335
Centre Latitude (°)	30.1707	30.1685
Centre Longitude (°)	78.1866	78.1840

### 3.2.2 Field Survey

Field survey was carried out in the month of March, 2014. The ground survey was carried out during 10<sup>th</sup> March 2014 to 25<sup>th</sup> March 2014. The satellite data was acquired in March 2013, hence the field work was planned during the same season. The forest is dominated by Sal forest. The Sal trees are mature and the tree height change should be minimal during one season. To account for the effects of leaf-fall during the early spring, especially in Teak, Khair and Sisoo species, the field work is carried out during the same season as the data acquisition.

Forest Department of Uttarakhand State provided maps for the forest regions detailing the forest-type and access fire lines and forest-paths. This data was used to plan the field sample collection. The pie-chart in Figure 3.4 shows the area wise species distribution in Barkot and Thano forests. It is observed that over 57% of the Barkot and Thano forest range is dominated by Sal (*Shorea robusta*) and the other major species being Teak (*Tectona grandis*), Sisoo (*Dalbergia sisoo*) and Khair (*Acacia catechu*). The Dry-mixed forest type comprises of stretches of Teak and Sal along with various different species.



Figure 3.3 Left: Barkot Forest Range. Right: Forest stand comprising chiefly of Sal trees.

The plots are distributed based on the spatial coverage of the tree-species. The access to certain forest regions, particularly in the western region of Barkot forest range is restricted as it is a very active Elephant corridor, and is dangerous to conduct field surveys. Hence the plots are sparse in the region.

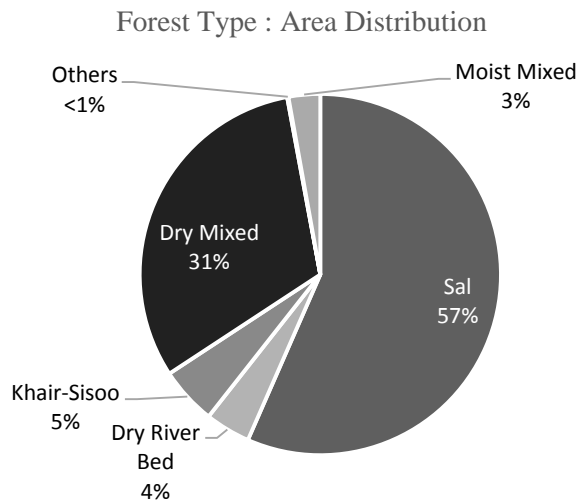


Figure 3.4 Pie chart showing the area wise distribution of different species in the study area.

Plots with each side of 12.5 meter were used. The plot size was chosen to match the spatial resolution of the RADARSAT-2 acquired multi-looked data. Figure 3.5 depicts the methodology followed for the plotting. The geo-location was obtained using Trimble Juno SB handheld GPS

receiver. The positional error in the reading was observed between 7 m – 10 m with the average positional error of 8m. The accuracy of the GPS reading decreases with increasing canopy density.

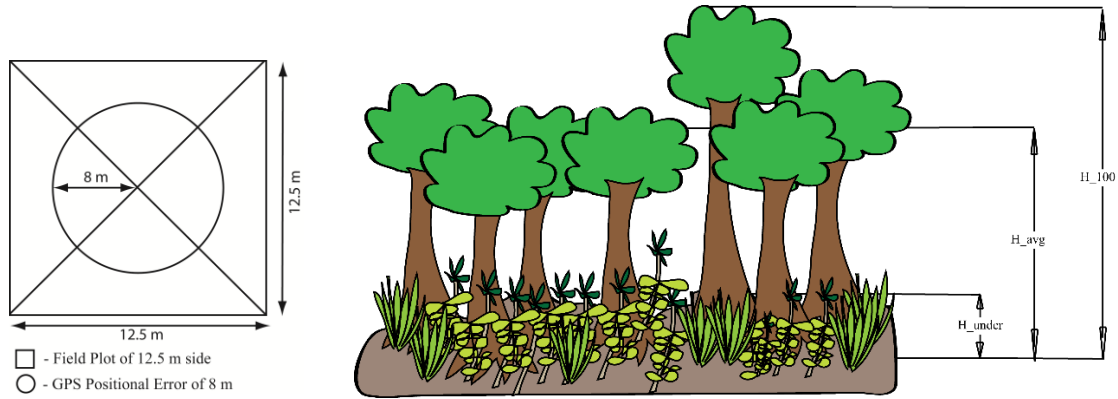


Figure 3.5 Left: Field plots of 12.5 meter each were plotted as shown. The GPS location was obtained using Trimble Juno SB handheld GPS. The average positional error observed is 8 meter as depicted using the circle. Right: The field height measurements in each plot. The measurements are noted for the highest tree – H\_100, average tree height – H\_avg and the understory height – H\_under of the plot.

The tree height was measured using Criterion RD1000 Laser Dendrometer with the aid of Leica Disto D8 Laser Distance meter. The highest measured tree height is quantified as H\_100 (Mette *et al.*, 2004; Zhang *et al.*, 2008), the average measured tree height for each plot as H\_avg and the understory height as H\_under. Following table provides the instrument details and mode of operation of Criterion RD 1000 Laser dendrometer. The instrument is accurate up to 0.1m.

Table 3.3 Criterion RD1000 Laser Dendrometer Specifications

Mode of Usage	Least Count of Angular Measurement	Least Count of Height Measurement	Range of Height Measured
Height/ Diameter Mode	1 degree	0.1 meters	0.51m – 304.76m

100 plots are taken in the Thano and Barkot forest region. The field survey data is tabulated in Appendix I. It contains information on the geo-location and the average tree height of the plot (H\_avg). The average height measured for all the plots is 23.90 meter and the average of the highest tree height in all plots is 26.6 meter. Figure 3.6 shows the field data collection locations distributed throughout the Barkot and Thano forest ranges. Data from plots are collected in the accessible areas of the forests. Certain areas have very dense lantana or are in active elephant corridors. The field data could not be collected in such areas.

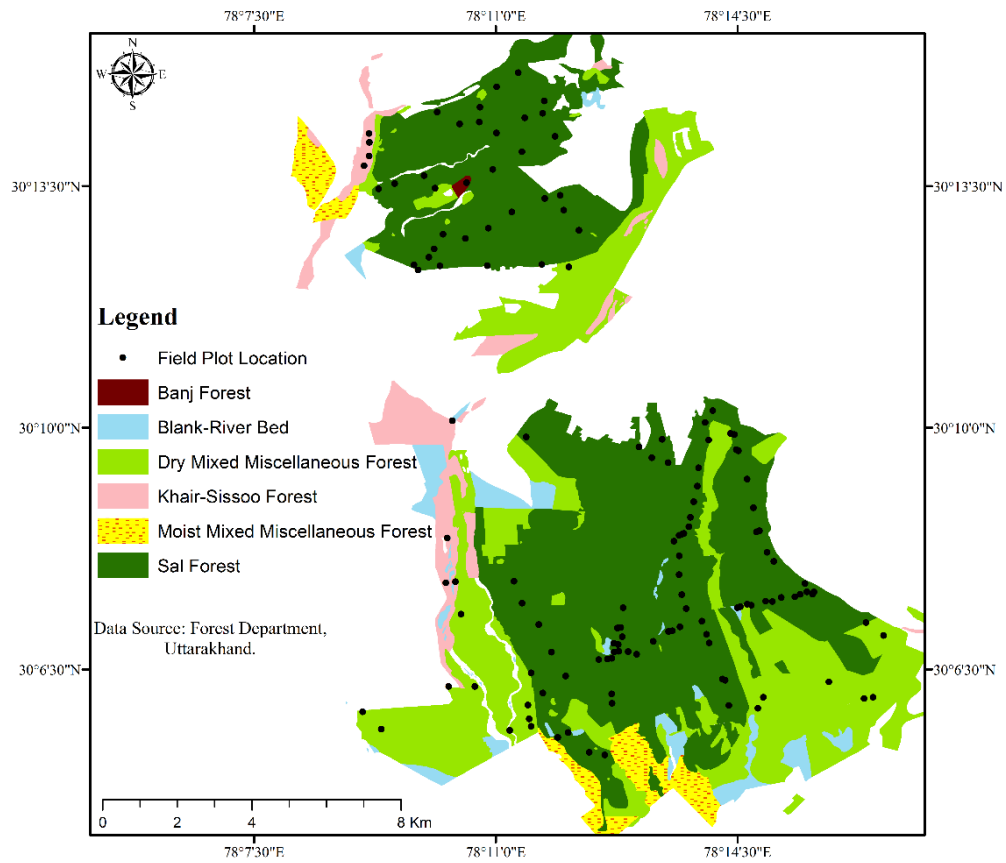


Figure 3.6 Field work and in situ data collection.



Figure 3.7a Field Photographs depicting the understory in forest area.



Figure 3.7b Dense Lantana understory in Thano Forest Range.



Figure 3.7c Dense Understory in Barkot Forest Range.

Figure 3.7 Field photographs depicting understory in Thano and Barkot Forest Range.

The understory height may be a contributing factor in the height derived from SAR data. At C-band the SAR wave has less penetration through dense canopy. Dense understory is present in both Barkot and Thano forest range. Prominently in Thano forest range, invasive species such as Lantana (*Viburnum lantana*) are present in dense clusters with height up to 2m rendering the forest impenetrable at many locations. The dominant species which form the understory is the Curry tree (*Murraya koenigi*) growing between 3m -7m tall.

## **4. METHODOLOGY**

---

The research work aims to study two major topics - POA (POA) shift and PolInSAR based vertical height estimation of forest-stand. The methodology for studying both these SAR phenomenon is described in this chapter.

### **4.1 Orientation Angle Shift**

The shift in polarization orientation is induced due to various reasons as discussed in Sec. 2.6. The present work aims to study the effect of POA Compensation on multi-frequency PolSAR data.

#### **4.1.1 Estimation of Induced Shift in Orientation Angle and its Compensation**

Fully polarimetric SAR data acquired from space-borne satellites is used for the study. Data sets available in L-, C- and X-band are utilized. Assuming reciprocity, Scattering matrix [S] is derived which provides a relation between the scattered Electromagnetic (EM) wave ( $E_s$ ) and the incident EM wave ( $E_i$ ) (Jin and Xu, 2013) as given by (1)

$$E_s = [S]E_i \quad (4.1)$$

Coherence matrix [T] is calculated from the scattering matrix. The coherence matrix is used as it is closely related to the physical properties of the scattering medium (Cloude and Pottier, 1996) and the scattering characteristics contained are derived using the second-order statistics of its scattering matrices (Yamaguchi *et al.*, 2005). Using the Yamaguchi decomposition (Yamaguchi *et al.*, 2006), the coherence matrix [T] is decomposed into four scattering mechanisms- volume, double-bounce, surface and helix scattering. These decomposed products are used as the basis for estimation of effect of POA on SAR data. The derived coherence matrix [T] and Yamaguchi decomposed products are those obtained before compensating for the shift introduced due to POA. The Yamaguchi decomposed scattering power is denoted as  $P_d, P_v, P_s$  and  $P_c$  for double-bounce, volume, surface and helix scattering power respectively. The next stage involves estimation of Orientation angle and its compensation.

The OA induced is calculated based on the circular polarization technique proposed in (Lee *et al.*, 2002, 2000) and briefly reviewed in (Lee and Ainsworth, 2011). The coherence matrix [T] is compensated for the induced OA shift and a compensated coherence matrix [ $\bar{T}$ ] is derived. [ $\bar{T}$ ] theoretically represents the physical properties of the scattering material better than the uncompensated matrix [T].

Yamaguchi decomposed products of the rotated coherence matrix are derived. The scattering power of the Yamaguchi decomposed products are denoted by  $\bar{P}_d, \bar{P}_v, \bar{P}_s$  and  $\bar{P}_c$ , for double-bounce, volume, surface and helix scattering power respectively. Here the superscript bar ( $\bar{\quad}$ ) denotes the scattering power after POA compensation. The derived Yamaguchi decomposed

power before and after POA compensation are compared for further analysis. The methodology is applied to fully polarimetric SAR data from L-band ALOS PALSAR, C-band RADARSAT-2 and X-band TERRASAR-X.

#### **4.1.2 Effect of Orientation Angle Shift on PolInSAR data and height retrieval**

The 6x6 coherence matrix [T6] is the main observable in PolInSAR data (Cloude and Papathanassiou, 1998). The vectorial representation of the scattering matrix in Pauli basis is given by the scattering vector

$$\underline{k} = [S_{HH} + S_{VV} \quad S_{VV} - S_{HH} \quad 2S_{HV}]^T \quad (4.2)$$

The [T6] matrix is formed by the outer product of the two scattering vectors  $\underline{k}_1$  and  $\underline{k}_2$  for images I1 and I2 of the two Interferometric acquisitions. It is thus clear that the methodology used earlier to estimate the shift in POA cannot be used in the case of PolInSAR data as the 3x3 coherence matrix [T] is not utilized. Hence the shift in POA is calculated on the scattering matrix [S] for the two acquisitions and the necessary compensation is carried out.

The derived, induced POA is  $\theta$ . Now the [S] matrix is rotated by  $\theta$ , thus compensating for the shift induced due to sloping terrain and urban structure not aligned along the azimuth direction. Equation (4.3) derives the compensated scattering matrix  $[\bar{S}]$  (Lee *et al.*, 2002),

$$[\bar{S}] = [U][S][U] \quad (4.3)$$

$$[\bar{S}] = \begin{bmatrix} \cos \theta & \sin \theta \\ -\sin \theta & \cos \theta \end{bmatrix} \begin{bmatrix} S_{HH} & S_{HV} \\ S_{HV} & S_{VV} \end{bmatrix} \begin{bmatrix} \cos \theta & -\sin \theta \\ \sin \theta & \cos \theta \end{bmatrix}$$

Note that the "-" on top of matrix [S] denotes the scattering matrix after rotation of angle  $\theta$ . The matrix [U] is the 2x2 unitary matrix and [S] is the scattering matrix before compensating for orientation angle and  $[\bar{S}]$  is the scattering matrix after compensation. The same process is followed for both the acquisitions and two new scattering matrices  $[\bar{S}_1]$  and  $[\bar{S}_2]$  are generated after POA compensation. New target vectors  $\bar{\underline{k}}_1$  and  $\bar{\underline{k}}_2$  are generated and a new 6x6 coherence matrix  $[\bar{T}_6]$  is calculated.  $[\bar{T}_6]$  is the main observable for PolInSAR data post-compensation for shift in POA. Height and other physical parameters are derived from the new  $[\bar{T}_6]$  matrix.

#### **4.2 PolInSAR Based Tree Height Estimation**

The basic observable in PolInSAR data is the 6x6 coherence matrix and its derivation is explained in the previous section. This section presents in detail the methods followed for generation of  $[\bar{T}_6]$  matrix and retrieval of forest-stand vertical profile.

PolInSAR data consists of two acquisitions made over the same region with same geometrical configuration. Here, two RADARSAT-2 acquisitions made over a temporal baseline of 24 days is used. The acquired RADARSAT-2 data is calibrated to radar backscatter coefficient ( $\sigma^0$ ) using the Sigma Nought Calibration look-up table, to generate the backscattering Scattering matrix [S].  $[S_1]$  and  $[S_2]$  denote the scattering matrices generated for the two passes- Pass I and Pass II- respectively.

$$[S_1] = \begin{bmatrix} S_{1HH} & S_{1HV} \\ S_{1VH} & S_{1VV} \end{bmatrix} \quad \text{and} \quad [S_2] = \begin{bmatrix} S_{2HH} & S_{2HV} \\ S_{2VH} & S_{2VV} \end{bmatrix} \quad (4.4)$$

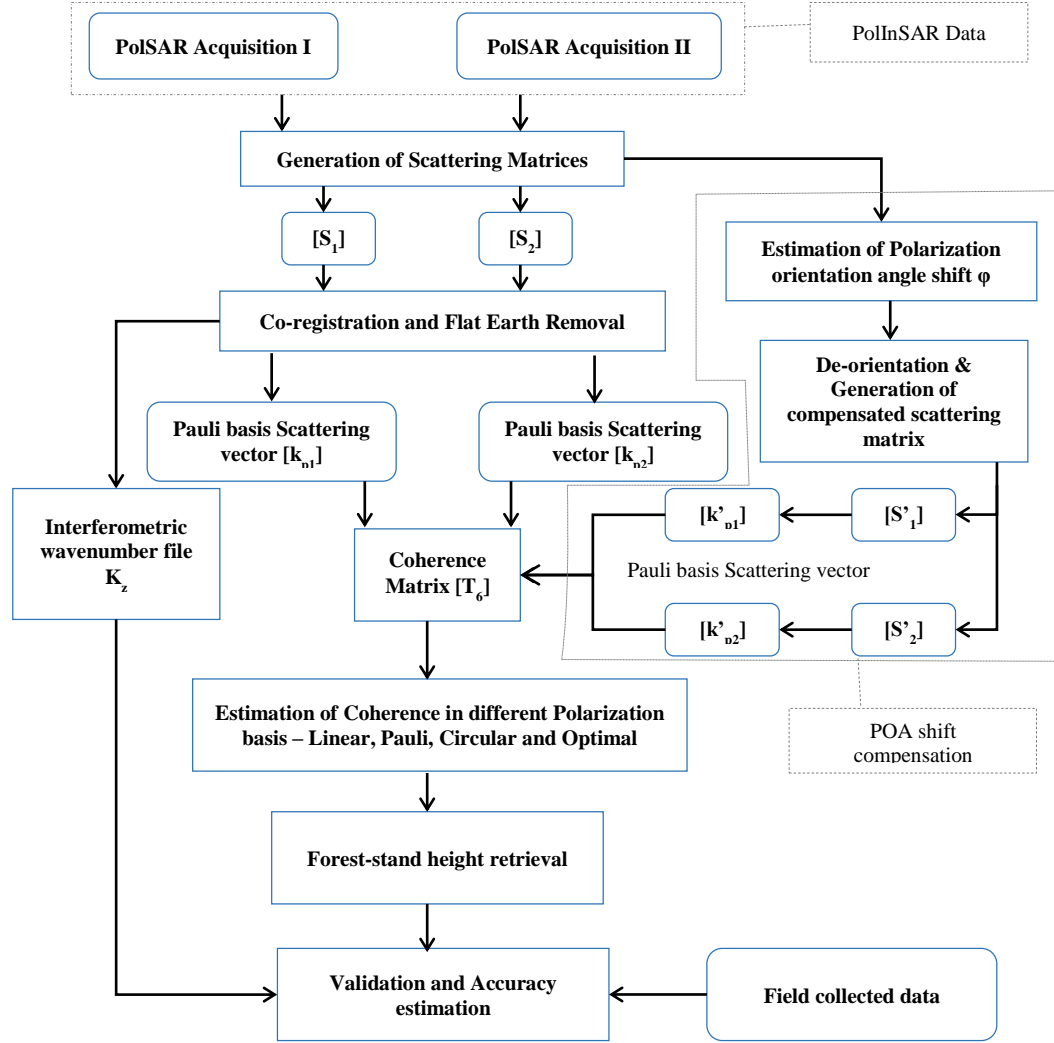


Figure 4.1 Methodology flow chart for Forest-stand height retrieval and study of POA shift on PolInSAR data.

**Co-registration:** To ensure that a pixel at same location in both images provides backscattering information for the same ground location, co-registration is performed on the two scattering matrices. Coarse Co-registration with a window size of 1024 rows and 254 columns at random five locations. Then fine co-registration is carried out at the random locations and a final shift in the rows and columns is estimated. Using this input, the two acquisitions are co-registered to each other. Now the backscatter for a pixel from both acquisitions is for the same ground feature.

**Calculation of Interferometric Wavenumber ( $k_z$ ):** Interferometric wavenumber provides the relationship between the interferometric phase ( $\phi$ ) and elevation of the scatterer ( $h_0$ ) (Cloude, 2008) as shown in Eq. 4.5.

$$\phi = k_z h_0 \quad (4.5)$$

$k_z$  is a function of incidence angle and wavelength and is given by (Cloude, 2008):

$$k_z = \frac{4\pi\Delta\theta}{\lambda \sin\theta} \quad (4.6)$$

where,

$$\Delta\theta = \theta_1 - \theta_2 \text{ and } \theta = \frac{\theta_1 + \theta_2}{2} \quad (4.7)$$

$\theta_1$  and  $\theta_2$  are the incidence angles of the two images  $I_1$  and  $I_2$  respectively.  $\Delta\theta$  provides the difference of the incidence angle,  $\theta$  is the average incidence angle and  $\lambda$  is the wavelength at which the data is acquired. Using Eq. 4.6, the  $k_z$  file is generated. This file is required to estimate the height of the forest-stand.

**Generation of 6x6 Complex Coherence Matrix [ $T_6$ ]:** Once the Scattering matrices for the two acquisitions are generated and co-registered, a PolInSAR data pair is formed. Coherent scattering vector  $\underline{k}$  is used for vectorization of the scattering matrix [S] (Cloude and Papathanassiou, 1998) given by

$$\underline{k} = \frac{1}{2} \text{Trace}([S]\psi_p)$$

$$\underline{k} = \frac{1}{\sqrt{2}} [S_{HH} + S_{VV}, \quad S_{VV} - S_{HH}, \quad S_{HV} + S_{VH}, \quad i(S_{HV} - S_{VH})]^T. \quad (4.8)$$

The superscript  $.^T$  represents the transpose of a matrix and  $S_{HH}$ ,  $S_{HV}$ ,  $S_{VH}$  and  $S_{VV}$  are the elements of the scattering matrix with the first letter of subscript representing the received polarization and second letter the transmitted polarization in HV-polarization basis.  $\psi_p$  is the set of 2x2 complex Pauli basis matrices (Cloude and Papathanassiou, 1998)

$$\psi_p = \left\{ \sqrt{2} \begin{bmatrix} 1 & 0 \\ 0 & 1 \end{bmatrix}, \quad \sqrt{2} \begin{bmatrix} 1 & 0 \\ 0 & -1 \end{bmatrix}, \quad \sqrt{2} \begin{bmatrix} 0 & 1 \\ 1 & 0 \end{bmatrix}, \quad \sqrt{2} \begin{bmatrix} 0 & -i \\ i & 0 \end{bmatrix} \right\} \quad (4.9)$$

The physical scattering mechanisms and wave scattering physics can be closely modelled by the use of Pauli basis (Cloude and Papathanassiou, 1998). Hence the Pauli basis is selected from the various orthogonal basis sets available for vectorization of [S] (Cloude and Pottier, 1996). As the medium considered is reciprocal, the scattering vector  $\underline{k}$  is reduced to a three-dimensional scattering vector as given in (4.10)

$$\underline{k} = [S_{HH} + S_{VV} \quad S_{VV} - S_{HH} \quad 2S_{HV}]^T \quad (4.10)$$

As explained in Section 2.7, the coherence matrix [ $T_6$ ] is defined as:

$$[T_6] := \left\langle \begin{bmatrix} \underline{k}_1 \\ \underline{k}_2 \end{bmatrix} \begin{bmatrix} \underline{k}_1^{*T} & \underline{k}_2^{*T} \end{bmatrix} \right\rangle = \begin{bmatrix} [T_{11}] & [\Omega_{12}] \\ [\Omega_{12}]^{*T} & [T_{22}] \end{bmatrix} \quad (4.11)$$

[ $T_{11}$ ] and [ $T_{22}$ ] are the same as the Hermitian coherence matrix formed from the multiplication of scattering vector of a single image with its complex conjugate, and contains the full polarimetric information for that image (Cloude and Papathanassiou, 1998) and is given as

$$[T_{11}] = \langle \underline{k}_1 \underline{k}_1^{*T} \rangle, \quad [T_{22}] = \langle \underline{k}_2 \underline{k}_2^{*T} \rangle, \quad [\Omega_{12}] = \langle \underline{k}_1 \underline{k}_2^{*T} \rangle \quad (4.12)$$

$[\Omega_{12}]$  is a 3x3 complex matrix which has both the polarimetric and interferometric information. This matrix provides the interferometric phase relations of different polarimetric channels from the two acquisitions (Cloude and Papathanassiou, 1998).

**Estimation of Coherences in different polarization basis:** Cloude and Papathanassiou (Cloude and Papathanassiou, 1998) have defined the interferometric coherence as a function of the coherence matrix elements and polarization basis as

$$\gamma = \frac{|\langle \omega_1^{*T} [\Omega_{12}] \omega_2 \rangle|}{\sqrt{\langle \omega_1^{*T} [T_{11}] \omega_1 \rangle \langle \omega_2^{*T} [T_{22}] \omega_2 \rangle}} \quad (4.13)$$

The two normalized complex vectors  $\omega_1$  and  $\omega_2$  can be interpreted as two scattering mechanism. The derivation of these vectors can be referred in Appendix section of (Cloude and Papathanassiou, 1998). For making this work self-sufficing the derivation is provided based largely on the derivation made by Cloude and Papathanassiou (Cloude and Papathanassiou, 1998). For a general Scattering matrix [S] given by

$$[S] = \begin{bmatrix} a & b \\ b & c \end{bmatrix}, \quad (4.14)$$

Pauli basis scattering vector  $\underline{k}$  can be written as

$$\underline{k} = \frac{1}{\sqrt{2}} [a + c, a - c, 2b]^T = |\underline{k}| \omega. \quad (4.15)$$

Where  $\omega$  is a unitary complex vector with a general form given by (Cloude and Papathanassiou, 1998)

$$\omega = \begin{bmatrix} \cos \alpha \exp i\phi \\ \sin \alpha \cos \beta \exp i\delta \\ \sin \alpha \sin \beta \exp i\gamma \end{bmatrix}. \quad (4.16)$$

Cloude and Papathanassiou propose a Scattering Vector Theorem (Cloude and Papathanassiou, 1998): "it is always possible to reduce an arbitrary scattering mechanism, represented by a complex unitary vector  $\omega$  to the identity  $[1 \ 0 \ 0]^T$  by the following set of ordered matrix transformations" Eq. (4.17). The first two matrices represent the mathematical canonical form of plane rotations. The third matrix represent a set of scattering phase angles. The angle  $\beta$  physically represents the orientation of the scatterer about the radar line of sight for Pauli basis vectorization of the scattering matrix (Cloude and Papathanassiou, 1998; Cloude and Pottier, 1996), while the angle  $\alpha$  provides the internal degree of freedom of the scatterer.  $\alpha \in [0^\circ, 90^\circ]$ , with the angle representing the type of scattering mechanism. For  $\alpha = 90^\circ$ , isotropic dihedral or helical scattering occurs, for  $\alpha = 0^\circ$  an isotropic surface is present and for  $\alpha = 45^\circ$  a dipole scatterer is present. For angles between  $0^\circ$  and  $90^\circ$  anisotropic scattering mechanisms occur.

$$\begin{bmatrix} 1 \\ 0 \\ 0 \end{bmatrix} = \begin{bmatrix} \cos \alpha & \sin \alpha & 0 \\ -\sin \alpha & \cos \alpha & 0 \\ 0 & 0 & 1 \end{bmatrix} \cdot \begin{bmatrix} 1 & 0 & 0 \\ 0 & \cos \beta & \sin \beta \\ 0 & -\sin \beta & \cos \beta \end{bmatrix} \cdot \begin{bmatrix} \exp(-i\phi) & 0 & 0 \\ 0 & \exp(-i\delta) & 0 \\ 0 & 0 & \exp(-i\gamma) \end{bmatrix} \omega \quad (4.17)$$

From Eq. 4.13 the complex interferometric coherence is calculated with  $\omega_1$  and  $\omega_2$  defining the polarization basis. Using the concept of Polarization Basis transformation explained in Section 2.4, scattering matrices for other orthogonal (A, B)-basis can be calculated. For the present study,

the scattering matrix for Circular, Pauli and Optimal basis were derived and the respective complex coherences were calculated. The Optimal polarization basis states were derived using Cloude and Papathanassiou coherence maximization procedure (Cloude and Papathanassiou, 1998)

Now, complex coherence images are obtained for four polarization basis, namely – Linear Basis (HH, HV, VV), Pauli Basis (HH+VV, HH-VV, 2HV), Circular Basis (RR, LL, LR), Cloude and Papathanassiou coherence maximization procedure based Optimal Basis (Opt1, Opt2, Opt3). These 12 complex coherences are used in the next steps for vegetation height retrieval.

**Vegetation Height Retrieval using ‘Three Stage Inversion Model’:** The ‘Three Stage Inversion Model’ was developed by Cloude and Papathanassiou (Cloude and Papathanassiou, 2003). The ‘Three Stage Inversion Model’ is explained in detail in Appendix 2. This is the principle technique utilized in this study for vegetation height retrieval. The study also proposes improvements over the model using coherence and backscatter based approach. The improved-technique is explained in the next section.

The ‘Three Stage Inversion’ technique assumes existence of polarization independent volume coherence (Cloude and Papathanassiou, 2003). This is true in case of random volume over ground (RVoG) model as the vegetation layer does not have any specific orientation and the interaction of SAR wave is not a function of its polarization (Lopez-Martinez and Alonso-Gonzalez, 2014). However, in case of plantations, orchards and certain agricultural fields, this may not be true as the oriented volume layer can now be characterized by an oriented volume over ground model. For the present study, the ‘Three Stage Inversion’ technique is used for the estimation of vegetation layer height for the Barkot and Thano forest.

#### **4.3 Improved ‘Three Stage Inversion’ technique for vegetation height estimation**

The height retrieved from the ‘Three stage inversion’ technique was evaluated and compared with field data. It was observed that inaccuracies in estimation of height were present for urban regions, agricultural fields and dry riverbeds. These were the areas where the ground scattering contribution is higher, i.e. ground-to-volume scattering ratio is high. The ground-to-volume ratio is essentially a measure of density of volume/vegetation layer. Barren and agricultural fields and urban regions provide higher ground scattering contribution as compared to volume scattering. This leads to positive ground-to-volume scattering ratio. The technique cannot be utilized in agricultural and barren fields, dry riverbeds and urban areas. This can be attributed to the fact that, the technique models the vegetation on RVoG model, and this model would fail in case if sparse or no vegetation is present. The main assumption of the ‘Three Stage Inversion’ technique is the presence of polarization independent volume coherence (Cloude and Papathanassiou, 2003). This assumption stands true for forest regions as the trees do not have any specific orientation and interaction of radar waves in different polarizations is random in nature. However for agricultural fields with rows of crops in a specific orientation, the scattering of radar waves is a function of wave polarization, reducing the presence of polarization independent volume coherence. Hence, the technique does not provide accurate results for these regions. Also the

technique provides accurate results if the minimum ground-to-volume scattering ratio is less than -10 dB (Cloude and Papathanassiou, 2003). This is not the case for non-forested regions.

The improved ‘Three Stage Inversion’ technique provides additional inputs of complex coherence and radar backscatter for delineation of forested and non-forested areas as shown in Figure 4.2.

The non-forest regions are broadly categorized here in two classes - water regions and dry land

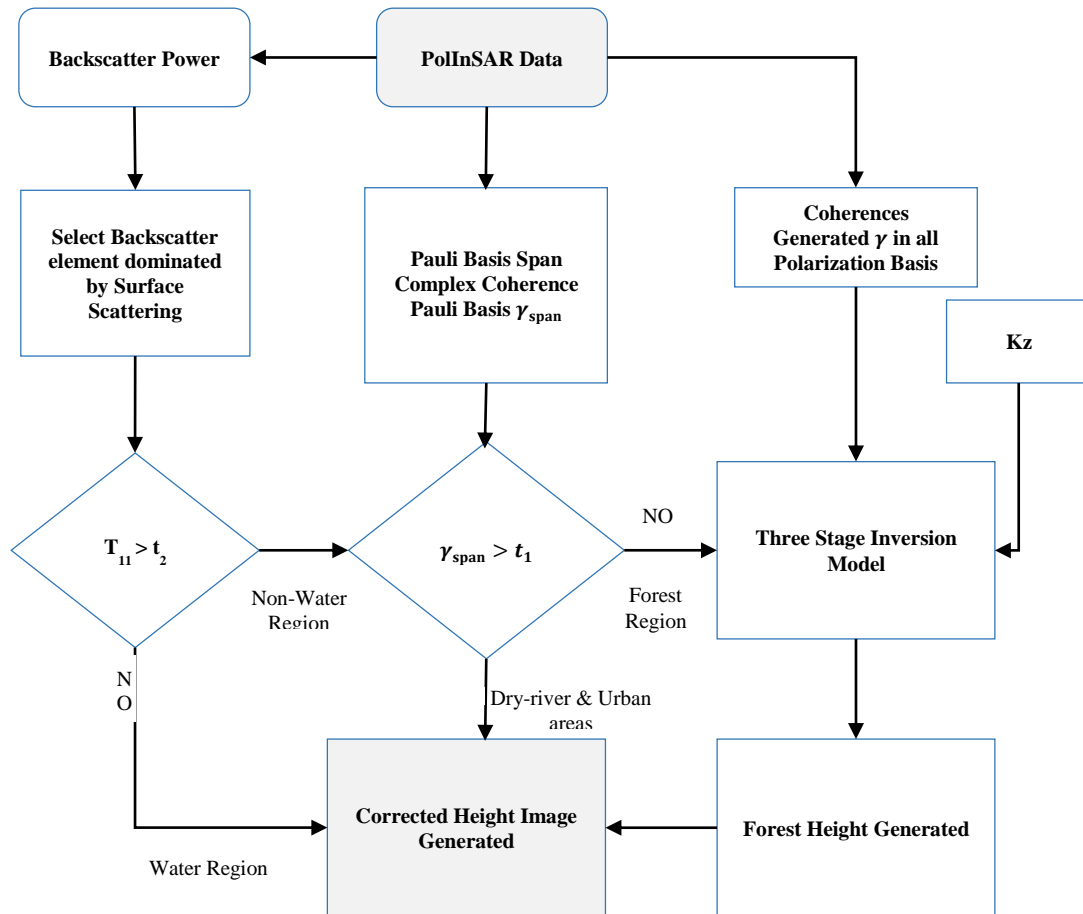


Figure 4.2 Flow chart for the ‘Improved Three Stage Inversion Technique’ for accurate estimation of height in forested and non-forested regions. The thresholds for Coherence and Backscatter are  $t_1$  and  $t_2$  respectively.

at 100 and backscatter to identify the forested regions. The criteria used for setting the threshold are discussed here.

**Complex Coherence Coefficient:** The forest region can be modeled by randomly oriented dipoles and hence volume scattering component is strong (Freeman and Durden, 1998). The complex coherence coefficient for forested regions is naturally low because of random nature of scattering mechanisms. The increase in vegetation height also leads to lower coherence as a consequence of volume decorrelation (Cloude and Papathanassiou, 2003). This can be used as a major differentiator for forested and non-forested regions. However, the water regions of the River Ganga and other flowing tributaries and canals also have a very low coherence comparable

to that obtained in the forests. However, the urban regions, agricultural fields and dry riverbeds have higher coherence and can be delineated from forested and water regions.

Complex coherence values are obtained for all possible polarization combinations in any one basis. Here Pauli basis is utilized with coherence values obtained as  $\gamma_{HH+VV}$ ,  $\gamma_{HH-VV}$  and  $\gamma_{HV}$  considering reflection symmetry. Span coherence image is generated which combines the coherence in all polarizations and can be given as:

$$\gamma_{span} = \gamma_{HH+VV} + \gamma_{HH-VV} + 2\gamma_{HV} \quad 4.18$$

Samples are collected for different regions and thresholds calculated. For the present data, the coherence threshold  $t_1$  is set at 0.8. From samples collected for different land use classes, it was observed that the coherence for water (river and canal) regions was the lowest ranging between 0.1 and 0.6, while for forested regions the span coherence values range from 0.2 to 0.8. This is depicted in Figure 4.3. The range of span coherence value for dry land areas (dry riverbed, agricultural and barren fields and urban regions) was the highest of the three ranging between 1.0 and 2.4, signifying very low decorrelation. The pixels whose span coherence lies below 0.8 represent the forested and water regions while those which lie above 0.8 represent the dry riverbeds, urban regions and agricultural areas. Further refinement can be obtained by setting the threshold value  $t_2$  of the backscatter coefficient to identify the forested lands from the water regions.

**Radar Backscatter Intensity:** The radar backscatter intensity is the amount of radar wave reflected back to the sensor. For smooth surfaces, specular reflection occurs and the radar signal is reflected away from the sensor. In such cases the backscatter intensity is very low. This typically occurs for calm water regions. For urban areas, dry riverbeds and dry agricultural lands the backscatter intensity is high. This is due to surface roughness and presence of dihedral corner reflecting surfaces which leads to double-bounce scattering. The double-bounce scattering is particularly prominent in urban areas as the road and building walls act as corner reflectors. Forested regions have intermediate tone of backscatter between urban and water regions. The forested regions have multiple scattering centers that collectively contributes to backscattered intensity (Richards, 2009) and the interactions of radar waves is mainly between the leaves, twigs and branches. Due to extinction of radar waves while travelling between the sensor and back, and its scattering in the vegetated medium, the backscattered energy reflected back to the target is lower than for urban and agricultural regions.

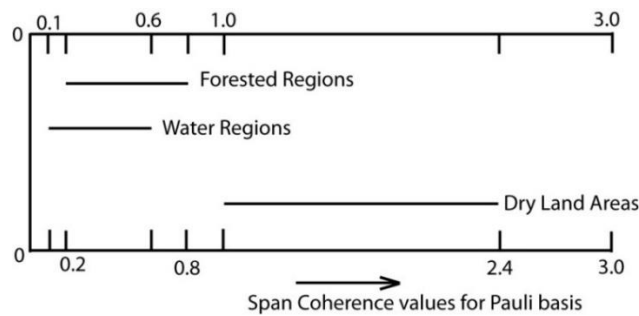


Figure 4.3 Span coherence values for different land cover regions. The value for forested regions  $\in(0.2,0.8)$ , water regions  $\in(0.1,0.6)$  and dry land areas  $\in(1.0,2.4)$

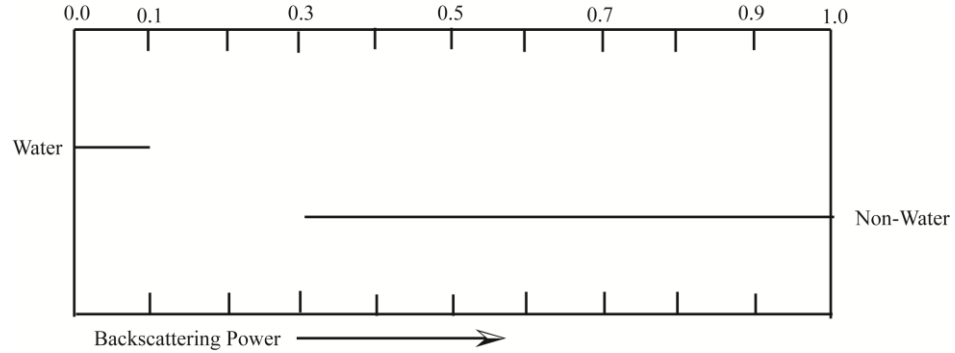


Figure 4.4 Threshold for backscattering power. The water and non-water regions result in distinctly different backscattering values. For water regions the backscattering power lies between (0, 0.1). For non-water, i.e. Forest and Urban areas, the backscatter power is more than 0.3.

This backscattered intensity is provided as an input for further refinement of the technique for differentiation between forested and water regions. After applying the coherence threshold  $t_1$ , the technique delineates the dry land areas but fails to identify the forested regions from the water regions. Hence another threshold  $t_2$ , using radar backscatter is applied for further refinement of the model. The radar backscatter intensity is obtained from the multi-looked SAR image and here the backscatter intensity from the  $T_{11}$  component of the coherence matrix is utilized. The reason for selection of  $T_{11}$  is that it is dominated by surface scattering.

$$T_{11} = \frac{1}{2} \langle |S_{HH} + S_{VV}|^2 \rangle \quad (4.18)$$

Supervised thresholds are calculated for different regions from samples provided. The range of backscattering power lies between (0, 1). It was observed that the backscatter intensity for water (river and canal) regions was between 0 and 0.1. While for other regions, the backscatter intensity is  $>0.3$  as depicted in Figure 4.4. Hence the threshold applied is  $T_{11} = 0.1$ . This input leads to identification of forested, water and dry land areas. Now the 'Three Stage Inversion' technique is applied for vegetated regions and results presented in the next chapter.

## 5. RESULTS AND DISCUSSION

The methodologies described above are applied on the acquired SAR data sets. The obtained results and their analysis is presented in this chapter.

### 5.1. Effect of shift in POA on multi-frequency SAR data

Fully polarimetric SAR data was acquired over Manali, Himachal Pradesh, India in three frequency bands - L, C and X. The data was acquired in Single Look Complex (SLC) format. Figure A4.1 in Appendix IV provides color coded Pauli decomposed SAR images acquired by the three SAR platforms. Multi-look processing is carried out to generate square pixels for better visual interpretation. The resolution of SAR data improves with increasing frequency of operation. Figure 5.1 shows the Google Earth Imagery of Manali and its surroundings. The study area is divided into three major regions for analysis. The major land cover classes are - (a) Vegetated/Forested regions comprising mainly of the park regions of Van Vihar, a Deodar (*Cedrus deodara*) species dominated park area near Manali; (b) The urban region of Manali city and (c) River area of Beas river.

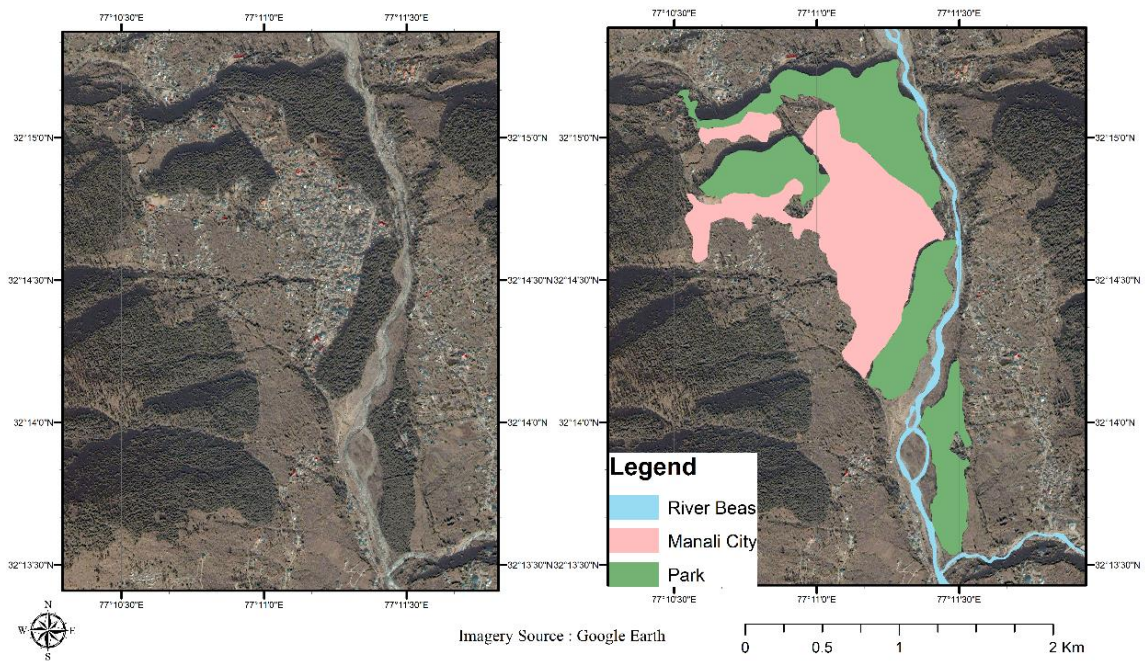


Figure 5.1 Left: Google Earth Imagery of Manali, Himachal Pradesh. Right: Three major areas of interest – Urban city region, Parks and the River Beas.

### 5.1.1 Polarization Orientation Angle (POA) Shift

Using the Circular Polarization technique (Equation 2.33-2.34) the POA of the SAR wave is calculated. The histograms for the estimated POA are presented in Figure 5.2. The distribution of the POA is normal for ALOS PALSAR with a skewness coefficient of 0.045.

Fig. 5.2a. ALOS PALSAR (L-Band)

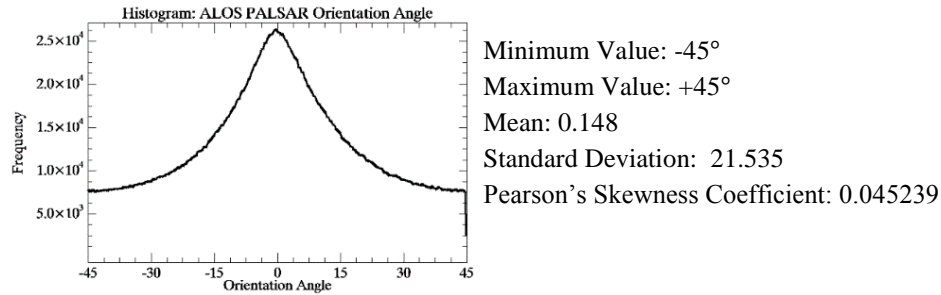


Fig. 5.2b. RADARSAT-2 (C-Band)

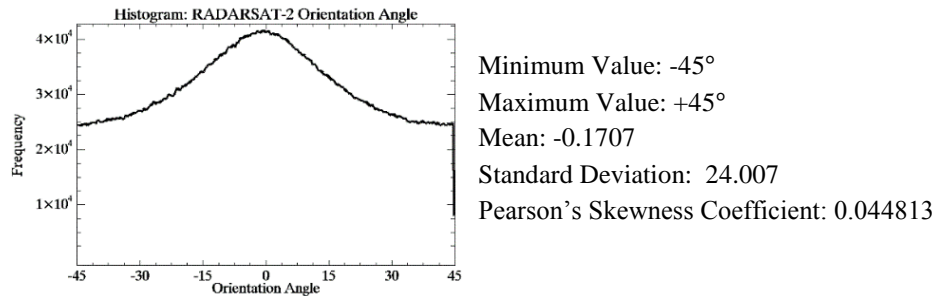


Fig. 5.2c. TERRASAR-X (X-Band)

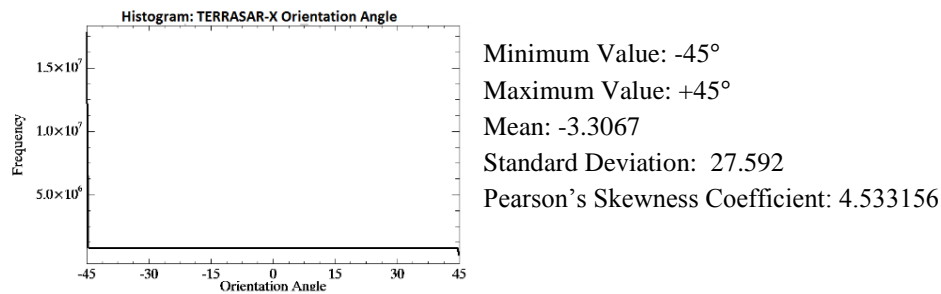


Figure 5.2 Histograms and Statistics of the POA induced in multi-frequency data sets.

There is very low POA for most of the pixels. While for RADARSAT-2, as the frequency increases, the induced POA also increases. However the distribution of the POA remains Gaussian with a skewness coefficient of 0.044. The bell shaped curve in case of L- and C-band show that the Circular Polarization technique is a good estimator. Whereas for X-band the histogram in Figure 5.2c leads to a possible explanations – that the X-band data contains high signal-to-noise (SNR) ratio.

### 5.1.2 Yamaguchi Decomposition

The obtained coherence matrix is decomposed using the Yamaguchi four component decomposition to obtain the scattering powers of the four scattering mechanisms viz. double-bounce scattering, surface scattering, volume scattering and helix scattering. As different scattering mechanisms are dominant in different regions of the study area, the effect of shift in POA can be studied from the effects observed in the scattering powers of the Yamaguchi decomposed products.

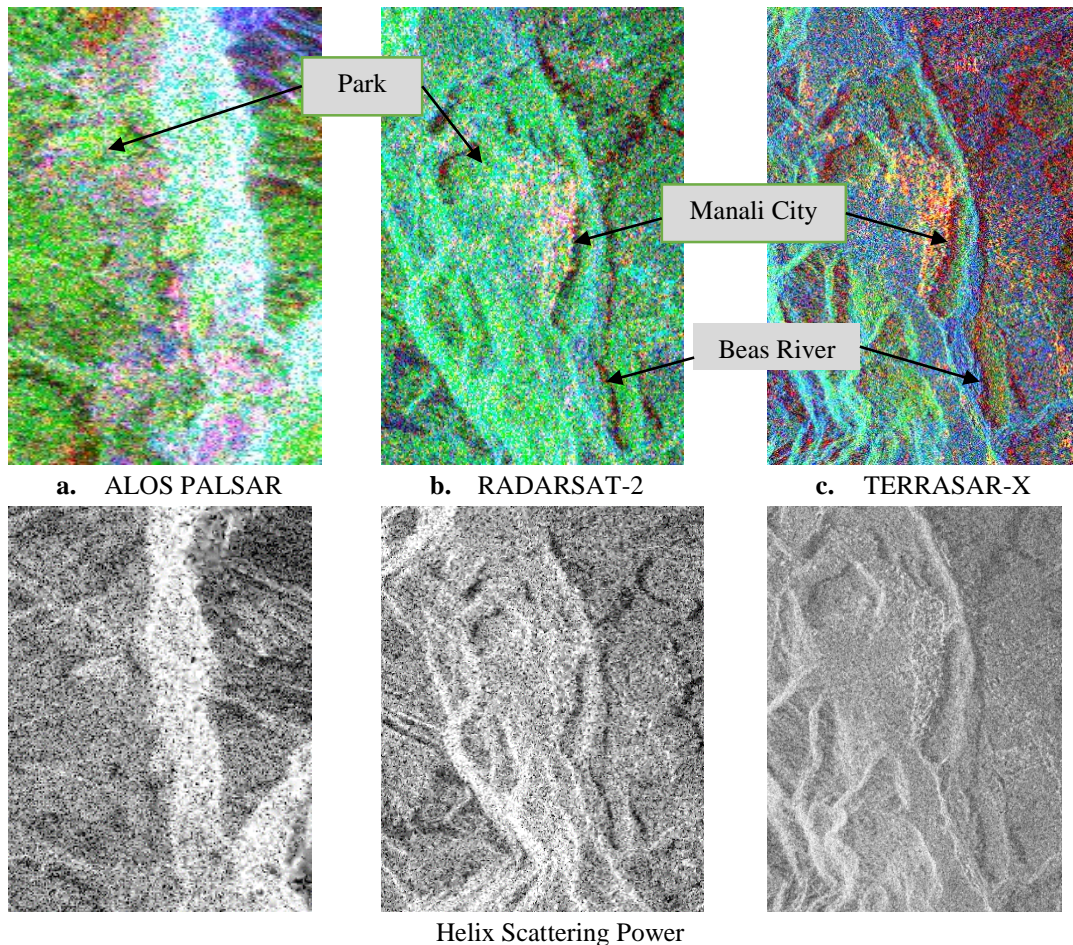


Figure 5.3 Yamaguchi decomposed color coded images for three SAR sensors before orientation angle compensation.

Figure 5.3 provides the color coded Yamaguchi decomposed images for the three SAR frequency bands. The color coding used is red for double-bounce scattering, blue for surface scattering and green for volume scattering. The park regions and urban features are easily distinguishable in all three acquisitions, River Beas is distinguished from nearby features in C- and X-band images. For L-band acquisition the river region presents almost equal scattering power which may be due to mixed response from multiple scatterers, as the spatial resolution of L-band data set is about 23.5 meters. Beas River has rapids near Manali city. Due to this, there is presence of double-bounce scattering from rock surfaces. At C-band the surface scattering from the water surface and

volume scattering from multiple reflections from rock surfaces can be observed. The X-band TERRASAR-X data presents a very clear scattering media distinction, with river surface as surface scatterer, the urban region as double-bounce scatterer and the park region as volume scatterer. With TERRASAR-X data, the spatial resolution improves to 3 meters. This leads to individual scattering media distinction more effectively than at L- or C-band.

### **5.1.3 Effect of Shift in POA on Yamaguchi decomposed products**

The coherence matrices are decomposed into the constituent scattering mechanisms using Yamaguchi decomposition. After POA compensation, the rotated coherence matrix is also decomposed for comparative study. Figure 5.4 shows the decomposed products pre- and post-POA compensation. POA shift compensation can also be termed as deorientation. The effect of POA shift is observed on the Yamaguchi decomposed products. The qualitative effects observed are that the volume scattering power decreases and the double-bounce scattering power increases after POA compensation. A quantitative analysis is required for understanding the effect in tangible terms. This is carried out as follows.

The study area is divided into three regions as described earlier – urban region, park region and the water region. These regions are representative of scattering media dominated by double-bounce scattering, volume scattering and surface scattering respectively. 50 random samples are collected in the three regions and the scattering powers are compared pre- and post-deorientation. The scattering powers are measured in decibel (dB) scale. The change in the four scattering components is measured and presented in the next sub-sections.

#### **5.1.3.1 Effect on Double-bounce Scattering Power**

Double-bounce or dihedral scatterers are generally dominant in urban centers and in this particular study, the river with rapids and rocks also acts as a dihedral scatterer. In Yamaguchi decomposition, double-bounce scattering power is given by (Sec. 2.4):

$$f_d = \frac{1}{2} \langle |S_{HH} - S_{VV}|^2 \rangle - 2 \langle |S_{HV}|^2 \rangle \quad (5.1)$$

The double-bounce scattering power shows change after compensating for POA shift. The Figure 5.5 depicts the trend-line for the change in scattering power across all the three regions. Overall, it was observed that the double-bounce scattering power increases after compensation. Very low (-30dB) scattering power is observed in park region for X-band SAR data. X-band signal, owing to smaller wavelength, cannot penetrate the canopy of the thick trees in park region.. ALOS PALSAR has a spatial resolution of 23.5 m. Hence one resolution cell on ground contains various types of scattering media. The backscattered power is a function of the cumulative behavior of the different types of scatterers. This can be the reason behind similar double-bounce backscatter behavior depicted by the L-band data in the three classes.

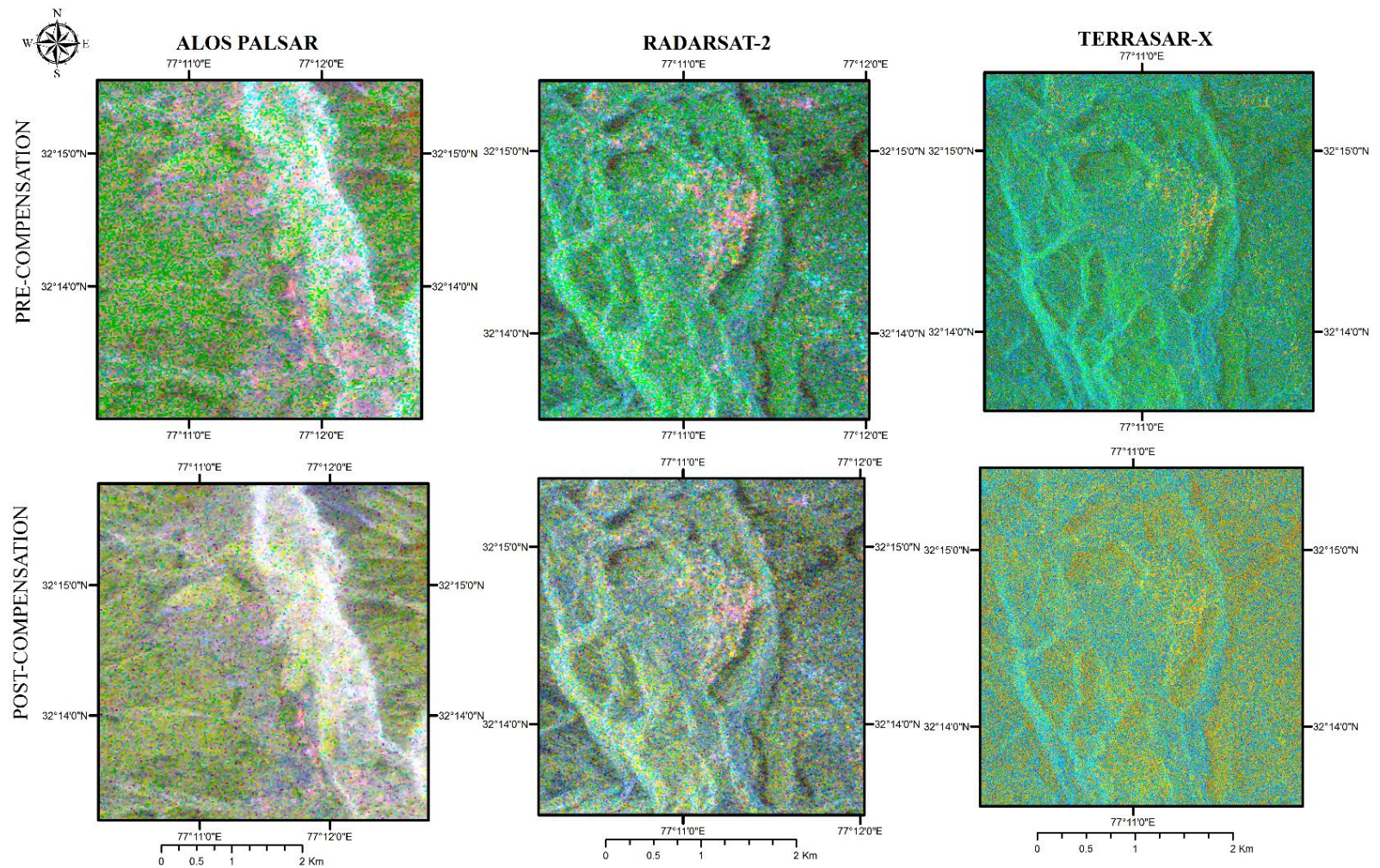


Figure 5.4 Comparison of Yamaguchi decomposed products Pre- and Post-orientation angle compensation. Color coding used- Double-bounce scattering– red; Volume scattering– green; Surface scattering – blue.

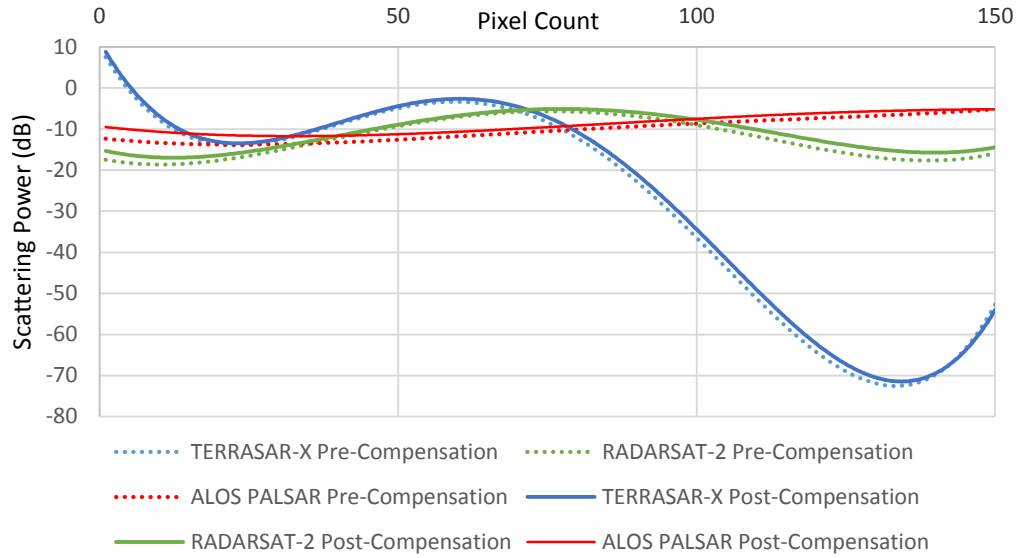


Figure 5.5 Effect of Orientation Angle Shift on double-bounce Scattering Power. Sample points 1-50 belong to River area; 51-100 to Urban region; 101-150 to Park region. As shown the double-bounce scattering consistently increases after de-orientation.

Table 5.1 quantitatively presents the change in double-bounce scattering power pre- and post-deorientation. It is observed, that the amount of change in double-bounce scattering power decreases with increasing frequency of operation of sensor. This shows that the effect of orientation angle shift decreases with increasing frequency of operation.

Table 5.1 Change in double-bounce scattering power post-POA compensation.

Sample Area	ALOS PALSAR	RADARSAT-2	TERRASAR -X
Water	2.16 dB	1.03 dB	0.77 dB
Urban	0.99 dB	0.54 dB	0.60 dB
Park	1.02 dB	1.94 dB	1.80 dB
Overall	4.18 dB	3.52 dB	3.18 dB

### 5.1.3.2 Effect on Surface Scattering Power

Surface scattering is dominant in barren fields, sand banks and calm river surface. The surface scattering power in terms of the elements of scattering matrix are given as (Sec. 2.4):

$$f_s = \frac{1}{2} \langle |S_{HH} + S_{VV}|^2 \rangle - 4 \langle |S_{HV}|^2 \rangle + 2 |Im \langle S_{HV}^* (S_{HH} - S_{VV}) \rangle| \quad (5.2)$$

The surface scattering power increases overall as observed in Figure 5.6 and Table 5.2. However the trend is different for water, urban and park regions. The overall increase does not show any particular trend with respect to the operating frequency of the SAR system. L-band data shows minimal increase in scattering power post-compensation in all regions. C-band data shows relatively high increase in scattering power for river and park regions, however, a slight increase

was measured for urban centers. X-band data depicted different result – an increased scattering power observed in river and urban areas while a decrease is observed for park regions.

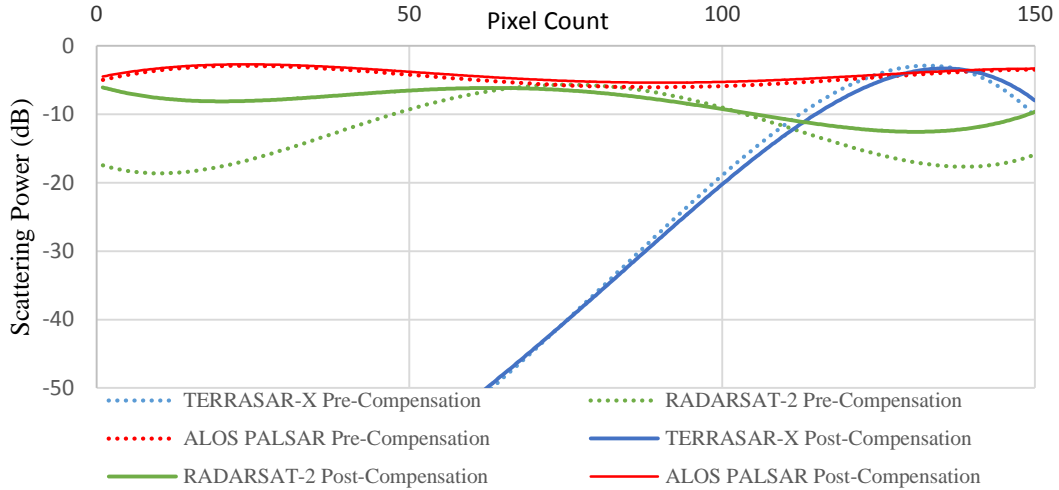


Figure 5.6 Effect of Orientation Angle Shift on Surface Scattering Power. Sample points 1-50 belong to River area; 51-100 to Urban region; 101-150 to Park region. Scattering power below -50dB is considered as noise and ignored.

TERRASAR-X SAR signal cannot penetrate the canopy and interacts with the canopy itself, the interaction being governed by the leaf and branch interactions. This leads to higher surface scattering as compared to double-bounce (Figure 5.5) and volume scattering (Figure 5.7). This may result in the high surface scattering power for X-band data.

Table 5.2 Change in surface scattering power post-POA compensation..

Sample Area	ALOS PALSAR	RADARSAT-2	TERRASAR -X
Water	0.29 dB	7.64 dB	0.93 dB
Urban	0.65 dB	-0.73 dB	0.57 dB
Park	0.30 dB	4.33 dB	-1.15 dB
Overall	1.25 dB	11.24 dB	0.35 dB

### 5.1.3.3 Effect on Volume Scattering Power

The park region is the dominant volume scatterer in the study area. The volume scattering power is given by (Sec. 2.4):

$$f_v = 8\langle |S_{HV}|^2 \rangle - 4|Im\langle S_{HV}^*(S_{HH} - S_{VV}) \rangle| = 4T_{33} - 2|Im(T_{23})| \quad (5.3)$$

Figure 5.7 shows the trend in the volume scattering power pre- and post-deorientation. It is observed that the volume scattering power decreases post-deorientation. The decrease is very high for X-band data (Table 5.3) as compared to L- and C-band data sets. For L-band, due to poor resolution and presence of rapids and rocky outcrops in the river region, the volume scattering is dominant before compensation. For river region, the overestimation in volume scattering power results in higher decrease in volume scattering power post-deorientation. The decrease in volume

scattering power shows that the orientation angle shift leads to over-estimation of volume scattering. As expected, the volume scattering decreases more in park region as compared to any other region for C- and X-band.

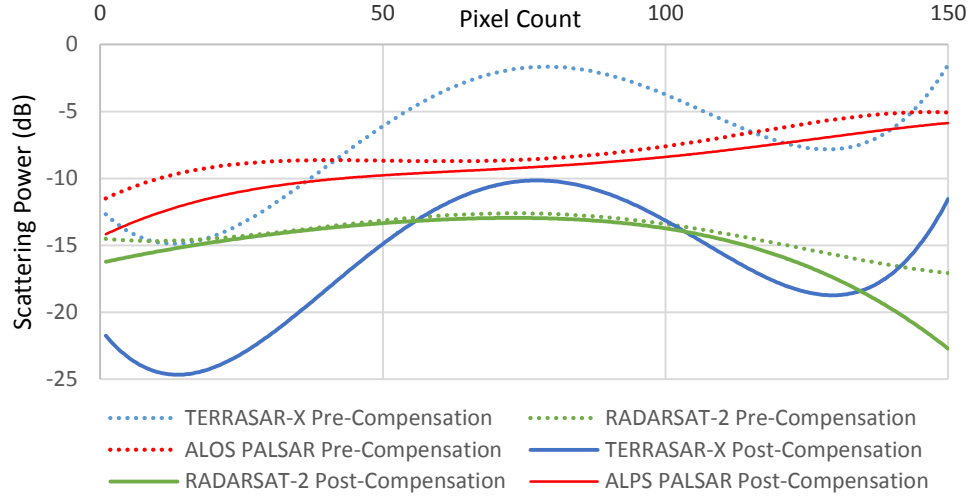


Figure 5.7 Effect of Orientation Angle Shift on Volume Scattering Power. Sample points 1-50 belong to River area; 51-100 to Urban region; 101-150 to Park region. The volume scattering power shows appreciable decrease post-compensation.

Table 5.3 Change in volume scattering power post-POA compensation.

Sample Area	ALOS PALSAR	RADARSAT-2	TERRASAR -X
Water	-1.87 dB	-0.70 dB	-9.82 dB
Urban	-0.66 dB	0.15 dB	-8.71 dB
Park	-1.27 dB	-2.06 dB	-10.04 dB
Overall	-3.81 dB	-2.62 dB	-28.58 dB

It is observed that the amount of increase in double-bounce scattering power is not equal to the amount of decrease in volume scattering power. (Lee and Ainsworth, 2011) state that “the amount of decrease in volume power is generally greater than the increase in double-bounce power.” This was observed to be true only in case of TERRASAR-X data where the increase in double-bounce power is 3.18 dB while the decrease in volume scattering power is -28.58 dB. However the results are to the contrary for L- and C-band data. The amount of decrease in volume scattering power is lower than the increase in double-bounce scattering power as seen in Table 5.3.

### 5.1.3.4 Effect on Helix Scattering Power

The result presented below are an important observations of the present study. The helix scattering is observed in complex structures in urban regions. The helix scattering power is given by:

$$f_c = 2|Im\langle S_{HV}^*(S_{HH} - S_{VV}) \rangle| = 2|Im(T_{23})| \quad (5.4)$$

After POA shift compensation, the deoriented helix scattering power  $\bar{f}_c$  is given by

$$\bar{f}_c = Im(-F^* \sin^2 2\theta + F \cos^2 2\theta)$$

$$= \text{Im}(F \sin^2 2\theta + F \cos^2 2\theta) = f_c$$

This shows that the helix scattering power  $f_c$  should be roll invariant (Lee and Ainsworth, 2011) and hence should not be affected by shift in POA. However the results obtained in the present study state otherwise. The results obtained are contradictory to the literature available. It is observed in Figure 5.8 that the helix scattering power decreases after compensation for POA shift. Helix scattering values in X-band were below -100 dB and are considered noise. For L- and C-band data, the helix scattering power decreases in all the three regions. The decrease in scattering power is highest for river areas and least for urban regions. This effect suggests overestimation of helix scattering power, much in the same manner as for volume scattering. Helix scattering is generally resultant from complex geometrical scatterers. The Beas River has many rapids, boulders and stones in the path. This may have resulted in helix scattering power to be overestimated before deorientation. However, the reason for change in helix scattering power needs to be mathematically explained using a physics based approach. This is beyond the scope of the present work.

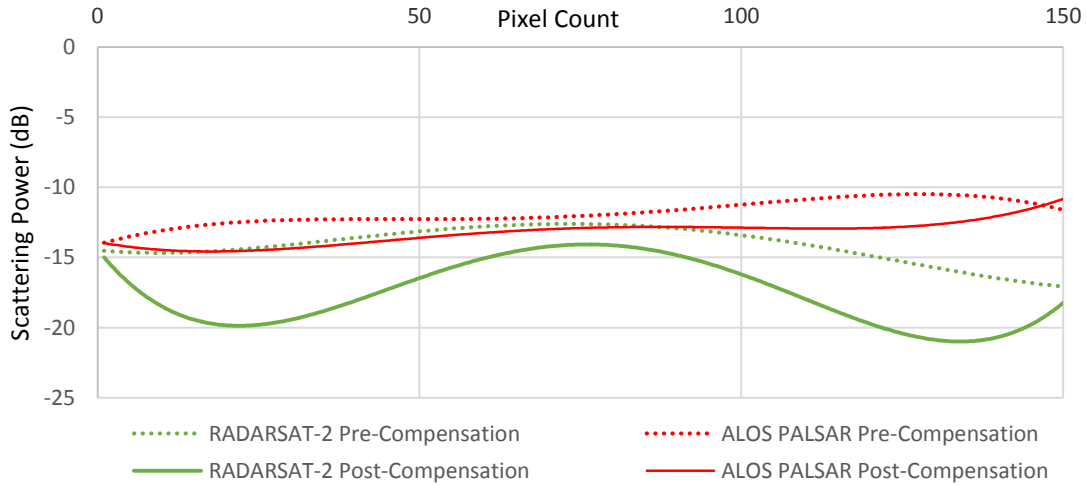


Figure 5.8 Effect of Orientation Angle Shift on Helix Scattering Power. Sample points 1-50 belong to River area; 51-100 to Urban region; 101-150 to Park region. The helix scattering power shows appreciable decrease post-compensation. The scattering power for TERRASAR-X is below -100dB and considered noise and ignored for analysis.

Table 5.4 Change in helix scattering power post-POA compensation.

Sample Area	ALOS PALSAR	RADARSAT-2	TERRASAR -X*
Water	-1.76 dB	-4.08 dB	-
Urban	-0.84 dB	-2.39 dB	-
Park	-1.76 dB	-3.88 dB	-
Overall	-4.36 dB	-10.36 dB	-

\* - Backscatter values for Helix scattering, in case of TERRASAR-X were below -100dB. Hence ignored.

A small study has been carried out to study the effects of shift in POA on PolInSAR data and its products. The results of the study are presented in Appendix III.

## 5.2. Polarimetric Interferometric Synthetic Aperture Radar (PolInSAR)

PolInSAR acquisitions were carried out on 3<sup>rd</sup> and 28<sup>th</sup> March 2013. The data obtained in Single Look Complex (SLC) format was processed to determine the backscatter coefficients of the Scattering matrices  $[S_1]$  and  $[S_2]$  for the two acquisitions at the ends of the baseline. The Figure 5.9 provides the Pauli basis images for the two acquisitions.

### 5.2.1 Co-registration of Scattering Matrices

The two repeat pass, fully polarimetric acquisitions which form the PolInSAR data pair are co-registered to each other. Using the first acquisition as the reference or master image, the second acquisition is co-registered using spectral analysis. The shift in the rows and columns is estimated using this technique and presented in Table 5.5. Initially, a window of 1024 x 256 (rows x columns) is selected for coarse co-registration and later a finer co-registration is carried out.

Table 5.5 Co-registration: Shift in rows and columns

	Rows	Columns
Shift	-88	-1

The co-registered slave image has a shift of 88 rows and 1 column. Hence after co-registration, in the slave image, there is a perceptible shift in the rows from top as seen in Figure 5.10. All further outputs would have this shift in rows at the top as a result of co-registration. It is estimated (Krieger *et al.*, 2005) that the decorrelation due to co-registration error is around 0.97, which may lead to small bias in forest stand height estimation.

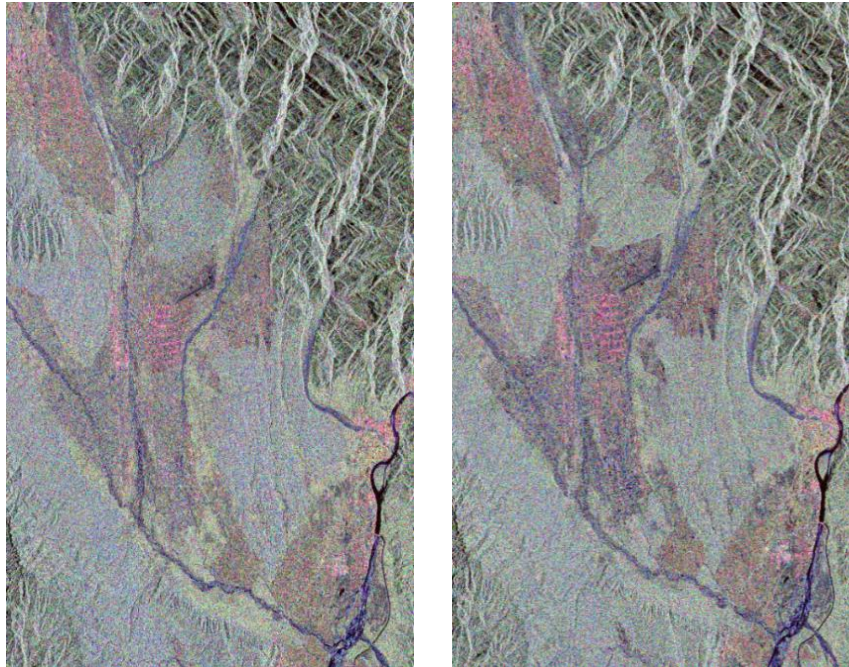


Figure 5.9 Pauli basis images of two acquisitions.

### 5.2.2 Estimation of Baseline

The baseline between the two acquisitions is calculated and the results are presented in Table 5.6.

Table 5.6 Baseline Estimation

Parameter	Value
Normal Baseline	78.67 meters
Critical Baseline	3857.53 meters
Time Baseline	24 Days
$2\pi$ ambiguity height	226.128 meters
$2\pi$ ambiguity displacement	0.028 meters

The baseline of the acquisition is 78.67 meters. The baseline is directly related to the volume decorrelation (Krieger *et al.*, 2005), with lower baseline acquisitions resulting in lower volume decorrelation. Baseline of 78.67 meters should result in very low volume decorrelation effects.

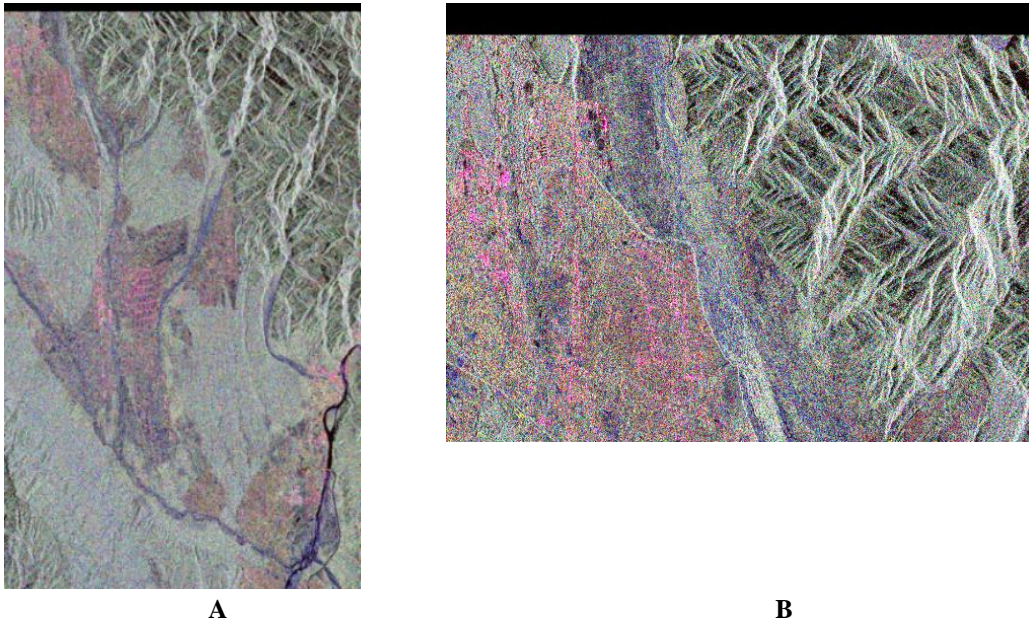


Figure 5.10 Shift in rows after co-registration. A) The co-registered slave image. The black rows at the top are the rows which are shifted after co-registration with the master image. B) A zoomed portion of the top left corner can be viewed showing the 88 rows shift leading to black portion at the top.

This can result in accurate parameter estimation. The time baseline of 24 days is the minimum temporal baseline possible with RADARSAT-2 data as this is the repeat pass temporal gap required. Thus the temporal de-correlation is kept minimum. The  $2\pi$  ambiguity height has an important consequence. The ‘Three Stage Inversion’ technique for tree height estimation can accurately predict height which is less than half of the  $2\pi$  ambiguity height. As the value here is 226 meters, hence the technique can accurately predict heights up to 123 meters. This is sufficient as the forest stand height for Sal forest does not exceed 35 meters in the study area.

### 5.2.3 Generation of Vertical Wavenumber $k_z$

The vertical wavenumber  $k_z$  depends on the imaging geometry and radar wavelength, given by

$$k_z = \frac{4\pi\Delta\theta}{\lambda\sin\theta} \quad (5.5)$$

The meaning of terms are explained in Sec. 4.2. The calculated  $k_z$  value lies between so 0.2217 and 0.2395. Higher values of  $k_z$  lead to lower height bias due to temporal decorrelation (Krieger *et al.*, 2005). For a vertical wavenumber of around 0.2 the temporal decorrelation effect on the estimated forest stand height is in the range of 0m - 4m with the maximum height bias of 4m for a high temporal decorrelation of 0.5 (Krieger *et al.*, 2005). As the temporal baseline for the present acquisition is 24 days and the Sal dominated forest is mature with very low change during the acquisitions, the temporal decorrelation would be very low. However without detailed knowledge of the changing processes during the acquisition, it is very difficult to measure temporal decorrelation. For the present study, it is considered that the effects of temporal decorrelation are negligible. Combined with lower temporal baseline and relatively high interferometric wavenumber ( $>0.2$ ), the bias in height due to temporal decorrelation can be ignored.

### 5.2.4 Multi-looking and Generation of $T_6$ Matrix

The 6x6 complex coherence matrix  $[T_6]$  is the main observable in PolInSAR data. As explained in Section 2.7 (Eq. 2.37), the  $[T_6]$  matrix contains the polarimetric and interferometric information from the two acquisitions. The Scattering matrices  $[S_1]$  and  $[S_2]$  are vectorized to obtain the scattering vectors (Eq. 4.8)  $k_1$  and  $k_2$ . Scattering matrix is multi-looked to equate the ground-range resolution and azimuth resolution, obtaining square pixels. As explained in Eq. 4.11, the elements of the  $[T_6]$  matrix are calculated and the Pauli basis images for the  $[T_{11}]$  and  $[T_{22}]$  matrices are generated and presented in Figure 5.11. The Barkot forest is prominent in the center of the image with River Ganga flowing to the east, seen as a dark region. The scattering from the river surface is dominated by surface scattering. But very calm water surfaces act as specular scattering surface, and most of the SAR wave is reflected away from the receiver. Due to this, the backscattered energy is very low leading to dark pixel value for the river surface. The city of Rishikesh is between the River Ganga and the Barkot forest. It is distinguished by the dominant double bounce scattering represented by red color. The Thano forest range is to the north-west of Barkot forest. Forests are dominated by volume scattering. However, on closer analysis, double-bounce scattering is also present along with surface scattering. The volume scattering from canopy, double-bounce scattering from tree-trunk and ground interactions, and surface scattering from the ground are present in forest regions. The RVoG model as depicted in Fig. 2.3 can be applied to these forest regions.

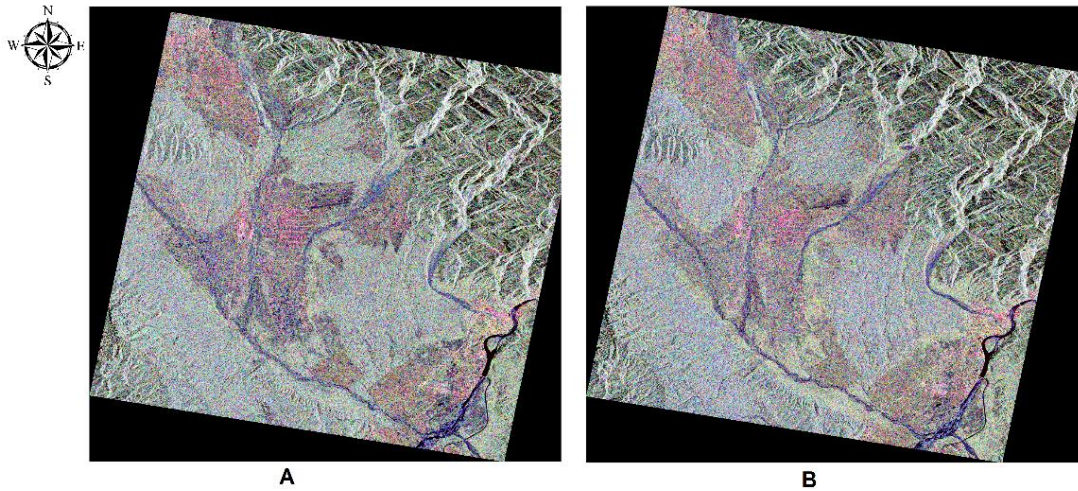


Figure 5.11 Pauli basis images after multi-looking and generation of  $[T_6]$  matrix. The images for two acquisitions A and B are presented above.

### 5.2.5 Calculation of Complex Coherence in different Polarization Basis

The complex coherences were estimated from the  $6 \times 6$   $[T_6]$  coherence matrix. The complex coherence is a function of polarization basis  $(\omega_1, \omega_2)$  given in Eq. 2.40. Figure 5.12 shows the three complex coherences obtained from the different linear combinations of the elements of the coherence matrix in the H, V-polarization basis. The Barkot forest range forms the top-left region of the image. A dry river channel can be seen to the north of the forest while the Rishikesh City and River Ganga are to the east of the Barkot forest.

The scaling from white to black corresponds to the coherence values from one to zero. For HH-  $(\omega_1 = \omega_2 = [1/\sqrt{2} \ -1/\sqrt{2} \ 0]^T)$  and VV-map  $(\omega_1 = \omega_2 = [1/\sqrt{2} \ 1/\sqrt{2} \ 0]^T)$  the significant coherence is observed in the dry river channel and urban areas. However, there is very low coherence in the river. As explained by (Cloude and Papathanassiou, 1998), temporal decorrelation leads to low coherence value independent of the polarization channel. Very low coherence is observed for the river in all three polarizations mainly due to temporal decorrelation.

The urban area have high coherence in HH- and VV-polarizations due to low volume and temporal decorrelation. However for forest regions, the coherence is very low in all the three polarizations. For HV-map  $(\omega_1 = \omega_2 = [0 \ 0 \ 1]^T)$  the coherence for urban centers is lower than observed in HH and VV polarizations. The urban areas are dominated by smooth and dihedral surfaces leading to high surface and double-bounce scattering. This leads to high HH- and VV- coherence but lower HV-coherence. The three coherence maps can be quantitatively seen from the corresponding coherence histogram as shown in Figure 5.13.

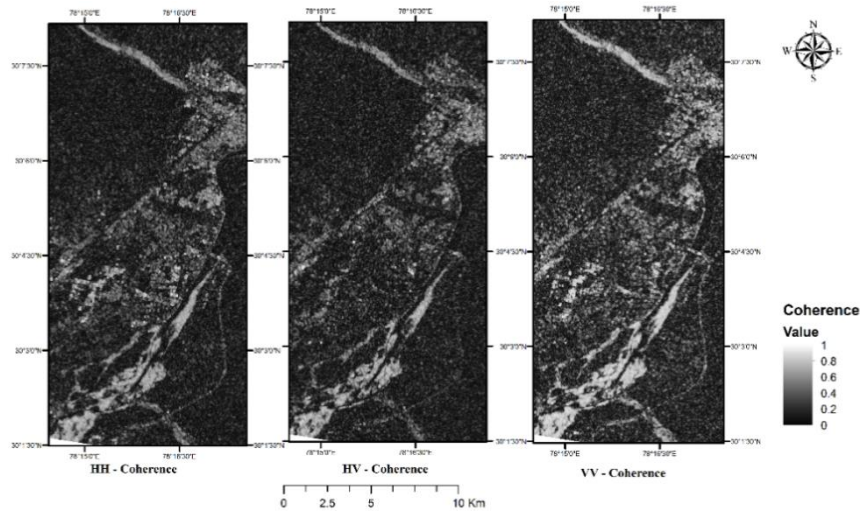


Figure 5.12 Coherence maps in H, V-polarization basis.

A color composite map for the coherence in Linear basis is shown in Figure 5.14. The coherence can be better visualized using the color composite map. The HH-coherence is represented by red color, HV-coherence by green color and VV-coherence by blue color. A zoomed portion of Rishikesh city and surrounding areas is shown on the left side of the image. The Barkot forest, Rishikesh city, dry river channel and the Ganga River can be seen in the map. The urban centers are dominated by HH-coherence in places where the color is red or pink. Some urban areas, especially in the Rishikesh City, are also showing high cross-polarized coherence.

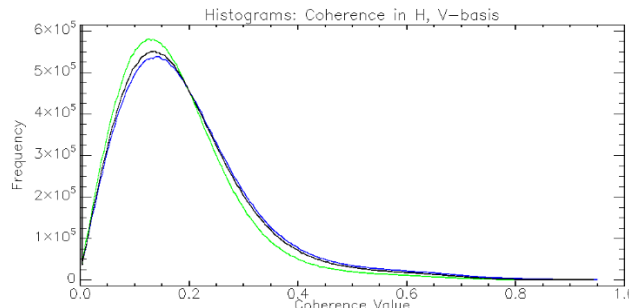


Figure 5.13 Coherence histograms in H, V-polarization basis. Blue – HH; Green – HV; Black – VV.

This may be due to one of the two reasons-dense structures or orientation angle shift. Close-clustering of urban structures leads to multiple scattering and increased cross-polarized (HV) coherence. This can be interpreted as volume scattering. Other reason for dominance of cross-polarization can be due to shift in POA shift. The features and conditions which induce the shift are enumerated in Sec. 2.6.

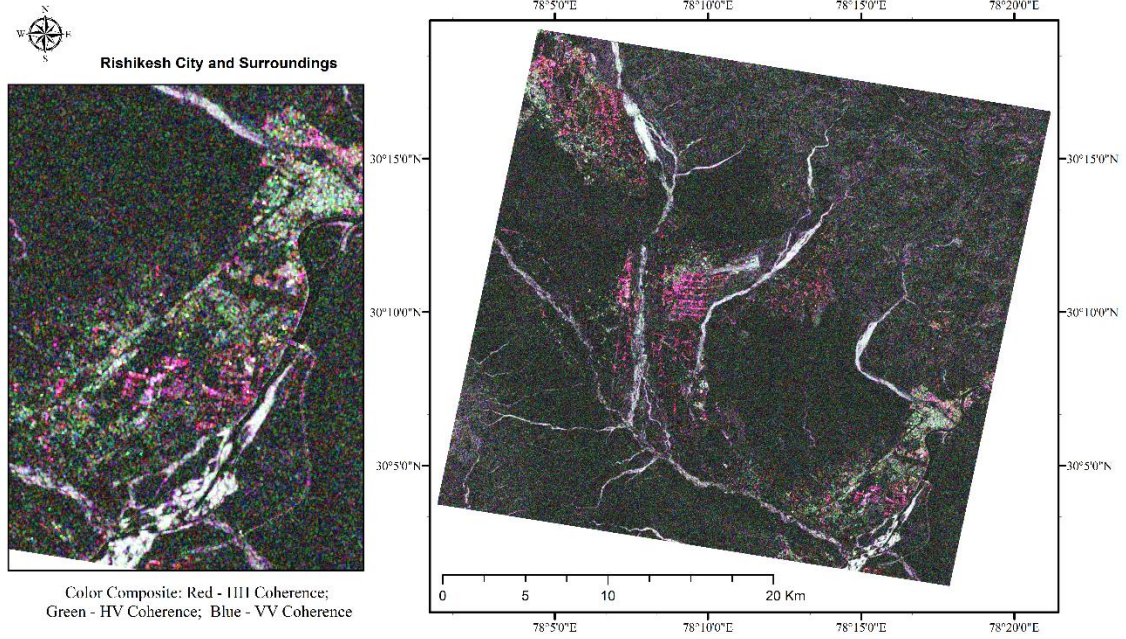


Figure 5.14 Color composite coherence map in H, V-polarization. Red – HH; Green – HV; Blue – VV.

In the zoomed portion depicting the Rishikesh City and surroundings, the urban portion in the center and at the top-right corner of the map, show high HH-coherence whereas the city area has high HV-coherence. While the urban centers in the central portion of the zoomed image are sparse built-up areas interspersed with farm lands (having very low coherence seen as black portion), the urban region to the north are dense urban clusters. Hence the sparse built-up areas show dominant HH-coherence and the dense urban centers show HV-coherence. However the urban area on the extreme top-right corner, in-spite of dense clusters, exhibit high HH-coherence contrary to the areas to its immediate south. This can be attributed to orientation angle shift. The Barkot and Thano forest ranges are exhibiting very low coherence in all three polarizations leading to darker shades. Whereas the dry riverbed are shown as very bright regions. This is due to very high coherence in all three polarizations and very low temporal decorrelation. The Figure 5.14, thus depicts the scattering behavior of different regions in the study area.

Polarization basis transformation and its implementation has been explained in Sec. 2.5. To demonstrate the basis transformations, the coherence maps for polarization in different basis are shown below. Coherences are calculated in Pauli basis (HH+VV, HV+VH, HH-VV), Circular basis (LL, LR, RR) and Optimal basis (Opt-1, Opt-2, Opt-3). The notations in the brackets are the polarization combinations associated with each polarization basis.

Pauli basis polarization uses addition and subtraction of linear polarized waves. HH+VV, HH-VV and HV+VH are the three polarization under the Pauli basis. As reflection symmetry is considered in the current work (HV=VH), HV+VH can be replaced by 2HV. However to avoid confusion, HV+VH is used to define cross-polarizations in Pauli basis. Figure 5.15 shows the

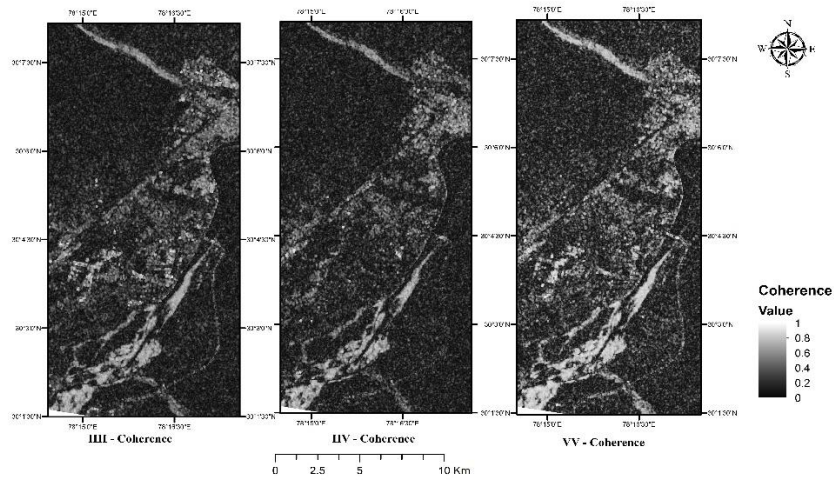


Figure 5.15 Coherence maps in Pauli-polarization basis.

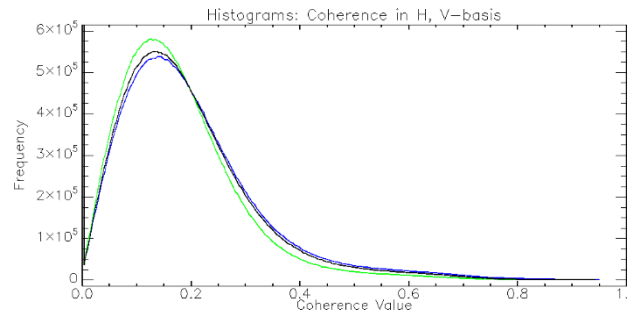


Figure 5.16 Coherence histograms in Pauli-polarization basis. Blue – HH+VV; Green – HV+VH; Black – HH-VV.

coherence maps in Pauli basis while the differences in the different basis can be quantitatively viewed in the histograms in Figure 5.16. The color composite image is presented in the Figure 5.17.

The difference between Linear basis and Pauli basis is difficult to identify using the individual coherence maps, hence color composite maps are shown in Figure 5.17. In Figure 5.17, it is observed that all the coherences lie between the value of (0.0, 0.4). This is similar to what is observed for linear polarizations in Fig. 5.13. However the color composite image provides a better medium for visual interpretation of the coherences. It is well known that the HH-VV polarization represents double-bounce scattering, HH+VV represents surface scattering and HV+VH volume scattering. As observed in Figure 5.17, the dry river channels are depicted by cyan color which can signify presence of stable surface and double-bounce scatterers. The stones in the dry riverbed result in double-bounce scattering and the ground results in surface scattering. The urban areas are dominated by greenish and reddish hues. These are indicative of presence of scatterers leading to volume and double-bounce scattering respectively. The reasons for urban areas showing two different scattering behavior are explained earlier. The forest regions, due to

volume decorrelation present lower coherences and hence appear dark regions on the coherence maps.

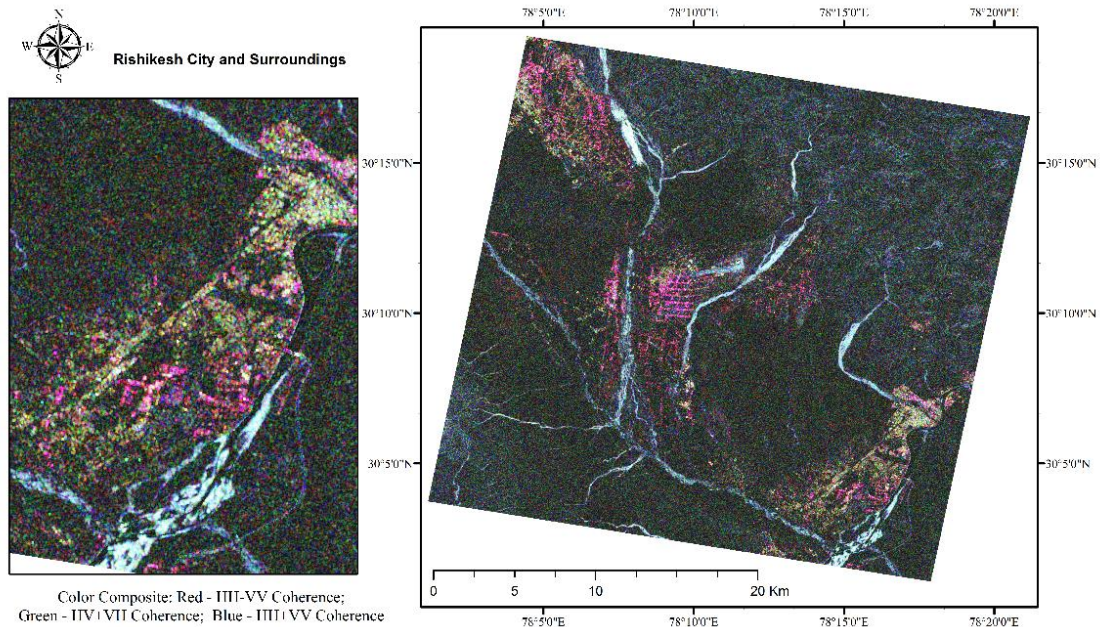


Figure 5.17 Color composite coherence map in Pauli-polarization basis. Red – HH+VV; Green – HV+VH; Blue – HH+VV.

Circular basis consists of LL, LR and RR polarizations. L stands for Left-Circular and R for Right-Circular. The first of the two letters in the polarization combination is for transmit and the second for receive. The coherence maps for the three polarizations under the circular polarization basis is shown in Figure 5.18, its histograms in Figure 5.19 and the color composite image in Figure 5.20. As observed in Figure 5.18, the cross polarized coherence is lower in urban regions as compared to the like polarizations. The histograms trace similar patterns for LL and RR polarizations.

The color composite coherence map is shown in Fig. 5.20. The forests present a very dark shade of green suggesting lower coherence overall but high dominance of cross-polarized LR coherence. The explanation for cross-polarized component being dominant is due to the presence of volume scattering. The dry riverbed also has significant LR coherence, while the urban centers are dominated by co-polarized LL and RR coherences. In dry riverbed, the LR coherence is dominant in Circular basis while HH+VV coherence is dominant in Pauli basis. It can be inferred that the interaction of SAR waves with scattering media is a function of the polarization of the incident wave. The cross-polarized LR scattering is dominant in Forest and vegetated areas, depicted with a darker tone, suggesting loss in coherence due to volume decorrelation.

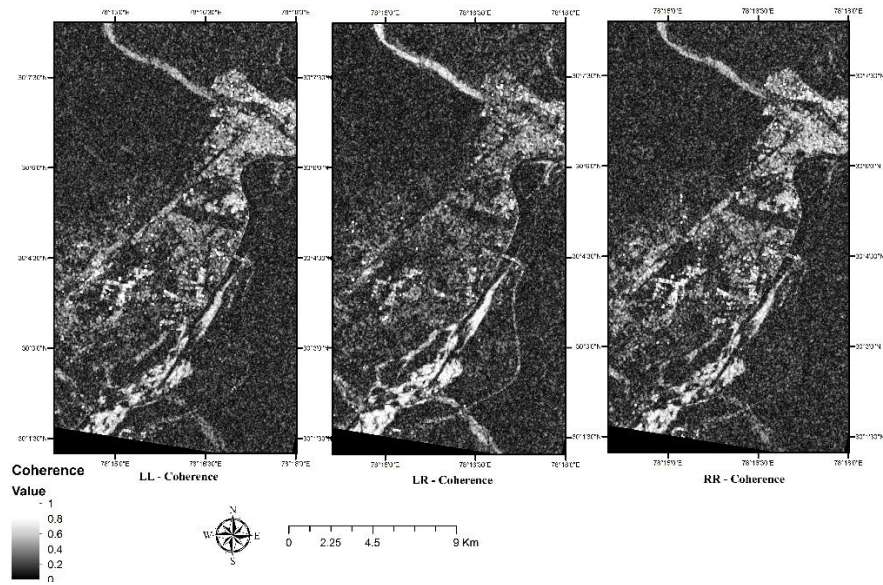


Figure 5.18 Coherence maps in Circular-polarization basis.

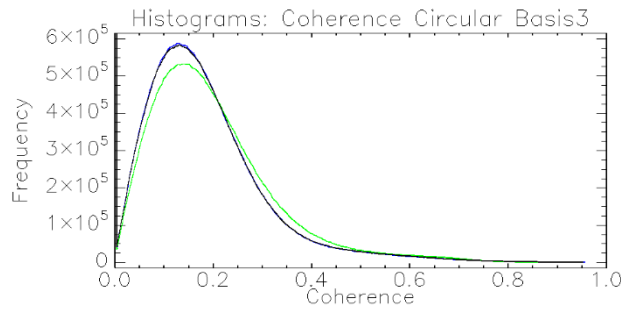


Figure 5.19 Coherence histograms in Circular-polarization basis. Blue – LL; Green – LR; Black – RR.

In the color coded images in Figure 5.14 Figure 5.17 and Figure 5.19 the forest regions are dominated by two scattering mechanisms whereas there is a presence of all three scattering mechanisms in urban regions. This can be attributed to the fact that C-band SAR waves penetrate less in the forest canopy and hence volume and double-bounce scattering is dominant. On the other hand the urban regions have dominant surface and double-bounce scattering. However due to high density of urban structures and orientation angle shifts, volume scattering is also observed in urban regions.

Using the coherence optimization technique described in (Cloude and Papathanassiou, 1998) the optimum coherences are derived. The optimum coherences are denoted as Opt-1, Opt-2 and Opt-3. Figure 5.21 shows the three optimum coherences in grayscale with the values of coherence ranging from 0-1. Figure 5.22 depicts the histogram of the coherences. It is observed that the optimum coherences are derived using the coherence value of each pixel, from the polarizations in three basis, as a criteria. The first optimum polarization, Opt-1 has pixels with highest coherence values followed by Opt-2 and Opt-3. The Figure 5.23 shows the color composite image of Optimal polarization basis. As the forest regions show a dark green appearance, with green

color coding associated to Opt-2 polarization, suggests that Opt-2 polarization may have dominant volume scattering though with low coherence. Similarly the dry riverbed areas show very bright (whitish) appearance signifying high coherence in all three polarizations. Thus the dry riverbed region results in relatively high coherence in all three polarizations, which is qualified by the fact that very low geometric and temporal changes occur in dry riverbed leading to very low decorrelation.

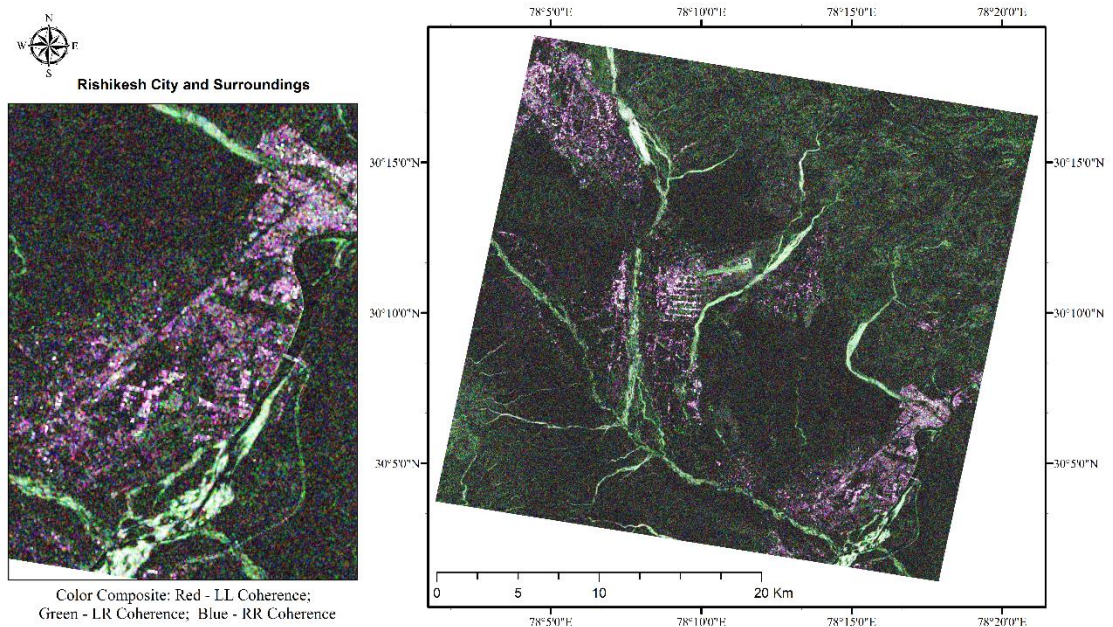


Figure 5.20 Color composite coherence map in Circular-polarization basis. Red –LL; Green – LR; Blue – RR.

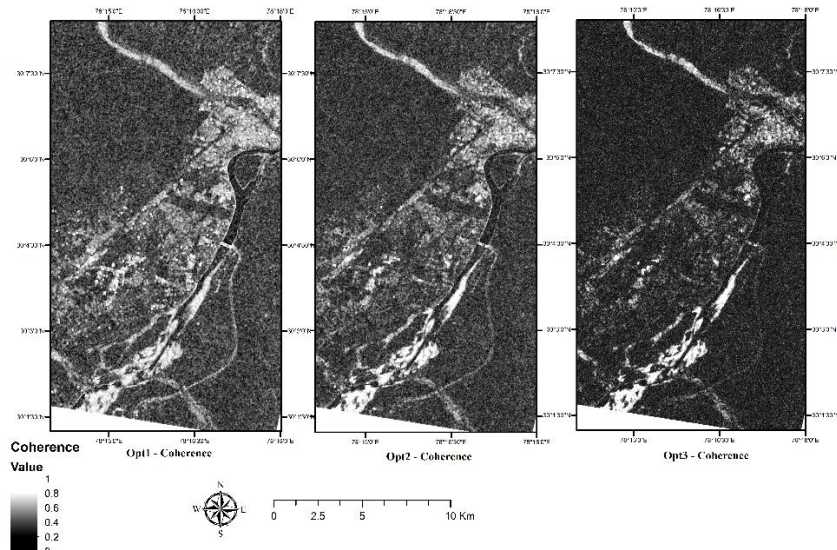


Figure 5.21 Coherence maps in Optimal-polarization basis.

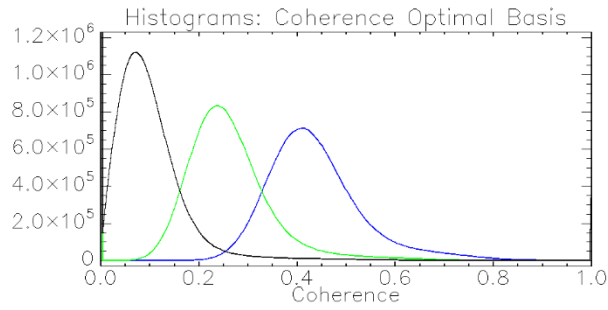


Figure 5.22 Coherence histograms in Optimal (Opt)-polarization basis. Blue – Opt1; Green – Opt2; Black – Opt3.

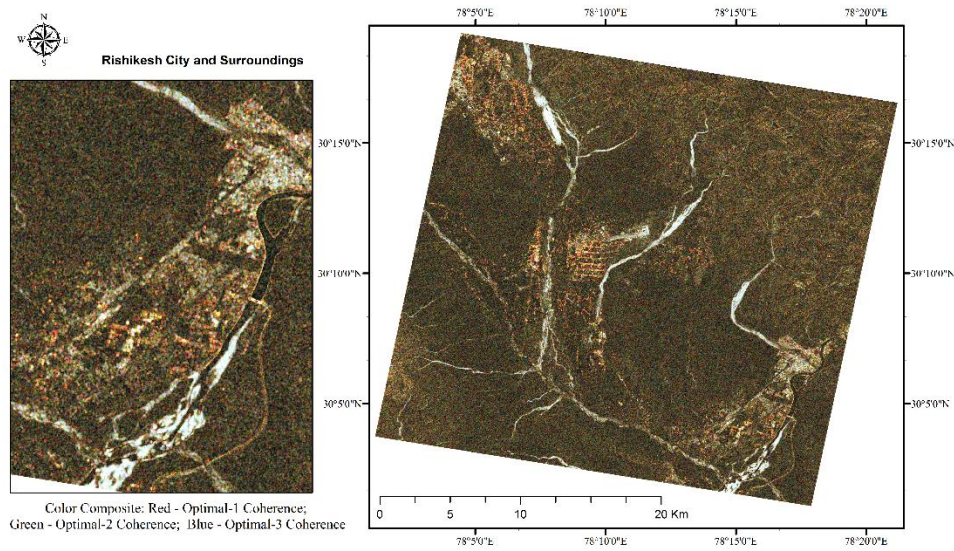


Figure 5.23 Color composite coherence map in Optimal-polarization basis. Red –Opt1; Green – Opt2; Blue – Opt3.

### 5.2.6 Coherence as a function of Ground-to-Volume scattering ratio

This section analyses the coherence behavior in forest regions as a function of scattering pattern. The ground-to-volume scattering ratio provides the ratio of ground scattering with respect to surface scattering. It can also be used to determine the ability of SAR system configuration to separate phase centers of the different polarizations as studied by Krieger *et al.* (Krieger *et al.*, 2005). In the present study, the ground-to-volume scattering ratio provides an estimate of the dominance of ground and surface scattering with respect to coherence, in a particular polarization. Using Yamaguchi four component decomposition technique, the coherence matrix was decomposed to obtain the four scattering components – volume, double-bounce, surface and helix scattering. The ratio of surface and volume scattering power is calculated and converted to decibel (dB) scale for better representation. This ratio is used as the ground-to-volume scattering ratio.

The coherence variations with respect to ground-to-volume scattering ratio for different polarizations in forested area is shown below. Figure 5.24 shows the variation of coherence in different polarization channels with respect to ground-to-volume scattering ratio in the forest range.

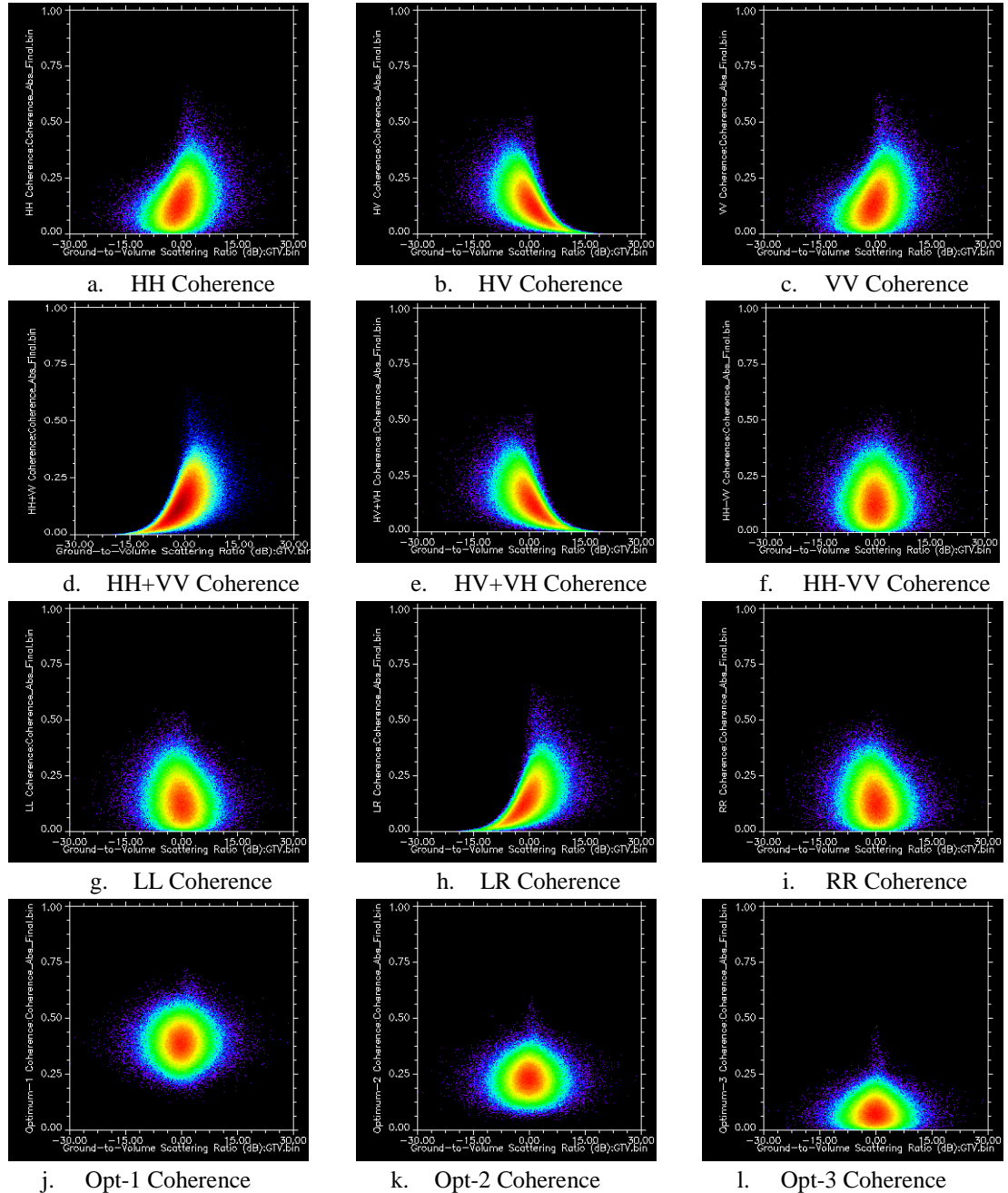


Figure 5.24 Forest region - scatter plots of ground-to-volume scattering ratio with coherence in different polarizations. The x-axis denotes the ground-to-volume scattering ratio in dB scale and the y-axis has coherences in different polarizations. The red-to-blue colors define the density of the points with red representing high density and blue representing low density.

The x-axis represents the ground-to-volume scattering ratio in decibel (dB) scale and the y-axis represents the coherence. The ground-to-volume scattering ratio ranges between (-30dB +30dB). A positive value on the x-axis indicates high ground scattering contribution while a negative value indicates high volume scattering contribution. The coherence values near 0dB are less affected by the ground and volume scattering. For H, V-Polarization basis, the Figure 5.24a, Figure 5.24b and Figure 5.24c, respectively show the variation of coherence in HH, HV and VV polarizations with ground-to-volume scattering ratio. HH and VV coherence maps indicate low dependence on ground and volume scattering with the distribution skewed towards high ground contribution. Whereas HV coherence map shows large number of pixels with high volume scattering contribution. This is understood since, the cross-polarization is dominant in forested regions owing to volume scattering. As volume contribution increases the coherence increases initially and then decreases. The decrease in coherence in areas with high volume scattering is due to increase in volume decorrelation.

The maps in Figure 5.24d, Figure 5.24e and Figure 5.24f depict the variation of coherences with ground-to-volume scattering ratio for Pauli basis. It is known that HH+VV scattering represents surface scattering, HH-VV represents double-bounce scattering and HV+VH volume scattering. This can be easily observed in the graphs. The HH+VV coherence increases with increase in ground-to-volume scattering ratio. Thus with increase in surface contribution, the coherence in HH+VV channel increases. HV+VH coherence shows reverse trend similar to HV coherence. The coherence increases with decrease in ground contribution and increase in volume contribution. The HH-VV coherence is centered on 0 dB with equal distribution. As this polarization channel represents the surface scattering it is not dependent on the ground-to-volume scattering ratio.

For Circular polarization basis, the co-polarized LL and RR coherence have similar behavior as HH-VV while the LR coherence shows behavior similar to that observed in HH+VV coherence. The coherence is low in the negative ground-to-volume scattering ratio region and increases as the ground scattering contribution increases. The optimal polarizations show no dependence on ground or surface scattering with an equiprobable distribution. As observed in Figure 5.24g, Figure 5.24h and Figure 5.24i, the coherence value decreases in the order of the three optimum coherences (Opt-1, Opt-2 and Opt-3).

### **5.2.6.1 Selection of polarization channels to describe Ground and Volume layer**

From the graphs provided in Figure 5.24, it is observed that, the scattering media (vegetation, in this case) interacts in different patterns with SAR waves in various polarization combinations. It is observed that the polarization channels HV and HV+VH best represent the volume scattering as the coherence increases with increased volume scattering contribution. Similarly the polarization channel HH+VV best represents the ground or surface scattering. This is an important observation drawn from this section. The estimation of forest stand height requires selection of polarization channels which best represent volume layer and ground layer. The objective of the analysis carried out in this section was to determine the polarization channels which best describe the volume and ground layer.

### 5.3 Estimation of Forest Stand Height

The forest stand height is estimated using three techniques – DEM Differencing, Coherence Amplitude Inversion and Three Stage Inversion.

#### 5.3.1 DEM Differencing height

This is the simplest technique to estimate the height of the vegetation layer. Interferograms in different polarizations are selected and their Digital Elevation Models (DEM) are generated. The heights derived from these interferograms depend upon the scattering center for the polarization channels. Hence, differences in the DEM provide the difference in the heights of the scattering centers. If accurate phase centers representing top and bottom canopy are selected, the vegetation height can be accurately estimated. Cross-polarized SAR waves, generally have the scattering center in the canopy and hence are used for canopy height estimation. The difference between the DEM derived using the cross- and co-polarized SAR waves provide the height of the canopy.

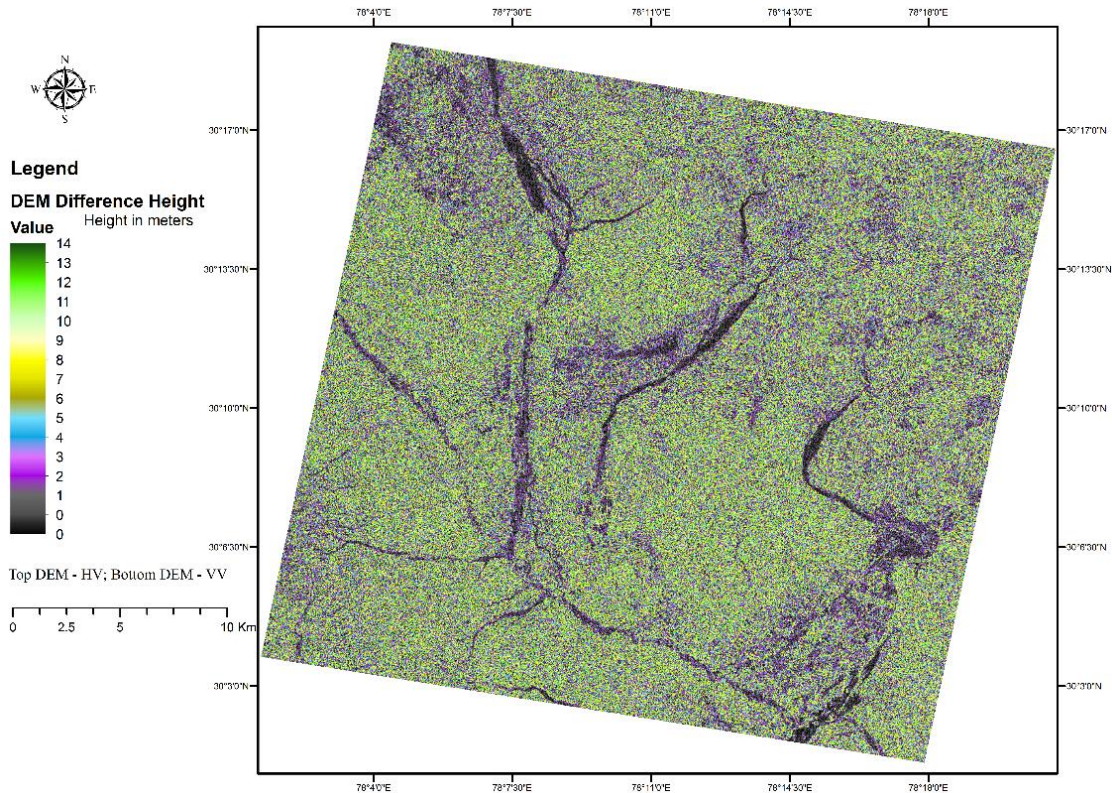


Figure 5.25 DEM Difference height. Top DEM: HV; Bottom DEM: HH+VV.

Figure 5.25 shows the DEM difference height obtained using HV and VV polarization channels selected for generating top and bottom DEM's. The DEM obtained using HV polarization provides DEM corresponding to top of canopy while the VV polarized DEM provides the near-ground DEM. The height obtained using this technique varies between 0 meters and 14.17 meters. As mentioned in the Sec. 3.2.2, the field data collected for Barkot and Thano forest ranges has a

mean height of 23.90 meters. But the height estimated using DEM Difference technique has a maximum height of 14.17 meters and mean height of 4.06 meters. Similar results are obtained in previous studies (Cloude, 2006, 2005) as explained in Section 2.8. The DEM Difference heights with different combinations of polarizations for top and bottom DEM are analyzed. However similar results are obtained. The maximum derived height does not exceed 14.5 meters. One important observation of this technique is that it estimates the height of dry riverbed regions accurately. As seen in Figure 5.25, the height estimated for dry river channels is in the range of 0-2 meters. This technique accurately estimates the height in the dry-river bed regions. The height is underestimated for forest regions. The technique overestimates the height of water surface and urban regions.

### 5.3.2 Coherence Amplitude Inversion Height

The second technique applied to the PolInSAR data is the coherence amplitude inversion technique explained in (Cloude, 2005). It is an alternative to the DEM differencing approach. It requires selection of two polarization channels. One channel is selected which represents only volume scattering while the other is believed to represent the surface scattering. The polarization channels are selected from the analysis carried out in Sec. 5.2.6. As concluded in Sec. 5.2.6.1, HH+VV best represents ground layer and HV+VH best represents the volume layer.

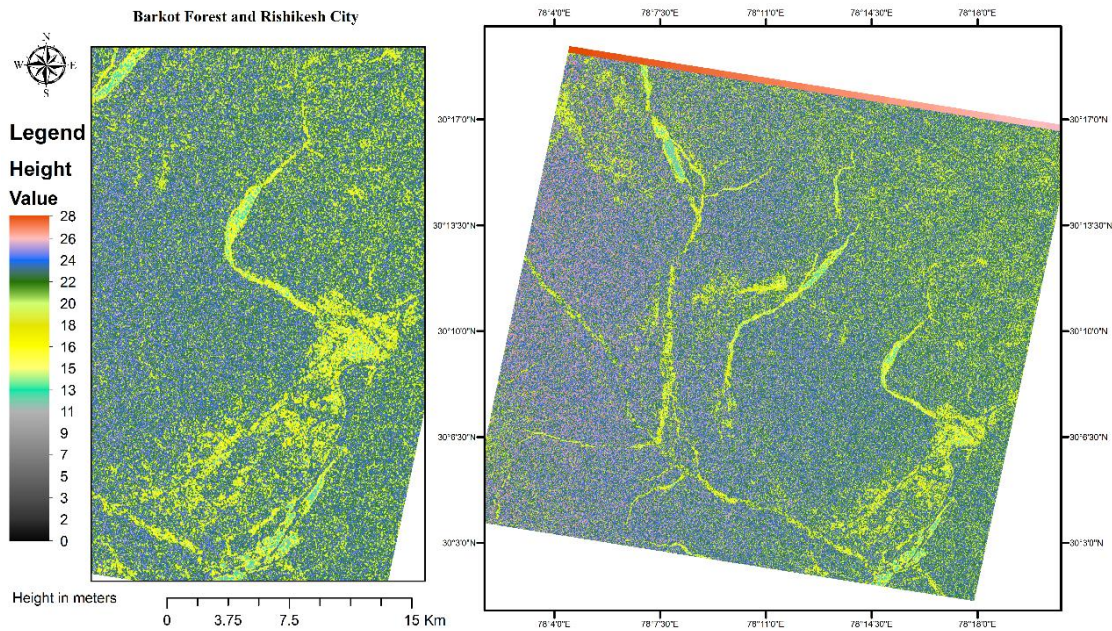


Figure 5.26 Coherence Amplitude Inversion height with using HV+VH polarization for volume dominated coherence and HH+VV polarization for surface coherence.

Figure 5.26 shows a forest height map with the two polarizations selected from Pauli basis. Using these two polarization channels the forest canopy height is estimated. It is observed that the height is over-estimated for urban and dry riverbed with the height in these regions in the range of 15-20m. Ideally, the estimated height in these regions should be near 0 m for dry riverbed and <10

meters for urban areas as very tall structures are not present in Rishikesh city. The Thano and Barkot forest range canopy height ranges from 16 to 28 meters. The distribution of canopy height is shown in the histogram in Figure 5.27. The mean height is 23.11 meters with standard deviation of 2.41 meters.

A

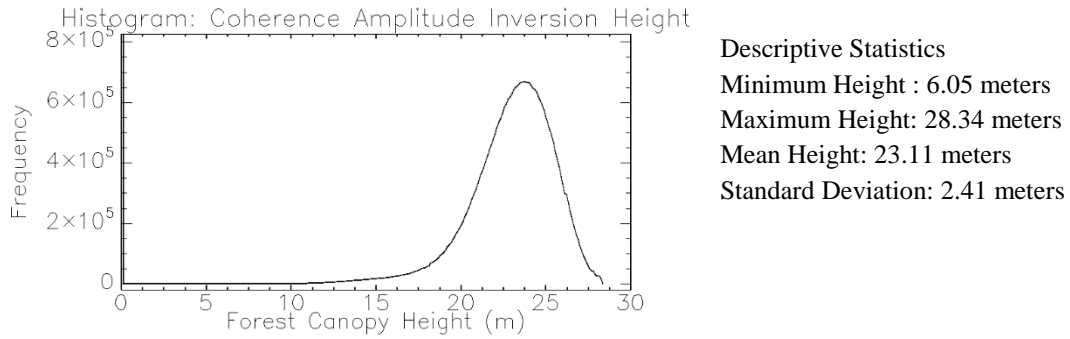


Figure 5.27 Coherence Amplitude Inversion height histogram. The descriptive statistics are provided on the right side.

### 5.3.2.1 Validation and Accuracy Assessment

The coherence amplitude inversion technique- derived forest height is validated against the field height. Forest stand height was measured at 100 locations across Thano and Barkot forest. The method used for field data collection is explained in Sec. 3.2.2. The descriptive statistics comparing the field data with the coherence amplitude inversion height are shown in Table 5.7.

Table 5.7 Statistics – Coherence amplitude inversion height and Field height (H\_avg)

Statistic	Derived Height	Field Height (H_avg)
Minimum	20 m	15 m
Mean	23.61 m	23.44 m
Maximum	27 m	29 m
Standard Deviation	1.71	2.87
Skewness	-0.147	-0.282
Kurtosis	-0.768	-0.001

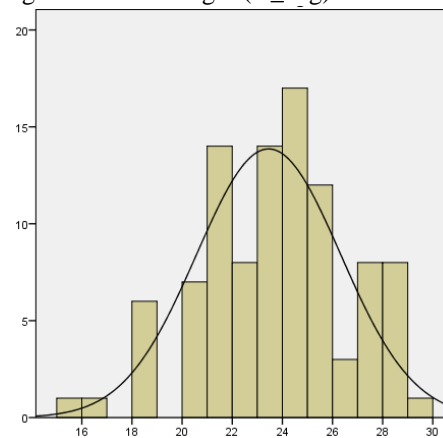


Figure 5.28 Histogram of Field measured forest height.

The tree height is measured in the forest at 100 locations. Figure 5.28 shows the histogram of the average tree height measured in the field. It is denoted as H\_avg. Figure 5.29 shows the histogram

of the tree height derived using the coherence amplitude inversion technique and Figure 5.30 shows the box plot distribution of the data.

The black line in the histograms is the ideal normal distribution line. To verify if the sample plots are a part of normally distributed data, tests of normality are used. Shapiro-Wilk test for normality is used here. The samples size for the test is N=100. The results are presented in Table 5.8. The p-value is the significance value for the data. For a confidence interval of 95%, the p-values are tabulated. Since both the p-values are greater than 0.05, it can be assumed that the plots are part of a normally distributed population. The same can also be visually verified using a Q-Q plot.

Table 5.8 Test of Normality of Data for coherence amplitude inversion height and Field height (H\_avg)

Data	Samples (N)	Significance (p-value)	95% Confidence Interval	
			Upper Bound	Lower Bound
Field Measured Height	100	0.107	24.01	22.88
Coherence Amplitude Inversion Height	100	0.094	23.95	23.27

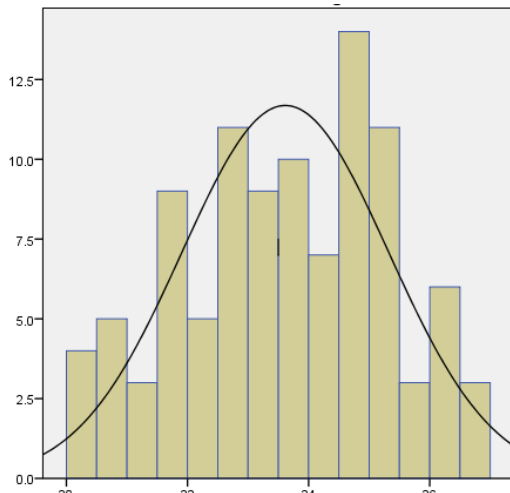


Figure 5.29 Histogram of derived forest height using Coherence Amplitude inversion technique.

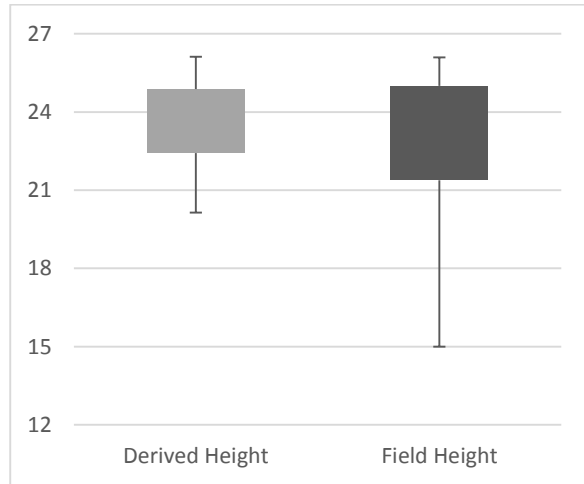


Figure 5.30 Box plot plot of the Coherence amplitude inversion forest height and field measured tree height.

The accuracy assessment for the coherence amplitude inversion technique derived forest height is presented in Table 5.9. The reference height for accuracy assessment is the field measured forest height. The sample data size is 100. The estimated height has a Root Mean Square Error (RMSE) of 2.76m for a mean estimated height of 23.61m. The average accuracy of this method is 90.10%. The average accuracy is derived using (Wang and Ouchi, 2010)

$$\sigma_M = 1 - \frac{1}{N} \sum_{i,j=1}^N \frac{|H_i - H_j|}{H_j} \tag{5.6}$$

Where  $\sigma_M$  is the average accuracy, N is the number of samples,  $H_i$  is the estimated height using the technique and  $H_j$  is the field measured tree height.

Table 5.9 Accuracy assessment results for coherence amplitude inversion height

Forest Height Derived Using	Mean height	Variance	RMSE	Correlation	Average Accuracy
Coherence Inversion Amplitude Height	23.61 m	2.922	2.77 m	0.34	90.10%

It is observed that though the accuracy of tree height estimation is high, but the correlation is very low at 34%. The scatter plot is shown in Figure 5.31. The plot shows the comparison of the field measured height data with the derived data.

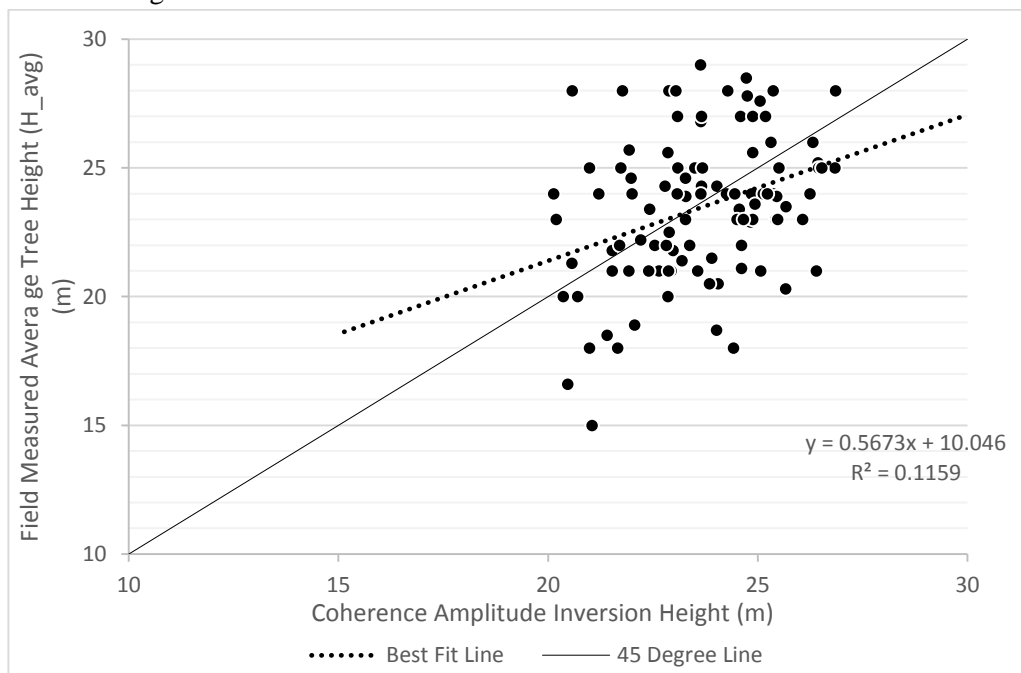


Figure 5.31 Scatter plot for the height derived using the Coherence Amplitude Inversion Technique. The solid line is the line at 45° and the dotted line is the best fit line through the plots. The  $R^2$  value is low at 0.1159 corresponding to a correlation of 0.34.

### 5.3.3 Three Stage Inversion Technique

The ‘Three Stage Inversion’ technique (Sec. 2.7) is applied to the PolInSAR data using the derived coherences in various polarization basis. The height of the forest stand is estimated and the height map is shown in Figure 5.32. This technique utilizes the complex coherences computed for different polarization basis. The complex coherences are plotted on complex plane and using the technique described in (S. Cloude and K. P. Papathanassiou, 2003) the forest stand height is estimated for each resolution cell. A brief description of the technique is provided in Appendix 2. The estimated tree height ranges from 8 – 27m. The different colors in Figure 5.32 denote the height range. It is observed that the ‘Three Stage Inversion’ technique overestimates the height

of the urban and dry riverbed regions. The height in these regions is in the range of 12 - 16m. The agricultural areas to the south of the Jolly Grant Airport, in the center of the image, also presents with high vegetation height of around 17 – 20m. The derived forest height varies between 18 - 27m.

### 5.3.3.1 Validation and Accuracy Assessment

‘Three Stage Inversion’ technique derived height is validated and its accuracy assessed. The tree height is collected during the field survey. This estimated tree height is validated against the field data. The descriptive statistics for the ‘Three Stage Inversion’ technique derived height and the field height is presented in Table 5.10.

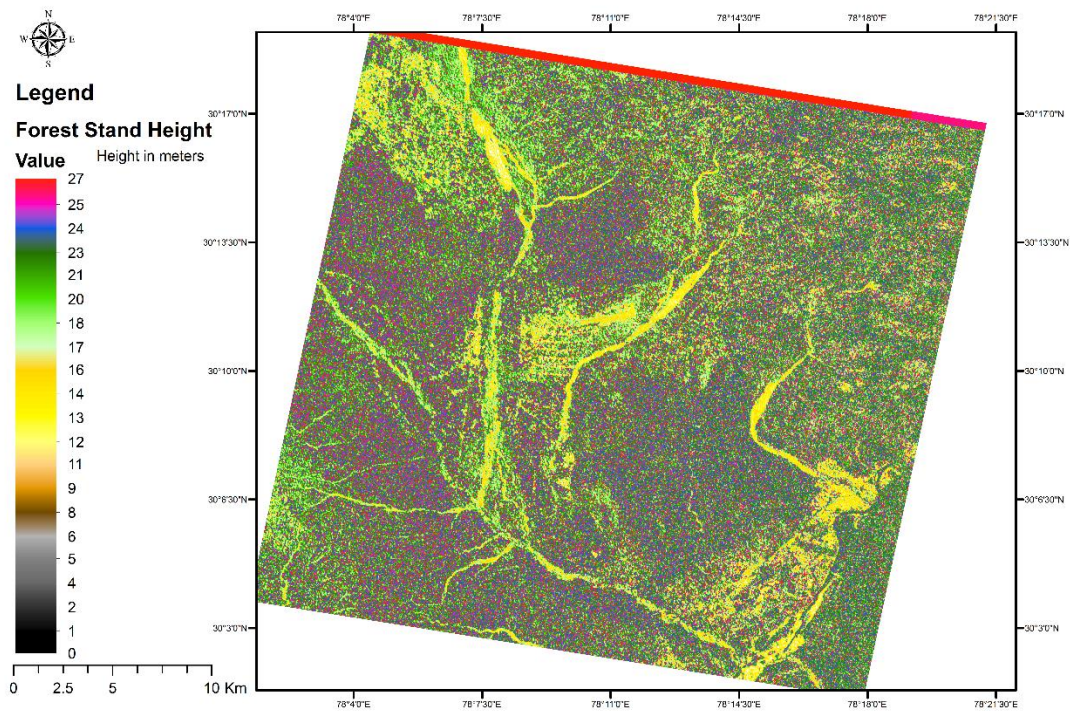


Figure 5.32 Forest Stand Height estimated using ‘Three Stage Inversion’ technique.

Table 5.10 Statistics – Three Stage inversion height and Field height ( $H_{avg}$ )

Statistic	Derived Height	Field Height ( $H_{avg}$ )
Minimum	18 m	15 m
Mean	22.98 m	23.44 m
Maximum	27 m	29 m
Standard Deviation	2.122	2.87
Skewness	-0.4	-0.277
Kurtosis	-0.563	-0.078

The Figure 5.33 shows the histogram of the tree height estimated using the three stage inversion method. The black line in the histogram is the ideal normal distribution line. It is observed from the histogram that the derived height is skewed towards higher tree heights. The test of normality

is applied to the estimated forest height. The Shapiro-Wilk test results are presented in Table 5.11. The  $p$ -value for the derived height is 0.001. For a confidence interval of 95%, the threshold  $p$ -value for passing the test of normality is 0.05. The derived height samples do not belong to a normally distributed data. The box plot of the derived height and the field height is shown in Figure 5.34

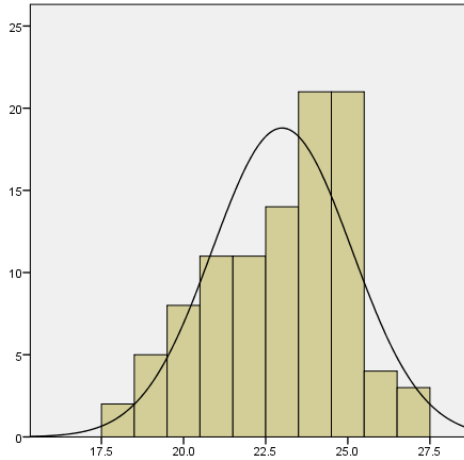


Figure 5.33 Histogram of ‘Three Stage Inversion’ technique derived Forest Height

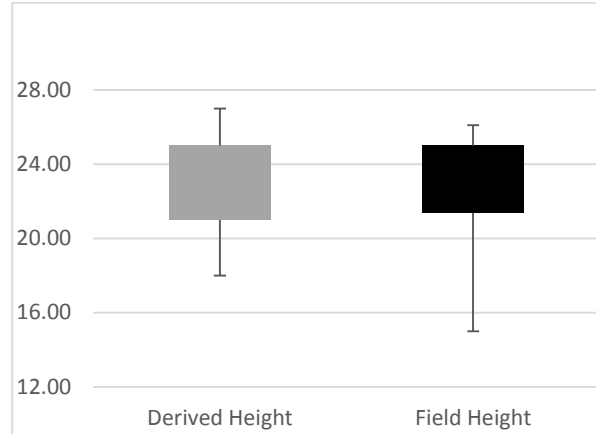


Figure 5.34 Box plot of the ‘Three Stage Inversion’ technique derived Forest height and the field measured tree height

Table 5.11 Test of Normality of Data for Three Stage Inversion height and Field Height ( $H_{avg}$ )

Height Type	Samples (N)	Significance ( $p$ -value)	95% Confidence Interval	
			Upper Bound	Lower Bound
Field Measured Height	100	0.107	24.01	22.88
Three Stage Inversion Height	100	0.001	23.42	22.58

The results for the accuracy assessment for the ‘Three Stage Inversion’ technique derived forest height is tabulated in Table 5.12. For the 100 samples collected the RMSE calculated is 2.28m for a mean height of 23m. The correlation is higher than the coherence amplitude inversion technique at 0.62. The average accuracy for this technique is high at 91.56%.

Table 5.12 Accuracy Assessment Results for ‘Three Stage Inversion’ technique height

Forest Height Derived using	Mean height	Variance	RMSE	Correlation	Average Accuracy
‘Three Stage Inversion’ technique	23 m	4.505	2.28 m	0.62	91.56 %
Coherence Amplitude Inversion Technique	23.61 m	2.922	2.76 m	0.34	90.10%

The Figure 5.35 shows the scatter plot for the field measured height and the three stage inversion derived height. The  $R^2$  value for 100 plots is 0.3877. It is observed from Table 5.9 and Table 5.12 that the ‘Three Stage Inversion’ technique produces accurate results as compared with the coherence amplitude inversion technique. The correlation of the field and derived height using

the ‘Three Stage Inversion’ technique is superior to that obtained from the coherence amplitude inversion technique.

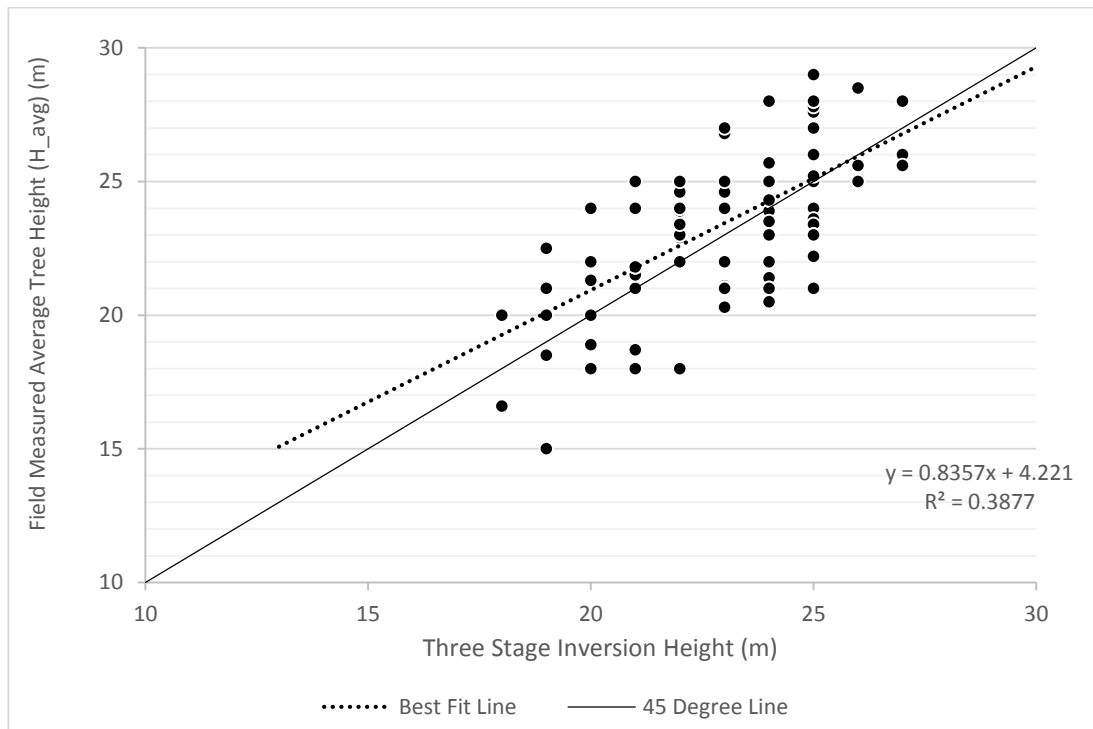


Figure 5.35 Scatter Plot - Three Stage Inversion Height vs Field Measured Average height (H\_avg). The solid line is the line at 45° and the dotted line is the best fit line through the plots. The R2 value is 0.3877 corresponding to a correlation of 0.623.

### 5.3.3.2 Source of Errors in the plots

It was observed that some plots had high errors in height estimation. Plots were identified which had error greater than two standard deviations from the mean height. 16 such plots were identified which had high error in estimated height. These plots were analyzed individually and probable reasons and sources of error were estimated. The plots are grouped into four classes. The probable sources of error for first three groups are enumerated below. For the two plots in Group IV, cause for error in estimation could not be ascertained. Table 5.13 provides the plots in each group. The plot location can be referred to in Appendix I.

Table 5.13 Groups of Plots with high error in height estimation

Overall it was observed that the derived height is underestimated as compared to the field height.

Group	Plots	Group	Plots
I	3, 25, 29, 31, 65, 67	III	6, 27
II	8, 20, 22, 33, 42, 49	IV	39, 44

The probable reasons for error in estimation of height for the three groups are:

- I. The forest stand in these 6 plots are in multiple stages of growth. In these plots, there is mature Sal and Teak species with new plantations of Teak. Up to three distinct levels of growth of forests were observed in plot 3 and 29. Due to multiple scattering centers as probable polarization independent volume scatterers, vegetation bias increases. The bias increases when multiple volume scatterers are present at different heights. As observed in Sec. 5.2.6, the coherence values in forest regions are low. This further leads to inaccuracies in estimation of true ground phase center. This can lead to underestimation of forest height as observed in plots in Group I.
- II. In the 6 plots in this group, there is presence of mixed plantations. Three plots, 20, 33 and 42 are in the sparse Khair-Sisoo forests. The height is overestimated in plot 20 and 42. In these plots, the Khair and Sisoo species is in abundance along with Bel (*Aegle marmelos*). The plots have low Khair and Sisoo (typically 15-22m high) with intermittent high Sal and Teak (between 24 – 32m) plantations. As the Khair and Sisoo species are deciduous, they are leafless during early spring. The volume scattering center is located in the canopy of the lone Sal or Teak tree in the plot. This may have lead to overestimation of height in these plots. In plot 33, there is a mixture of Sal, Teak with evergreen species of Jamun (*Syzygium cumini*) and Tendu (*Diospyros melanoxylon*). These trees have a dense canopy leading to high extinction of SAR wave. It can lead to underestimation of height.
- III. In the plot 6 and 27, very dense understory comprising of Curry leaf tree and Lantana is found. Dense understory can lead to underestimation of tree height.

These 16 plots were excluded and the accuracy assessment was carried out. It can be seen from Table 5.14 that the correlation increases to 0.71 from 0.62 corresponding to  $R^2$  value of 0.51. This  $R^2$  value is higher than 0.38 for the 100 plots. Figure 5.36 shows the scatter plot between the field height and the derived height for the 84 plots.

Table 5.14 Accuracy assessment after excluding the outlier plots.

Forest Height Derived using	Mean height	Variance	RMSE	Correlation	Average Accuracy
'Three Stage Inversion' technique – 100 Plots	23 m	4.505	2.28 m	0.62	91.56 %
'Three Stage Inversion' technique – 84 Plots	23.12 m	4.49	2.16 m	0.712	94.07%

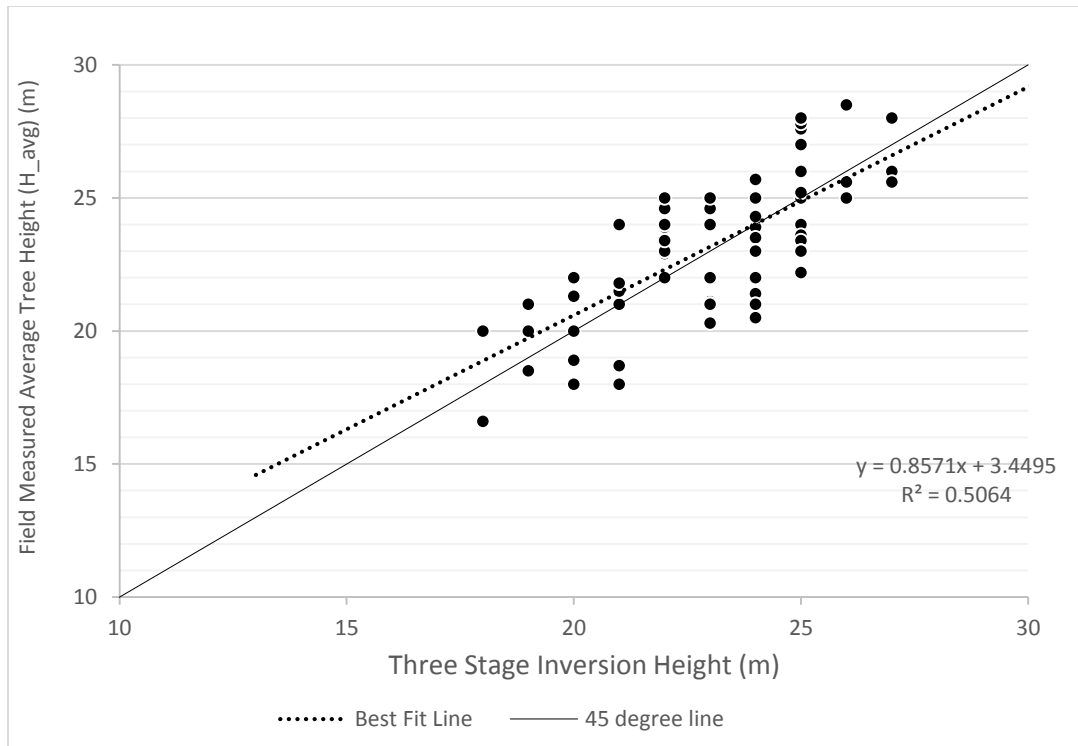


Figure 5.36 Scatter plot for ‘Three Stage Inversion’ technique after excluding the outliers

An attempt has been made here to explain the outliers and the source of errors in the individual plots.

It can be observed that the accuracy of tree height estimation by Three Stage Inversion technique is 94.07% as measured against field data for the 84 plots in the Barkot and Thano forests. The plots are distributed evenly across the different forest types and it must be noted that the forest is dominated by Sal and hence most of the plots are in the Sal dominated patch. For the areas which could not be surveyed for field data, the accuracy of estimated height may not vary more than the RMSE of the height collected from the plots. Hence the accuracy for the non-surveyed areas of forests should have an accuracy closer to 91%.

### 5.3.4 Improved Three Stage Inversion Technique

The improved ‘Three Stage Inversion’ technique is proposed in Sec. 4.3. Figure 5.37 shows a subset view of the forest height estimated using the ‘Three Stage Inversion’ technique. Two transects are shown in the map. Transect in the upper part of the image goes through Barkot forest range and a dry riverbed while the second transect passes through Rishikesh urban area and River Ganga. The height profiles for the two transects are shown in Figure 5.38 and Figure 5.39.

The coherence threshold is calculated using methods described in Sec.4.3. The coherence threshold can delineate the dry riverbed and urban regions from the forest and water areas. The map and height profile showing changes in height after applying the coherence threshold are shown in Figure 5.40.

**Coherence Threshold** – Transect-1 passes through the dry riverbed. As observed in transect shown in Figure 5.38 the height of the dry river bed is inaccurately estimated at 15m in the ‘Three Stage Inversion’ technique. After applying the coherence threshold, the dry riverbed height is estimated at 0 m above the ground as shown in Figure 5.41. Transect-2 passes through the urban (pixels 50-170) and river areas (pixels 180-250). In the vertical profiles in Figure 5.39, urban height is overestimated at 15m whereas the water height is around 20m. After application of

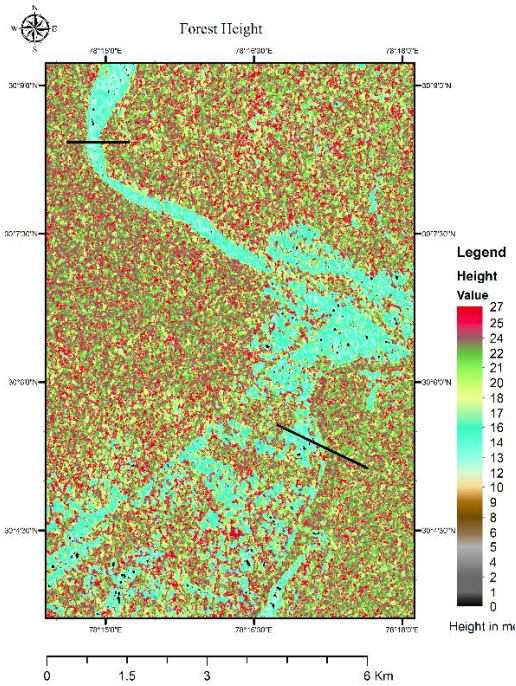


Figure 5.37 Forest Height Map generated using ‘Three Stage Inversion’ technique. Transect-1 is at the top of the image, passes through dry-river. Transect-2 at the center of the images passes through urban regions and River Ganga.

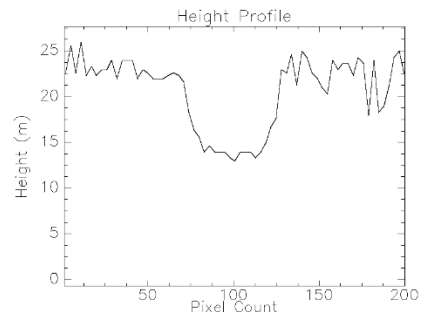


Figure 5.38 Transect-1 Height Profile

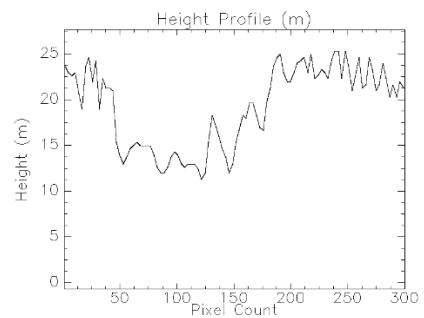


Figure 5.39 Transect-2 Height Profile

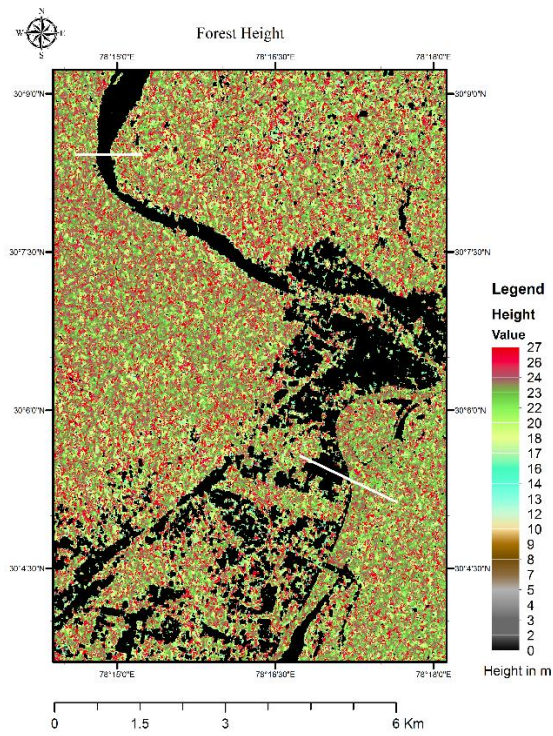


Figure 5.40 Forest Height Map generated using Improved ‘Three Stage Inversion’ technique. The coherence threshold is applied. Transect-1 is at the top of the image, passes through dry-river. Transect-2 at the center of the images passes through urban regions and River Ganga.

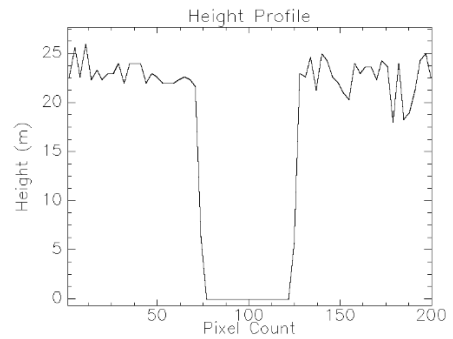


Figure 5.41 Transect-1 Height Profile

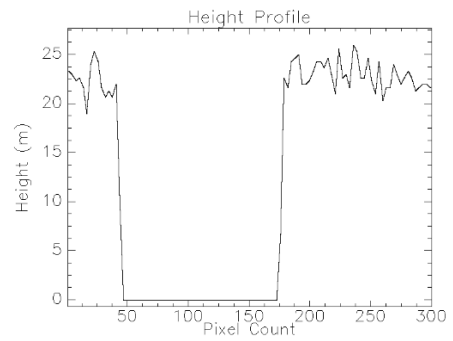


Figure 5.42 Transect-2 Height Profile

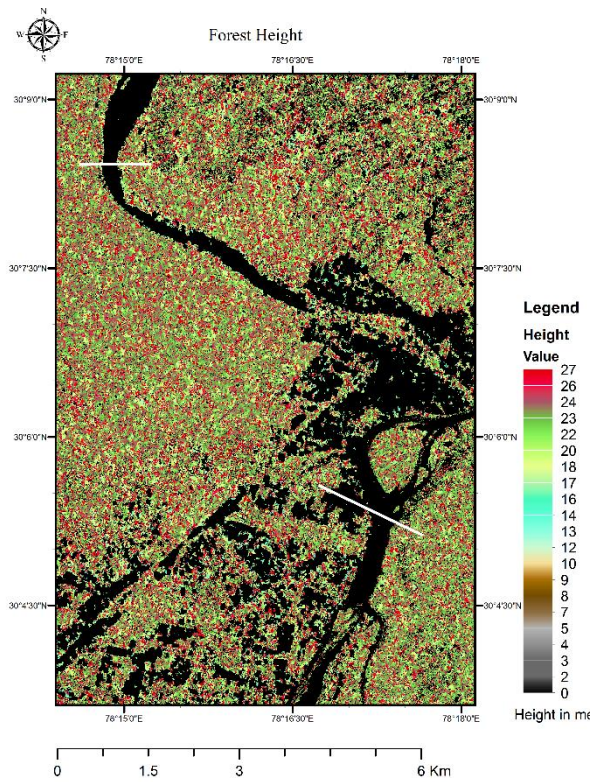


Figure 5.43 Forest Height Map generated using Improved ‘Three Stage Inversion’ technique. Coherence and Backscatter threshold are applied. Transect-1 is at the top of the image, passes through dry-river. Transect-2 at the center of the images passes through urban regions and River Ganga.

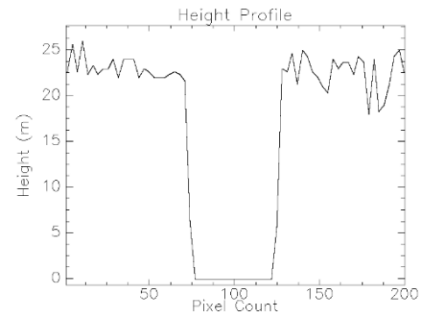


Figure 5.44 Height Profile Transect-1

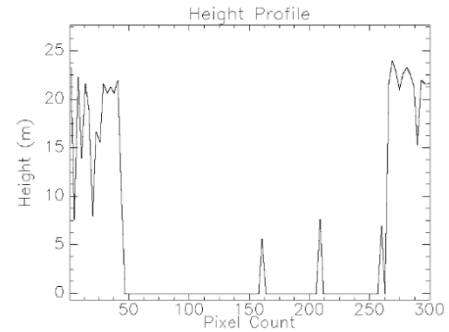


Figure 5.45 Height Profile Transect-2

coherence threshold, the urban area height is reduced to 0m, however the water level height is still overestimated as shown in.

**Backscatter Threshold** - Application of backscatter threshold does not change the height in the dry riverbed as this threshold delineates the water and non-water regions only. The effect of the application of backscatter threshold can be observed in Figure 5.45. The river height above the surface is now near 0 m as expected. The few peaks in the middle are due to presence of vegetated patches on the banks of the river. Thus the application of the coherence and backscatter threshold leads to delineation of forests and vegetated areas from dry riverbed, urban and water bodies. This provides an accurate estimation of the height of water bodies and dry riverbeds.

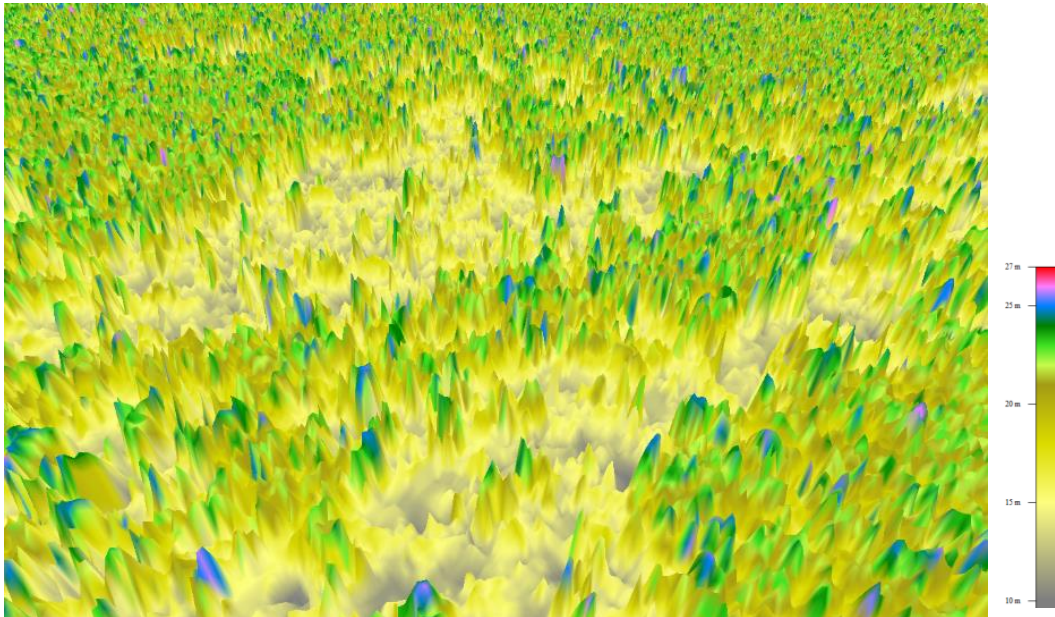


Figure 5.46 Three-dimensional representation of the height difference between effective phase scattering centers of the Barkot forest area.

Three dimensional view of Barkot forest and Rishikesh can be seen in the Figure 5.46. The height varies between 10m and 26m in the view. The low lying areas are the Rishikesh city and the Barkot forest can be seen. Appendix 5 provides a few more three dimensional views of the study area.

## **6. CONCLUSION AND RECOMMENDATIONS**

---

### **Conclusions**

The present study has shown the effect of shift in polarization orientation angle on multi-frequency PolSAR data. The results presented have some interesting findings. One major observation is the change observed in helix scattering power post-POA compensation. This is contrary to the available literature. This research has shown the varying effect of POA shift on different scattering surfaces when illuminated with SAR waves in various frequency bands.

The present work also signifies the importance of PolInSAR based tree height estimation. Two PolInSAR techniques are compared and it is concluded that the ‘Three Stage Inversion’ technique is a robust and accurate technique for forest height estimation. This method is suitable for measuring the height of large swaths of forested areas. In the present study, the technique is applied to tropical forest area, it may also be applied to evergreen inaccessible forested areas. The coherence and backscatter based approach for improvements in the tree height estimation techniques are also demonstrated in this research. The utility of this approach is successfully demonstrated using the threshold approach for vegetated area identification.

The limitations of the present work are incorporated for further improvements in techniques for accurate estimation of tree height using PolInSAR techniques. A major limitation for validation of this study is the non-availability of airborne LIDAR data for tree height validation. With LIDAR data, ground survey can be undertaken in large, inaccessible areas, and the tree height can be validated using larger datasets. The present space-borne PolInSAR data is acquired in C-band. However, with longer wavelength data (P- and L- bands), the uncertainty in the tree height estimated also increases. Hence there is a need for acquisition of PolInSAR data and its processing at different wavelengths to obtain accurate height estimation. The present study utilizes only one set of PolInSAR data. With large pairs of PolInSAR data, the validation of the methodology can be more accurate. Larger datasets, both of PolInSAR data and the LIDAR data can lead to better validation of the methods employed in the present study.

The conclusions of the research work are presented in the form of the answers to the research questions.

### **1. How do complex coherence in different polarizations, vary for different scattering media?**

The three principle polarization basis discussed in the present work are Linear, Pauli and Circular basis. The optimal basis as shown in Sec. 5.2.5 and Sec. 5.2.6 is an Eigen value based optimization technique which divides the complex coherences in accordance to increasing coherence values. The linear and Pauli basis are interrelated as the Pauli basis is derivative of

the Lexicographic basis polarization. As shown in Sec. 5.2.5, the scatterers act in different manner with different polarization basis.

The vegetated areas act as volume scatterers. Here the geometrical decorrelation in the form of volume decorrelation is dominant reducing the coherence. This is evident in all the three polarizations. Hence the forests appear as a dark green region in all the three polarization basis. The dry riverbed has rocks and sand. The rocks and dry ground lead to double-bounce scattering as well as surface scattering. This results in very low geometrical decorrelation and stable backscatter pattern. The sand, if deep, may acts as volume scatterer as the SAR wave can penetrate the surface. This results in volume decorrelation. The dry riverbed has high coherence in all three polarizations of the linear basis resulting in bright pattern (Figure 5.14). In Pauli basis, the delineation of surface and double-bounce scattering is better. Thus the dry riverbed, having high overall coherence, has dominant HH+VV coherence, which can be attributed to higher stable surface scatterers. In the Circular polarization, the cross-polarized LR coherence is higher, suggesting that the scattering media results in higher stable pattern of cross-polarized component in Circular polarization. Thus it is concluded that the same scattering media (dry riverbed) leads to stable scattering in all three polarizations of Linear polarization, the scatterer is better identified in Pauli basis as surface scatterer whereas in Circular basis it generates stable cross scattering.

Thus complex coherence in different polarizations vary for a scattering media.

## **2. What will be the effect of POA shift on multi-frequency PolSAR data?**

The effect of POA shift on multi-frequency PolSAR data is analyzed using the Yamaguchi decomposition results in Sec. 5.1.3. The conclusions are drawn as follows

- a. The double-bounce scattering power increases after compensating for the shift in POA. The increase in double-bounce scattering power is higher for increasing frequencies of operation of SAR sensor.
- b. The surface scattering power increases after deorientation. The increase is high for C-band data as compared to the increase observed in L- and X-band.
- c. The volume scattering power decreases overall and the decrease is highest for X-band followed by L- and C-band.
- d. Contrary to the literature available, the helix scattering power shows change after deorientation. The helix scattering power decreases for L- and C-band. For X-band, the data shows noisy behavior and could not be analyzed.
- e. The decrease in double-bounce scattering power is lower than the increase in volume scattering power for L- and C-band data, after deorientation. This is contrary to the observations made in literature using airborne SAR data.

It is concluded that the shift in POA leads to incorrect estimation of the scattering pattern of the scattering media which leads to inaccuracies in estimation of geophysical and biophysical parameters. Hence it is concluded that POA shift compensation is essential for PolSAR data.

**3. Does POA shift compensation affect the PolInSAR data?**

As shown in Appendix-3, the POA shift compensation does have an effect on the PolInSAR data. As the POA shift compensation is applied on the scattering matrices of the two acquisitions at the ends of the baseline, the PolInSAR observable,  $T_6$  matrix is affected. This leads to changes in the complex coherence pattern observed and the derived forest stand height. As observed in Appendix-3.1, the complex coherence calculated shows a major change in the coherence pattern for forests, dry riverbed as well as urban areas. The scattering pattern observed for different regions changes after POA shift compensation.

**4. What is the effect of deorientation on the modeled forest height?**

The modeled forest height using ‘Three Stage Inversion’ technique changes after deorientation. The average estimated forest height increases after deorientation. The accuracy of estimation of tree height decreased after deorientation. It is concluded that POA shift compensation is not suitable for PolInSAR based tree height estimation.

**5. Which among Coherence Amplitude Inversion (CAI) and Three stage inversion (TSI) technique is more robust and better suited for estimation of forest stand height?**

Three stage inversion (TSI) technique is more robust as compared to Coherence Amplitude Inversion (CAI) technique. The CAI technique ignores phase information and is sensitive to extinction and structure variations. Also CAI requires *a priori* information for selection of polarization channels. On the other hand TSI technique utilizes the phase and also takes into consideration tree structure and extinction estimation (see Appendix 2).

**6. What is the accuracy of the estimated forest height using both the Coherence Amplitude Inversion (CAI) and Three stage inversion (TSI) technique when compared with field measured height?**

The accuracy assessment results for tree height estimation using CAI and TSI technique are presented in Table 5.9 and Table 5.12 respectively. It is observed that TSI technique produces more accurate results as compared to those obtained from CAI technique. The correlation between field measured height and the PolInSAR derived height is higher for TSI technique as compared to CAI. The correlation between the field measured forest height and the estimated tree height using TSI technique is 62% with an average accuracy of 91.56% and RMSE of 2.28m. Whereas the values using CAI technique stand at 34% correlation with 90.10% average accuracy and RMSE of 2.76m. Thus is concluded that the TSI technique produces more accurate and correlated results as compared to CAI technique.

**7. Is backscatter and coherence based approach suitable for improvements in the algorithm for vertical tree height estimation?**

Yes, the backscatter and coherence based approach is suitable for delineation of non-forested regions from forested regions. The Improved ‘Three Stage Inversion’ technique is successfully demonstrated in Sec. 5.3.4. The coherence and backscatter approach is applied in the present

work. Using threshold for coherence, the dry riverbed and urban areas are identified and after applying backscatter threshold, the forested areas are delineated from non-forest regions.

### **Recommendations**

Shift in Polarization orientation angle leads to inaccurate estimation geo-physical and bio-physical parameters. For PolSAR data, it is recommended that, POA shift compensation should be a standard pre-processing step. Further physics based approach is necessary for analysis of the effects of POA shift on PolInSAR data and the modeled vegetation height.

The present study applies Single-baseline PolInSAR techniques to C-band RADARSAT-2 data. Further research is recommended using multi-baseline data in L- and P-band, capable of penetrating dense canopy surfaces. Also more pairs of PolInSAR data are recommended as larger number of datasets offer better validation of results. Validation of the tree height is recommended using airborne LIDAR measurements for better coverage in inaccessible forest areas.

## REFERENCES

---

- Ballester-Berman, J.D., Lopez-Sanchez, J.M. (2010). Application of Freeman-Durden Decomposition to Polarimetric SAR Interferometry. *EURSAR, 8th European Conference on Synthetic Aperture Radar* (pp. 1–4.). Germany: Aachen.
- Ballester-Berman, J.D., Lopez-Sanchez, J.M. (2010). Applying the Freeman-Durden Decomposition Concept to Polarimetric SAR Interferometry. *IEEE Transactions on Geoscience and Remote Sensing* 48(1), 466–479. <http://dx.doi.org/10.1109/TGRS.2009.2024304>.
- Ballester-Berman, J.D., Lopez-Sanchez, J.M., Fortuny-Guasch, J. (2005). Retrieval of biophysical parameters of agricultural crops using polarimetric SAR interferometry. *IEEE Transactions on Geoscience and Remote Sensing* 43(4), 683–694. <http://dx.doi.org/10.1109/TGRS.2005.843958>.
- Binghuang, Z., Bing, C. (2007). An analysis of coherence optimization methods in PolInSAR. *APSAR, 1st Asian and Pacific Conference on Synthetic Aperture Radar* (pp. 577–579). China: Huangshan. <http://dx.doi.org/10.1109/APSAR.2007.4418678>.
- Boerner, W.-M. (2004). Recent advances in Radar Polarimetry and Polarimetric SAR Interferometry. Presented at the RTO SET Lecture Series on “Radar Polarimetry and Interferometry,” Washington DC, USA, pp. 8–1 to 8–30. <http://ftp.rta.nato.int/public/PubFullText/RTO/EN/RTO-EN-SET-081/EN-SET-081-08.pdf> (accessed June, 2014).
- Boerner, W.-M. (2006). Recent advances in Polarimetry and Polarimetric Interferometry. *2006 IEEE International on Geoscience and Remote Sensing Symposium* (pp. 49–51). USA: Denver. <http://dx.doi.org/10.1109/IGARSS.2006.17>.
- Cai, H., He, P., Zou, B., Lin, M. (2011). Building parameters extraction from PolInSAR image using hybrid method. *2011 IEEE International on Geoscience and Remote Sensing Symposium* (pp. 382–385). Canada: Vancouver. <http://dx.doi.org/10.1109/IGARSS.2011.6048979>.
- Cloude, S., Papathanassiou, K.P. (2003). Three-stage inversion process for polarimetric SAR Interferometry. *IEEE Proceedings on Radar, Sonar and Navigation* 150(3), 125–134. <http://dx.doi.org/10.1049/ip-rsn:20030449>.
- Cloude, S.R. (2005). Pol-InSAR Training Course (Manual), PolSARpro. ESA. [http://earth.esa.int/polsarpro/Manuals/1\\_Pol-InSAR\\_Training\\_Course.pdf](http://earth.esa.int/polsarpro/Manuals/1_Pol-InSAR_Training_Course.pdf). (accessed May, 2014).
- Cloude, S.R. (2006). Polarization coherence tomography. *Radio Science*. 41(4), RS4017, 1 – 27. <http://dx.doi.org/10.1029/2005RS003436>.
- Cloude, S.R. (2008). Polarization Coherence Tomography (PCT): A Tutorial Introduction (Manual). PolSARpro. ESA. [http://earth.eo.esa.int/polsarpro/Manuals/3\\_PCT\\_Training\\_Course.pdf](http://earth.eo.esa.int/polsarpro/Manuals/3_PCT_Training_Course.pdf). (accessed June 2014).

- Cloude, S.R., Papathanassiou, K.P. (1998). Polarimetric SAR interferometry. *IEEE Transactions on Geoscience and Remote Sensing* 36(5), 1551–1565. <http://dx.doi.org/10.1109/36.718859>.
- Cloude, S.R., Papathanassiou, K.P. (2003). Three-stage inversion process for Polarimetric SAR Interferometry. *IEE Proceedings- Radar, Sonar and Navigation*, 150(3), 125–134. <http://dx.doi.org/10.1049/ip-rsn:20030449>
- Cloude, S.R., Pottier, E. (1996). A review of target decomposition theorems in radar polarimetry. *IEEE Transactions on Geoscience and Remote Sensing*, 34(2), 498–518. [www.doi.org/10.1109/36.485127](http://www.doi.org/10.1109/36.485127).
- Colin-Koeniguer, E., Trouve, N. (2014). Performance of Building Height Estimation Using High-Resolution PolInSAR Images. *IEEE Transactions on Geoscience and Remote Sensing*, 52(9), 5870–5879. <http://dx.doi.org/10.1109/TGRS.2013.2293605>.
- Feng Xu, Ya-Qiu Jin. (2005). Deorientation theory of polarimetric scattering targets and application to terrain surface classification. *IEEE Transactions on Geoscience and Remote Sensing*, 43(10), 2351–2364. <http://dx.doi.org/10.1109/TGRS.2005.855064>.
- Freeman, A., Durden, S.L. (1998). A three-component scattering model for polarimetric SAR data. *IEEE Transactions Geoscience and Remote Sensing*, 36(3), 963–973. <http://dx.doi.org/10.1109/36.673687>.
- Frey, O., Meier, E., Hajnsek, I. (2012). Towards a more reliable estimation of forest parameters from polarimetric SAR tomography data, *2012 IEEE International Geoscience and Remote Sensing Symposium* (pp. 3110–3113). Germany: Munich. <http://dx.doi.org/10.1109/IGARSS.2012.6350767>.
- Hellmann, M.; Cloude, S.R. (2007). Polarimetric Interferometry. In *Radar Polarimetry and Interferometry* (pp. 8-1 – 8-14). Educational Notes, Paper-8. Neuilly-sur-Seine, France. <http://ftp.rta.nato.int/public/PubFullText/RTO/EN/RTO-EN-SET-081bis/EN-SET-081bis-08.pdf>. (accessed May, 2014).
- Huynen, J.R. (1970). Phenomenological Theory of Radar Targets (Doctoral Thesis). Technical University of Delft, The Netherlands.
- Jin, Y.-Q., Xu, F. (2013). *Polarimetric Scattering and SAR Information Retrieval*. Singapore: John Wiley-IEEE Press. ISBN: 978-1-118-18813-2.
- Khati, U., Kumar, S., Thakur, P. (2013). Effect of Shift in Polarization Orientation Angle on Multi-wavelength Fully Polarimetric Data, *ICMARS, 9<sup>th</sup> International Conference on Microwave, Antenna, Propagation and Remote Sensing* (pp. 30-34). India: Jodhpur.
- Kostinski, A., Boerner, W.-M. (1986). On foundations of radar polarimetry. *IEEE Transactions on Antennas and Propagation*. 34(12), 1395–1404. <http://dx.doi.org/10.1109/TAP.1986.1143771>.
- Krieger, G., Papathanassiou, K.P., Cloude, S.R. (2005). Spaceborne Polarimetric SAR Interferometry: Performance Analysis and Mission Concepts. *EURASIP Journal on Advances in Signal Processing*. 20, 3272–3292. <http://dx.doi.org/10.1155/ASP.2005.3272>.

- Lee, J.-S., Ainsworth, T.L. (2011). The Effect of Orientation Angle Compensation on Coherency Matrix and Polarimetric Target Decompositions. *IEEE Transactions on Geoscience and Remote Sensing*. 49(1), 53–64. <http://dx.doi.org/10.1109/TGRS.2010.2048333>.
- Lee, J.-S., Pottier, E. (2009). *Polarimetric Radar Imaging: From Basics to Applications*. Florida: CRC Press. ISBN 9781420054972.
- Lee, J.-S., Schuler, D.L., Ainsworth, T.L. (2000). Polarimetric SAR data compensation for terrain azimuth slope variation. *IEEE Transactions on Geoscience and Remote Sensing*. 38(5), 2153–2163. <http://dx.doi.org/10.1109/36.868874>.
- Lee, J.-S., Schuler, D.L., Ainsworth, T.L., Krogager, E., Kasilingam, D., Boerner, W.-M. (2002). On the estimation of radar polarization orientation shifts induced by terrain slopes. *IEEE Transactions on Geoscience and Remote Sensing* 40(1), 30–41. <http://dx.doi.org/10.1109/36.981347>.
- Lee, S.-K. (2012). Forest parameter estimation using Polarimetric SAR Interferometry techniques at low frequencies (PhD. Thesis). Eidgenössische Technische Hochschule, ETH Zürich, Oberpfaffenhofen.
- Lee, S.K., Kugler, F., Papathanassiou, K.P., Moreira, A. (2006). Forest Height Estimation by means of Pol-InSAR. *Kyoto & Carbon Science Report - Phase 1 (2006-2008) pp. 1-13*. [http://www.eorc.jaxa.jp/ALOS/en/kyoto/phase\\_1/KC-Phase1-report\\_DLR\\_v2.pdf](http://www.eorc.jaxa.jp/ALOS/en/kyoto/phase_1/KC-Phase1-report_DLR_v2.pdf). (accessed June, 2014).
- Li, Z., Guo, M., Wang, Z., Zhao, L. (2014). Forest-height inversion using repeat-pass spaceborne polInSAR data. *Science China: Earth Sciences*. 57(6), 1314-1324. <http://dx.doi.org/10.1007/s11430-013-4669-3>.
- Lopez-Martinez, C., Alonso-Gonzalez, A. (2014). Assessment and Estimation of the RVoG Model in Polarimetric SAR Interferometry. *IEEE Transactions on Geoscience and Remote Sensing*. 52(6), 3091–3106. <http://dx.doi.org/10.1109/TGRS.2013.2269614>
- Lopez-Martinez, C., Fabregas, X., Pipia, L. (2009). PolSAR and PolInSAR model based information estimation. *2009 IEEE International Geoscience and Remote Sensing Symposium* (pp. III–959 – III-962). South Africa: Cape Town. <http://dx.doi.org/10.1109/IGARSS.2009.5417934>.
- Lopez-Martinez, C., Papathanassiou, K.P. (2013). Cancellation of Scattering Mechanisms in PolInSAR: Application to Underlying Topography Estimation. *IEEE Transactions on Geoscience and Remote Sensing*. 51(2), 953–965. <http://dx.doi.org/10.1109/TGRS.2012.2205157>.
- Lopez-Sanchez, J.M., Ballester-Berman, J.D. (2009). Potentials of polarimetric SAR interferometry for agriculture monitoring. *Radio Science*. 44(2), RS2010, 1 – 20. <http://dx.doi.org/10.1029/2008RS004078>.
- Lopez-Sanchez, J.M., Hajnsek, I., Ballester-Berman, J.D. (2012). First Demonstration of Agriculture Height Retrieval with PolInSAR Airborne Data. *IEEE Geoscience and Remote Sensing Letters* 9(2), 242–246. <http://dx.doi.org/10.1109/LGRS.2011.2165272>.
- Luo, H.-M., Chen, E., Cheng, J., Li, X. (2010). Tree height retrieval methods using POLInSAR coherence optimization. *2010 IEEE International Geoscience and Remote Sensing*

- Symposium.* (pp. 3259–3262). USA: Honolulu.  
<http://dx.doi.org/10.1109/IGARSS.2010.5649765>.
- Mette, T. (2006). Forest Biomass Estimation from Polarimetric SAR Interferometry (Doctoral Thesis). Technical University of Munich, Munich.
- Mette, T., Papathanassiou, K., Hajnsek, I. (2004). Biomass estimation from polarimetric SAR interferometry over heterogeneous forest terrain. *2004 IEEE International Geoscience and Remote Sensing Symposium* (pp. 511–514). USA: Anchorage.  
<http://dx.doi.org/10.1109/IGARSS.2004.1369076>.
- Minh, N.P., Zou, B. (2013). A Novel Algorithm for Forest Height Estimation from PolInSAR Image. *International Journal of Signal Processing, Image Processing & Pattern Recognition*. 6(2) 15 - 32.
- Minh, N.P., Zou, B., Lu, D. (2012). Accuracy improvement method of forest height estimation for PolInSAR Image. *ICALIP, International Conference on Audio, Language and Image Processing*. (pp. 594–598). China: Shanghai.
- Neumann, M., Ferro-Famil, L., Reigber, A. (2010). Estimation of Forest Structure, Ground, and Canopy Layer Characteristics from Multibaseline Polarimetric Interferometric SAR Data. *IEEE Transactions on Geoscience and Remote Sensing*. 48(3), 1086–1104.  
<http://dx.doi.org/10.1109/TGRS.2009.2031101>.
- Nghia, P.M., Zou, B., Cheng, Y. (2012). Forest height estimation from PolInSAR image using adaptive decomposition method. *ICSP, 11th International Conference on Signal Processing*. (pp. 1830–1834). China: Beijing.
- Papathanassiou, K.P., Cloude, S.R. (2001). Single-baseline polarimetric SAR interferometry. *IEEE Transactions on Geoscience and Remote Sensing* 39(11), 2352–2363.  
<http://dx.doi.org/10.1109/36.964971>.
- Richards, J.A. (2009). *Remote Sensing with Imaging Radar*. Heidelberg: Springer. ISBN 978-3-642-02020-9.
- Schuler, D.L., Lee, J.-S., De Grandi, G. (1996). Measurement of topography using polarimetric SAR images. *IEEE Transactions on Geoscience and Remote Sensing* 34(5), 1266–1277.  
<http://dx.doi.org/10.1109/36.536542>.
- Skolnik, M. (3<sup>rd</sup> Eds). (2008). *Radar Handbook*, New York: McGraw-Hill. ISBN 978-0071485470.
- Skolnik, M.I. (2003). *Introduction to Radar Systems*. Tata McGraw-Hill Education. ISBN 978-0072881387.
- Tan, L., Yang, R. (2008). Investigation on tree height retrieval with polarimetric SAR interferometry. *2004 IEEE International Geoscience and Remote Sensing Symposium* (pp. V–546 – V-549). USA: Boston. <http://dx.doi.org/10.1109/IGARSS.2008.4780150>.
- Tebaldini, S. (2010). Single and Multipolarimetric SAR Tomography of Forested Areas: A Parametric Approach. *IEEE Transactions on Geoscience and Remote Sensing*. 48(5), 2375–2387. <http://dx.doi.org/10.1109/TGRS.2009.2037748>.
- Treuhaft, R., Madsen, S., Moghaddam, M., Van Zyl, J.J. (1996). Vegetation characteristics and underlying topography from interferometric radar. *Radio Science*. 31(6), 1449–1485.  
<http://dx.doi.org/10.1029/96RS01763>.

- Ulaby, F., Fung, A., Moore, R. (1986). *Microwave Remote Sensing Active and Passive. From Theory to Applications*. Chicago: Artech House.
- Ulaby, F.T., Moore, R.K., Fung, A.K. (1982). *Microwave Remote Sensing: Active and Passive. Radar Remote Sensing and Surface Scattering and Emission Theory*. Chicago : Artech House.
- Ulaby, F.T., Moore, R.K., Fung, A.K. (1981). *Microwave Remote Sensing: Active and Passive. Microwave Remote Sensing Fundamentals and Radiometry*. Chicago: Artech House.
- Wang, H., Ouchi, K. (2010). A Simple Moment Method of Forest Biomass Estimation From Non-Gaussian Texture Information by High-Resolution Polarimetric SAR. *IEEE Geoscience and Remote Sensing Letters*. 7(4), 811–815. <http://dx.doi.org/10.1109/LGRS.2010.2047839>
- Woodhouse, I. (2006). *Introduction to Microwave Remote Sensing* (Chapter 4). Florida: CRC Press. ISBN 0-415-27123-1.
- Yamaguchi, Y., Moriyama, T., Ishido, M., Yamada, H. (2005). Four-component scattering model for polarimetric SAR image decomposition. *IEEE Transactions on Geoscience and Remote Sensing*. 43(8), 1699–1706. <http://dx.doi.org/10.1109/TGRS.2005.852084>.
- Yamaguchi, Y., Sato, A., Boerner, W.-M., Sato, R., Yamada, H. (2011). Four-Component Scattering Power Decomposition with Rotation of Coherency Matrix. *IEEE Transactions on Geoscience and Remote Sensing*. 49(6), 2251–2258. <http://dx.doi.org/10.1109/TGRS.2010.2099124>.
- Yamaguchi, Y., Yajima, Y., Yamada, H. (2006). A Four-Component Decomposition of POLSAR Images Based on the Coherency Matrix. *IEEE Geoscience and Remote Sensing Letters*. 3(3), 292–296. <http://dx.doi.org/10.1109/LGRS.2006.869986>.
- Yong Bian, Mercer, B. (2010). PolInSAR Statistical Analysis and Coherence Optimization Using Fractional Lower Order Statistics. *IEEE Geoscience and Remote Sensing Letters*. 7(2), 314–318. <http://dx.doi.org/10.1109/LGRS.2009.2034275>.
- Zhang, Q., Mercer, B., Cloude, S.R. (2008). Forest height estimation from INDREX-II L-band polarimetric InSAR data. *Proceedings of the ISPRS XXIth Congress*. (pp. 343 – 348). China: Beijing.
- Zou, B., Cai, H., Zhang, Y., Lin, M. (2013). Building Parameters Extraction from Spaceborne PolInSAR Image Using a Built-Up Area Scattering Model. *IEEE Journal of Selected Topics in Applied Earth Observations and Remote Sensing*. 6(1), 162–170. <http://dx.doi.org/10.1109/JSTARS.2012.2210033>.
- Zou, B., Lu, D., Hongjun, C., Zhang, Y. (2011). Ground topography estimation over forests using PolInSAR image by means of coherence set. *ICIP 18<sup>th</sup> IEEE International Conference on Image Processing* (pp. 2809–2812). Belgium: Brussels. <http://dx.doi.org/10.1109/ICIP.2011.6116621>.

## APPENDICES

### Appendix 1: Plot wise Field Measured Tree Height

Table A1.0.1 Plot wise field measured tree height

Sr No	Latitude	Longitude	Field measured average plot height H_avg (m)
1	30.12714	78.25838	21
2	30.12591	78.25545	23
3	30.12571	78.25219	25
4	30.12482	78.24848	18.9
5	30.124	78.24399	22.9
6	30.12352	78.24239	28
7	30.12324	78.21408	21.1
8	30.11462	78.21178	28
9	30.11833	78.21266	26
10	30.11624	78.21386	25
11	30.11104	78.21126	24
12	30.11203	78.2173	24
13	30.11513	78.22126	25
14	30.11762	78.22585	27
15	30.1147	78.23486	23
16	30.09903	78.24655	21
17	30.16393	78.22347	24
18	30.16732	78.1899	22
19	30.12172	78.17496	21
20	30.12922	78.17127	15
21	30.12954	78.17359	21
22	30.09192	78.19826	27
23	30.08774	78.20958	24
24	30.10013	78.21136	21
25	30.16532	78.23998	24
26	30.16502	78.24088	25
27	30.15431	78.24398	28
28	30.14183	78.24697	20
29	30.1415	78.2462	24
30	30.13442	78.25039	24
31	30.12912	78.25785	21
32	30.16201	78.21787	21

<b>Sr No</b>	<b>Latitude</b>	<b>Longitude</b>	<b>Field measured average plot height H_avg</b>
33	30.10421	78.17825	25
34	30.20603	78.16357	26
35	30.20782	78.16715	22
36	30.20983	78.16849	25
37	30.2148	78.18149	23
38	30.2188	78.18719	22
39	30.21921	78.19969	29
40	30.21432	78.20336	27
41	30.23772	78.15269	23
42	30.23551	78.15275	18
43	30.22994	78.15156	23
44	30.22433	78.1551	28
45	30.22454	78.1687	28
46	30.22583	78.17629	24
47	30.23333	78.18968	24
48	30.22284	78.19886	24
49	30.24042	78.17935	26.8
50	30.24403	78.17946	25.2
51	30.24894	78.18358	27.6
52	30.25234	78.18878	23.4
53	30.24553	78.195	25
54	30.2425	78.19467	23.6
55	30.23784	78.18348	24.3
56	30.20474	78.16459	24.6
57	30.20611	78.19435	22
58	30.15704	78.23228	23
59	30.15261	78.23198	18
60	30.1488	78.23105	24
61	30.14113	78.22867	27
62	30.14103	78.22826	24
63	30.13574	78.22758	27
64	30.11084	78.21028	21.8
65	30.11071	78.20815	28
66	30.1127	78.21297	23
67	30.11751	78.22498	20.5
68	30.12302	78.22928	22.2
69	30.13123	78.22755	23.4

<b>Sr No</b>	<b>Latitude</b>	<b>Longitude</b>	<b>Field measured average plot height H_avg</b>
70	30.09361	78.1867	25.6
71	30.16112	78.24187	28
72	30.17082	78.23568	23.9
73	30.16372	78.23468	20
74	30.15941	78.22095	20.3
75	30.12654	78.25979	24.3
76	30.11681	78.23418	21.3
77	30.10572	78.23869	27.8
78	30.10163	78.24788	22.5
79	30.10671	78.20018	23
80	30.10752	78.19185	28.5
81	30.1703	78.18826	21.8
82	30.1644	78.19066	16.6
83	30.11653	78.27688	21.4
84	30.10534	78.2637	18.5
85	30.10132	78.27216	24.6
86	30.10164	78.27438	21
87	30.11964	78.27269	23.9
88	30.11433	78.21288	18
89	30.11844	78.21349	18.7
90	30.12323	78.24157	21
91	30.08834	78.20588	20
92	30.09462	78.19186	21.5
93	30.10262	78.19469	25
94	30.09642	78.19139	22
95	30.0997	78.19109	23.5
96	30.12962	78.1877	24.3
97	30.1191	78.19365	25.7
98	30.14	78.17158	25.6
99	30.09393	78.15568	20.5
100	30.10421	78.17198	25

## Appendix 2: ‘Three Stage Inversion’ technique

This section explains the ‘Three Stage Inversion’ technique for forest height estimation using PolInSAR data. The technique explained below is a part of the original technique by Cloude and Papathanassiou (S. R. Cloude and K. P. Papathanassiou, 2003).

The basic observable in PolInSAR is the 6x6 coherence matrix defined in (Eq. A2.1). The complex coherence  $\gamma$  can be represented as shown in (Eq. A2.2)

$$[T_6] = \langle k, k^{*T} \rangle = \begin{bmatrix} T_{11} & \Omega_{12} \\ \Omega_{12}^{*T} & T_{22} \end{bmatrix} \quad (\text{A2.1})$$

$$\text{Where, } k = \frac{1}{\sqrt{2}} [S_{HH}^1 + S_{VV}^1 \quad S_{HH}^1 - S_{VV}^1 \quad 2S_{HV}^1 \quad S_{HH}^2 + S_{VV}^2 \quad S_{HH}^2 - S_{VV}^2 \quad 2S_{HV}^2]$$

$$\gamma = \frac{\omega^{*T} \Omega_{12} \omega}{\omega^{*T} T_{11} \omega} \quad (\text{A2.2})$$

In Eq. A2.2,  $\omega$  is a three component unitary complex vector defining the choice of polarization. The ‘Three Stage Inversion’ technique assumes the two-layer model for vegetation developed by (Treuhaft *et al.*, 1996). A schematic representation for the two layer model is shown in Figure A2.1. The ground is at an elevation of  $z=0$ . The vegetation canopy layer with height  $h_v$  has the bounds  $z=z_0$  to  $z=z_0+h_v$ . The model has two layers – the bottom layer and the top layer.

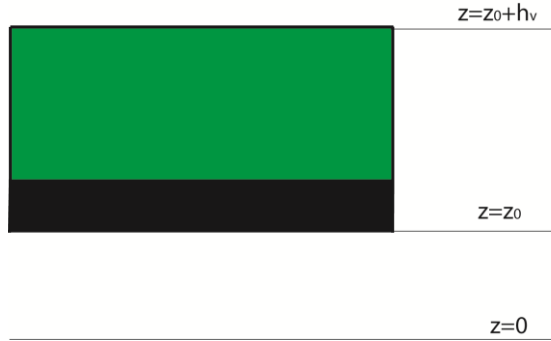


Figure A2.1 Schematic representation of the two layer model.

According to the two-layer model for vegetation, the equation for complex coherence  $\gamma$  can be rewritten as

$$\gamma = \frac{\omega^{*T} (e^{i\phi_1} I_2^V + e^{\frac{-2\sigma h_v}{\cos \theta_0}} T_g e^{i\phi_1}) \omega}{\omega^{*T} (I_1^V + e^{\frac{-2\sigma h_v}{\cos \theta_0}} T_g) \omega} \quad (\text{A2.3})$$

Where,

$$I_1^V = e^{\frac{-2\sigma h_v}{\cos \theta}} \int_0^{h_v} e^{\frac{2\sigma z'}{\cos \theta_0}} T_V dz'$$

$$I_2^V = e^{\frac{-2\sigma h_v}{\cos \theta}} \int_0^{h_v} e^{\frac{2\sigma z'}{\cos \theta_0}} e^{ik_{zz'}} T_V dz'$$

$$T_V = m_v \begin{bmatrix} 1 & 0 & 0 \\ 0 & \mu & 0 \\ 0 & 0 & \mu \end{bmatrix} \quad 0 \leq \mu \leq 0.5$$

$$T_g = m_g \begin{bmatrix} 1 & t_{12} & 0 \\ t_{12}^* & t_{22} & 0 \\ 0 & 0 & t_{33} \end{bmatrix} \quad (\text{A2.4})$$

In Eq. A2.3 and Eq. A2.4,  $\phi_1$  is the phase center of the bottom layer,  $\sigma$  is the mean wave extinction in the medium,  $k_z$  is the vertical wavenumber,  $\theta$  is the mean angle of incidence,  $T_V$  is 3x3 diagonal coherence matrix for the volume scattering and  $T_g$  is the reflection symmetric ground scattering coherence matrix,  $\mu$  is the ground-to-volume scattering ratio.

The model assumes that the canopy extends from ground to top and hence  $\phi_1 = \phi_2$ . The complex coherence is polarization dependent and can be rewritten as the equation of a straight line in the complex plane as

$$\gamma(\omega) = e^{i\phi_1}(\gamma_v + L(\omega)(1 - \gamma_v)) \quad 0 \leq L(\omega) \leq 1 \quad (\text{A2.5})$$

Where

$$L(\omega) = \frac{\mu(\omega)}{1+\mu(\omega)} \quad \text{and} \quad \mu(\omega) = \frac{2\sigma}{\cos\theta_0(e^{\frac{2\sigma h_v}{\cos\theta_0}} - 1)} \frac{\omega^{*T} T_g \omega}{\omega^{*T} T_V \omega} \quad (\text{A2.6})$$

$$\gamma_v = \frac{2\sigma}{\cos\theta_0(e^{\frac{2\sigma h_v}{\cos\theta_0}} - 1)} \int_0^{h_v} e^{ik_z z'} e^{2\sigma z' / \cos\theta_0} dz' \quad (\text{A2.7})$$

The ground-to-volume scattering ratio  $\mu(\omega)$  is polarization dependent and includes the effects of wave extinction in the medium as seen in Eq. A2.6 and  $\gamma_v$  is a polarization-independent volume integral shown in Eq. A2.7. The inversion of (A2.5) can be easily understood by employing a geometrical interpretation inside a unit circle of the complex plane as shown in Figure A2.2.

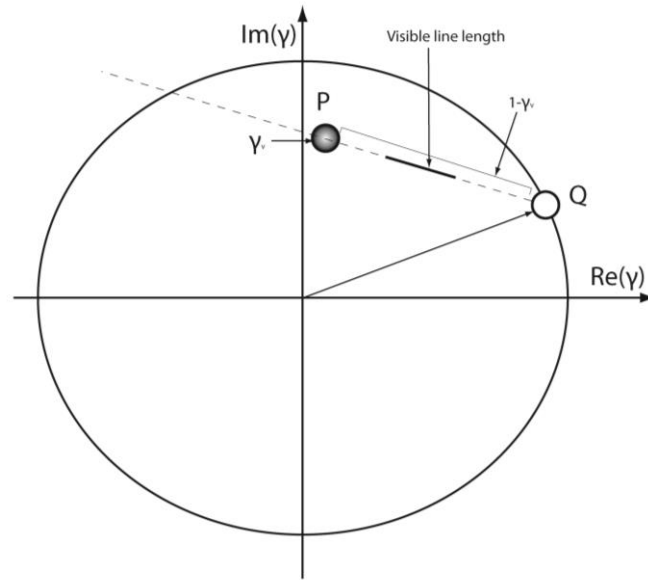


Figure A2.2 Representation of the 'Three Stage Inversion' technique (Cloude and Papathanassiou, 2003).

Eq. A2.6 is plotted on the complex plane. The line intersects the circle at two points. One of these is the underlying topography related phase (shown as Q in Figure A2.2). The other is a false solution and must be rejected by the inversion process.

The volume coherence  $\gamma_v$  lies at one end of the line. It satisfies the condition  $\mu = 0$  and is represented as P in Figure A2.2. This point provides the estimation of height using this technique. The visible length of the line depends on the baseline, operating frequency and vegetation density. The PolInSAR model inversion is carried out in three stages as described below.

**Stage 1: Least Squares line fit**

The complex coherences in all the possible polarizations are plotted on the complex plane as shown in Figure A2.3. A best fit line is plotted using the real and imaginary components of the data and the equation of the best fit line is calculated. Using this equation, the intersection of the line with the complex plane are calculated. Let these intersection points be  $\psi_1$  and  $\psi_2$ . One of these two points represents the true ground phase. The correct point is estimated through the process of vegetation bias removal.

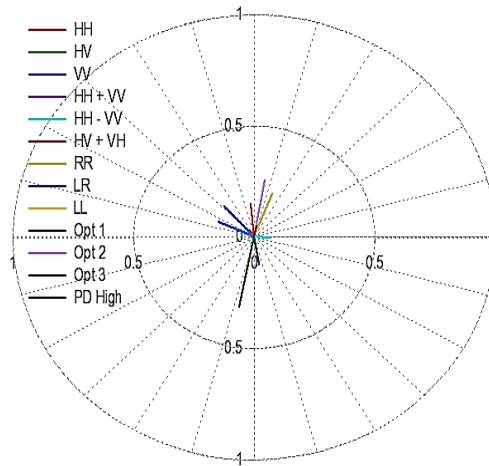


Figure A2.3 An example of the coherences plotted on the complex plane.

**Stage 2: Vegetation bias removal**

In the second stage, the correct intersection point among  $\psi_1$  and  $\psi_2$  needs to be selected. A simple strategy is applied in this stage. The ground-to-volume scattering ratio  $\mu$  is low for the polarizations which have more volume scattering and lower for those having dominant surface scattering. The polarizations are rank-ordered according to the estimated ground-to-volume scattering ratio, and the intersection point which lies farthest is the correct estimate for ground topography. For eg. HV polarization will have more volume scattering and hence low ground-to-volume scattering ratio. The intersection point among  $\psi_1$  and  $\psi_2$  which is farthest from the  $\gamma_{HV}$  coherence provides a correct estimate of the ground topography.

**Stage 3: Height and extinction estimation**

Using Eq. A2.7, a function is plotted at a fixed mean wave extinction  $\sigma$ , which provides a relation between complex coherence and height of vegetation layer  $h_v$ . Such curves at difference values of  $\sigma$  are plotted on the unit circle as shown in Figure A2.4.

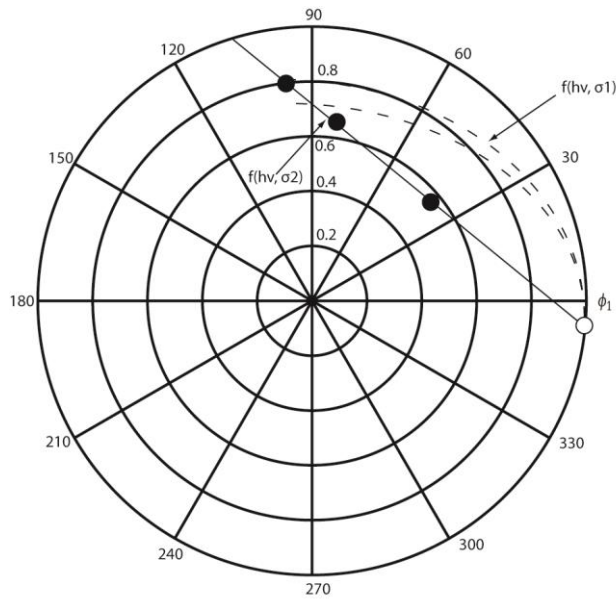


Figure A2.4 Geometrical interpretation of the height and extinction estimation (Cloude and Papathanassiou, 2003).

Where the curve intersects the line the candidate  $\gamma_v$  point. The value of  $\mu$  for each point is calculated. One of the points has a negative value for  $\mu$  which is not physically possible and the point is eliminated. This we obtain the estimate for the correct  $\gamma_v$ . Using the Eq. A2.7, the height of the vegetation layer  $h_v$  is estimated assuming a suitable value for the mean wave extinction  $\sigma$ . This is the mathematical basis behind the ‘Three Stage Inversion’ technique. Readers are referred to (S. R. Cloude and K. P. Papathanassiou, 2003) for more detailed explanation of the process.

### Appendix 3: Effect of POA Shift on PolInSAR data

A preliminary study was carried out to assess the effect of POA Shift (OAS) on PolInSAR data. As discussed in Sec. 4.1.2, the shift in orientation angle in the two acquisitions of the PolInSAR data are calculated and the scattering matrices  $[S_1]$  and  $[S_2]$  are compensated for the shift using (4.3). The scattering matrices  $[\overline{S}_1]$  and  $[\overline{S}_2]$  are generated post-compensation and the 6x6 complex coherence matrix  $[\overline{T}_6]$  is calculated. The complex coherences in different polarizations are calculated, and forest stand height using ‘Three Stage Inversion’ technique is estimated. This section provides the changes observed in the coherence pattern post-compensation and analyses the change in estimation of forest stand height after compensating for orientation angle shift.

### A3.1 Effect on Complex Coherences in different Polarization basis

Change in the coherence pattern was observed post-compensation. The Figure A3.1 shows the comparative coherence maps in Linear basis, pre- and post-OAS compensation.

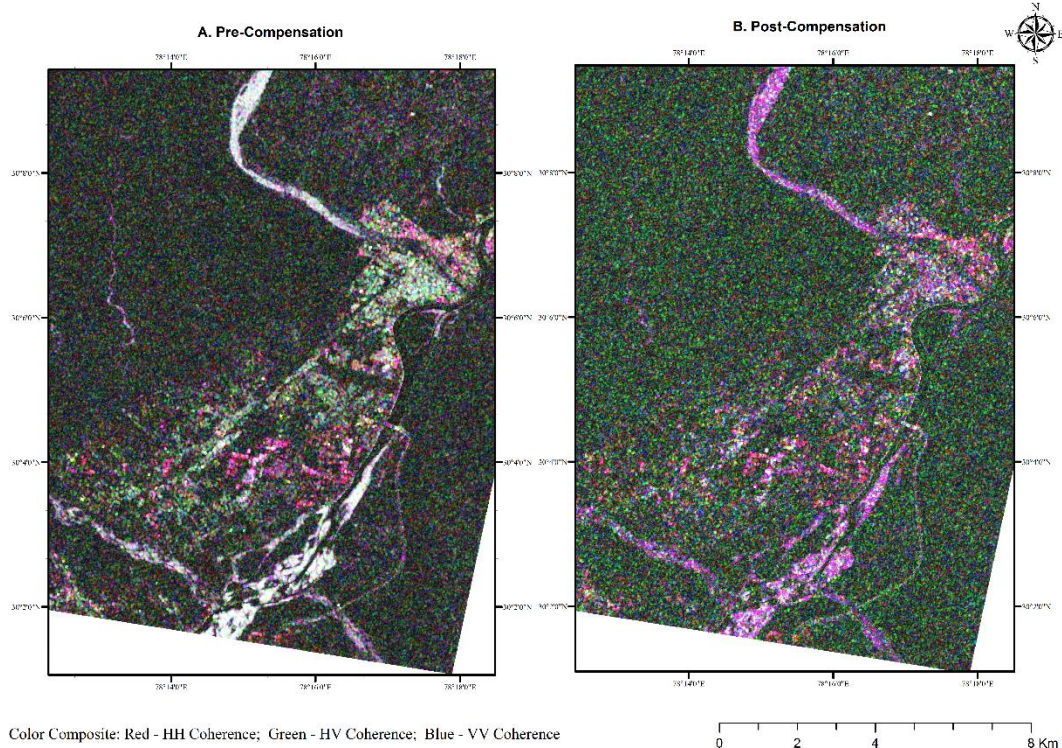


Figure A3.1 Comparative color composite Coherence map in Linear (H,V) polarization basis. A. Shows coherence map pre-OAS compensation and B. shows coherence map post-OAS compensation. The color composition is Red-HH coherence; Green-HV coherence and Blue-VV coherence.

Similarly, complex coherences were calculated in Pauli and Circular basis. The comparative maps are shown in Figure A3.2 and Figure A3.3.

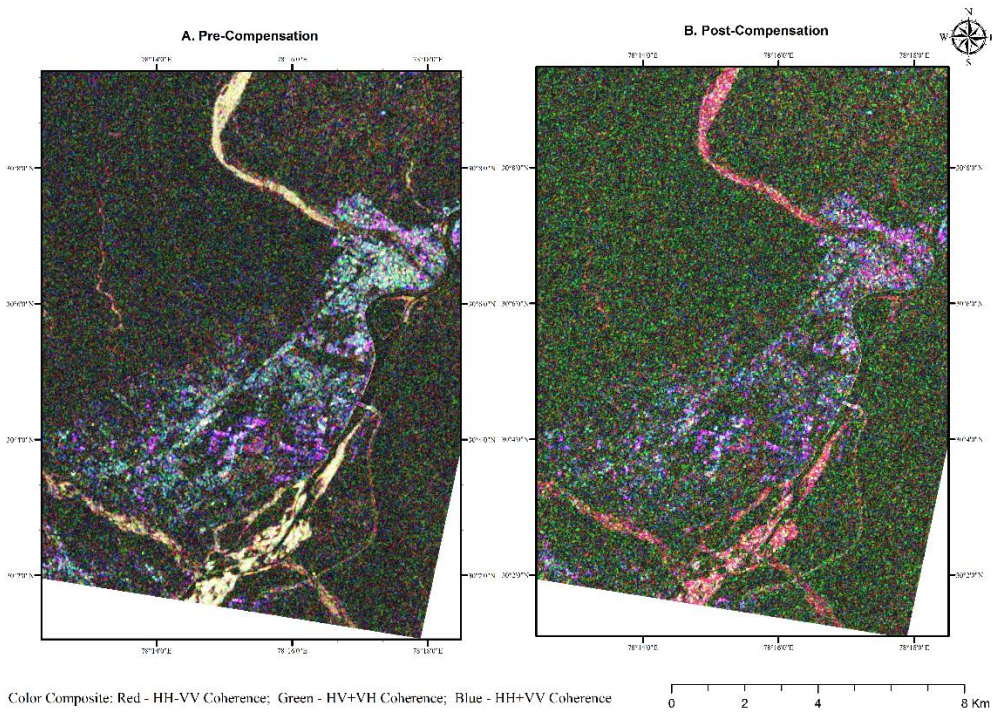


Figure A3.2 Comparative color composite Coherence map in Pauli polarization basis. A. Shows coherence map pre-OAS compensation and B. shows coherence map post-OAS compensation. The color composition is Red-HH+VV coherence; Green-HV+VH coherence and Blue-HH+VV coherence.

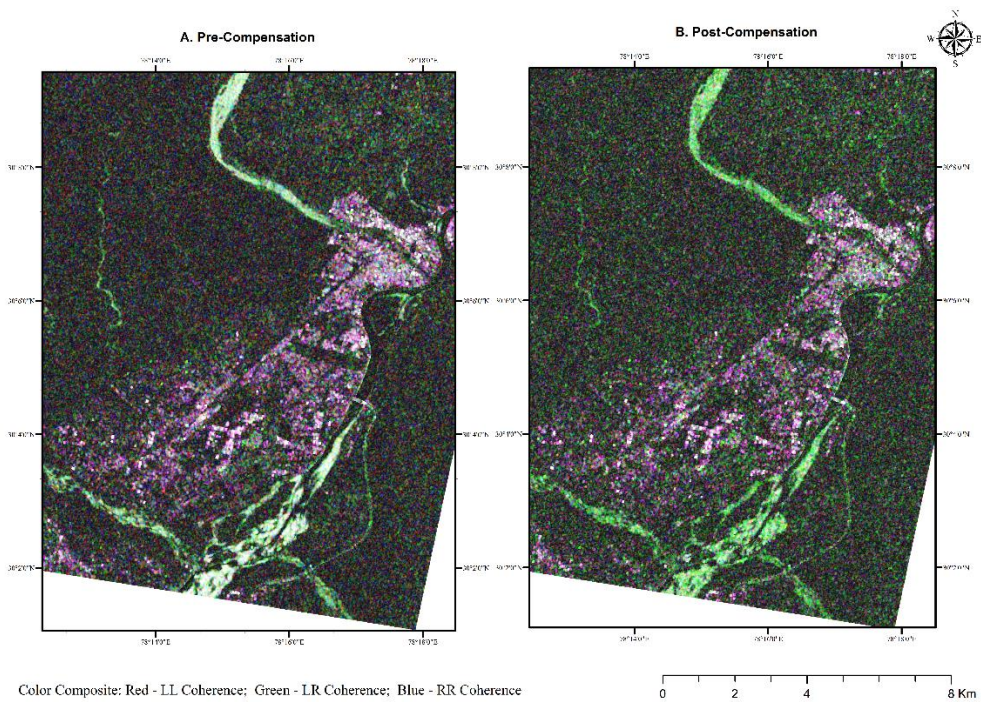


Figure A3.3 Comparative color composite Coherence map in Circular (L,R) polarization basis. A. Shows coherence map pre-OAS compensation and B. shows coherence map post-OAS compensation. The color composition is Red-LL coherence; Green-LR coherence and Blue-RR coherence.

The changes in coherence pattern in three polarization basis are shown in Figure A3.1, Figure and Figure . The observed changes in three major regions – forests, dry riverbed and urban areas – are tabulated in Table A3.1.

Table A3.1 Change in Coherence pattern post compensation for OAS.

Change Observed	Forest regions	Dry Riverbed	Urban areas
Linear basis (HH, HV, VV)	Increase in cross-polarized (HV) coherence. This shows presence of permanent cross-polarized scatterers in the forest regions. This is expected since forests act as cross-polarized scatterers.	Increase in HH- coherence and decrease in HV- and VV- coherence. The white color in dry riverbed pre-compensation denotes presence of all three coherences in equal proportions. This suggests that the dry riverbed scatterers in all three polarization. This is due to presence of stones which lead to both double-bounce and volume scattering besides surface scattering due to the fine sand in the river bed. Post-compensation, the HH-coherence increases and HV- and VV-coherence decreases. The increase in HH-coherence suggests presence of scatterers which lead to higher surface scattering.	Urban areas show decrease in HV-coherence and increase in HH- and VV-coherence. The HH- and VV-coherence increase when scatterers lead to more surface and double-bounce scattering. In urban regions, these two scattering is dominant and volume scattering is minimum. Hence decrease in HV-coherence is expected and provides more accurate coherence estimation.
Pauli basis (HH+VV, HV+VH, HH-VV)	Show a similar trend as observed in Linear basis. The HV+VH-coherence increases. This suggests increase in detection of volume scatterers.	The HH-VV coherence increases in dry riverbed regions. This suggests that the double-bounce scatterers are present in riverbed in large numbers as compared to surface and volume scatterers. This is true as the dry bed is strewn with stones (see Figure ).	The HV+VH coherence decreases and the HH-VV and HH+VV coherence increases. This suggests detection of higher number of double-bounce and surface scatterers as compared to the volume scatterers. Stable scatterers lead to high coherence.
Circular basis (LL, LR, RR)	The forests show very small increase in cross-polarized LR coherence as compared to Linear and Pauli basis.	The LR coherence increases in dry riverbed region. This suggests presence of stable scatterers which lead to cross-polarized scattering.	The urban regions show very less change after compensation for OAS.

From the observations noted in Table A3.1, it is observed that the deorientation or the compensation for POA shift result in increase of detected scatterers with expected scattering behavior post-compensation for the particular region. For example, in the Pauli basis coherence, in the dry riverbed the HH-VV coherence increases after deorientation. It is well known that HH-VV scattering increases when double-bounce scattering increases. However, HH-VV coherence will increase when stable scatterers are present which lead to double-bounce scattering. In the dry

bed, the stones may lead to double bounce scattering. Field photographs can be seen in Figure which shows the size of stones strewn across a dry riverbed. In the urban centers, HV+VH coherence decreases and HH-VV and HH+VV coherence increases. This shows that, before deorientation, the scatterers were incorrectly classified as those leading to volume scattering. After deorientation, the stable scatterers which provide high surface and double-bounce scattering lead to increase in HH-VV and HH+VV coherence. This is expected because the surfaces such as roof-top and roads act as stable surface scatterers increasing HH+VV coherence and the walls and the ground form a dihedral surface which is a stable double-bounce scattering surface. This increases the HH-VV coherence.



Figure A3.4 Field photographs of dry riverbed. The figure on the left shows the boulders in the riverbed. On the right the dry riverbed is seen in the backdrop of the foothills of the Himalayas.

An attempt has been made here to analyze the effects of POA shift compensation on the coherence in different polarization basis. A detailed mathematical analysis is beyond the scope of this thesis.

### **A3.2 Effect of deorientation on estimated forest height**

The ‘‘Three Stage Inversion’ technique’ for forest stand height estimation was applied to the de-oriented (POA Compensated) PolInSAR data. The forest stand height was estimated for the Barkot and Thano forest ranges. The retrieved forest height is validated and the accuracy estimated using the 100 field plots. The results obtained are presented.

Table A3.2 Descriptive Statistics - Forest height estimated pre- and post-deorientation

Statistic	Derived Height Post-Deorientation	Derived Height Pre-Deorientation	Field Height (H_avg)
Minimum	21 m	18 m	15 m
Mean	24.4 m	22.98 m	23.44 m
Maximum	27 m	27 m	29 m
Standard Deviation	1.39	2.122	2.87
Skewness	-0.335	-0.4	-0.277
Kurtosis	-0.112	-0.563	-0.078

Table A3.2 provides the basic descriptive statistics of the derived forest height after compensating for POA shift. The statistics for derived forest height before deorientation and the field height are also shown for comparison. It is observed that the estimated height increases after deorientation. However, this does not give a clear picture to the effect of POA shift compensation on the estimated height. The accuracy of the derived forest height is measured and the results are presented in Table A3.3.

Table A3.3 Accuracy assessment for derived forest height after deorientation

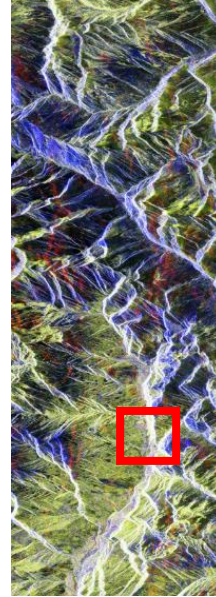
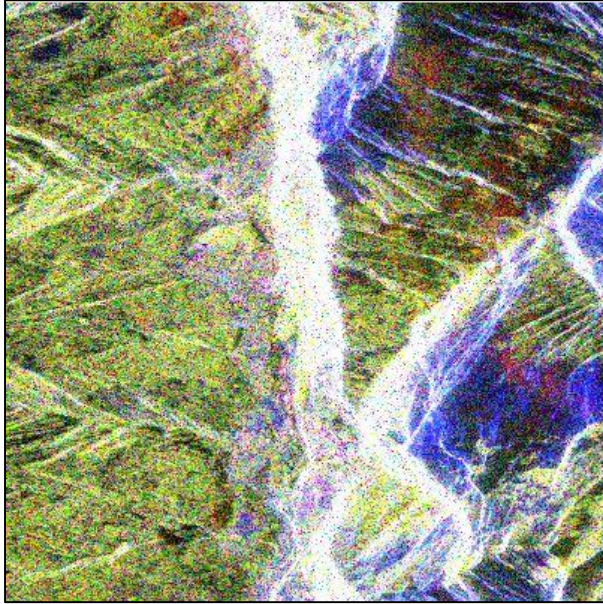
'Three Stage Inversion' technique	Mean height	Variance	RMSE	Correlation	Average Accuracy
Before Deorientation	23 m	4.505	2.28 m	0.62	91.56 %
After Deorientation	24.4 m	1.919	3.43 m	-0.12	87.94 %

It is observed that the deorientation has a very adverse effect on the estimated height using 'Three Stage Inversion' technique. The correlation after deorientation becomes -0.12. This shows negligible correlation between the derived and actual forest height. The reason for the loss in correlation and accuracy need to be ascertained in a detailed mathematical analysis which is beyond the scope of this work.

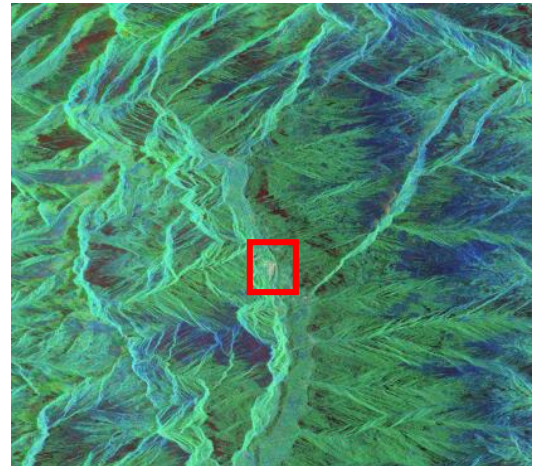
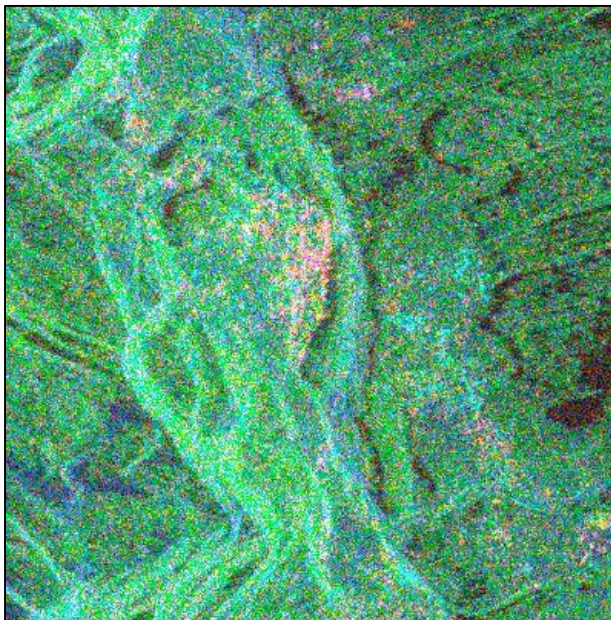
However it is observed that the POA shift compensation is not advised for PolInSAR based tree height estimation.

#### **Appendix 4: Pauli Decomposed images of Multi-frequency PolSAR data**

Figure A4.1 shows the Pauli decomposed images for the three PolSAR acquisitions over Manali for L-, C- and X-band. The blue color depicts surface scattering, red represents double-bounce scattering and greens stands for volume scattering.



I. ALOS PALSAR



II. RADARSAT-2

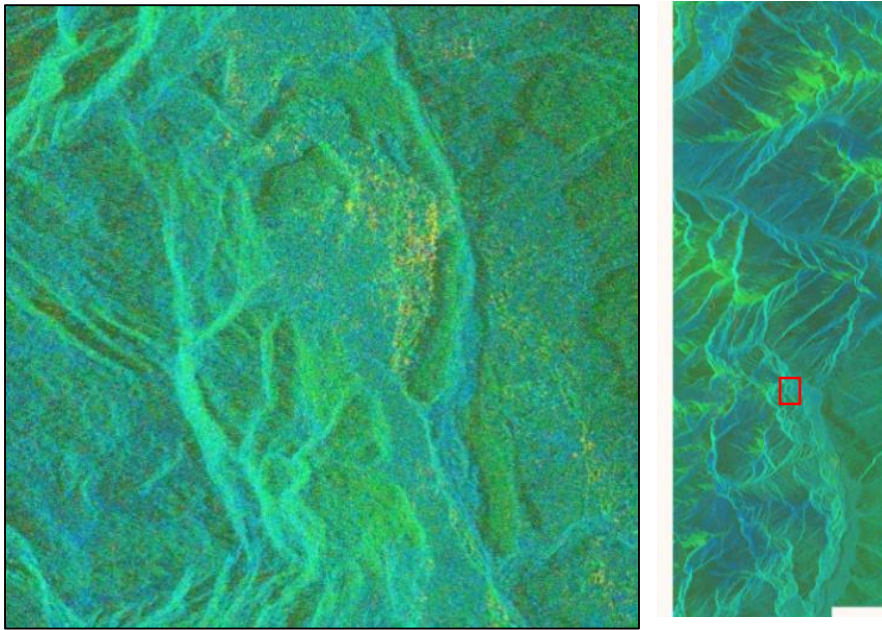


Figure A4.1 Pauli Decomposed Color Composite SAR images in L-, C-, and X-band. III. TERRASAR-X

The different resolutions of the acquired data can be readily observed from the level of detail of different features in the three images in Figure A4.1.

## **Appendix 5: Three Dimensional View of Estimated Height**

The three dimensional view of the estimated forest height using PolInSAR data are presented in this appendix. Figure A5.1 shows a 3D view of the Barkot forest and Rishikesh city. The dark blue color depicts near zero vegetation height. The urban areas and the dry-river bed are seen in this color. The Barkot forest with the variations in height can be seen.

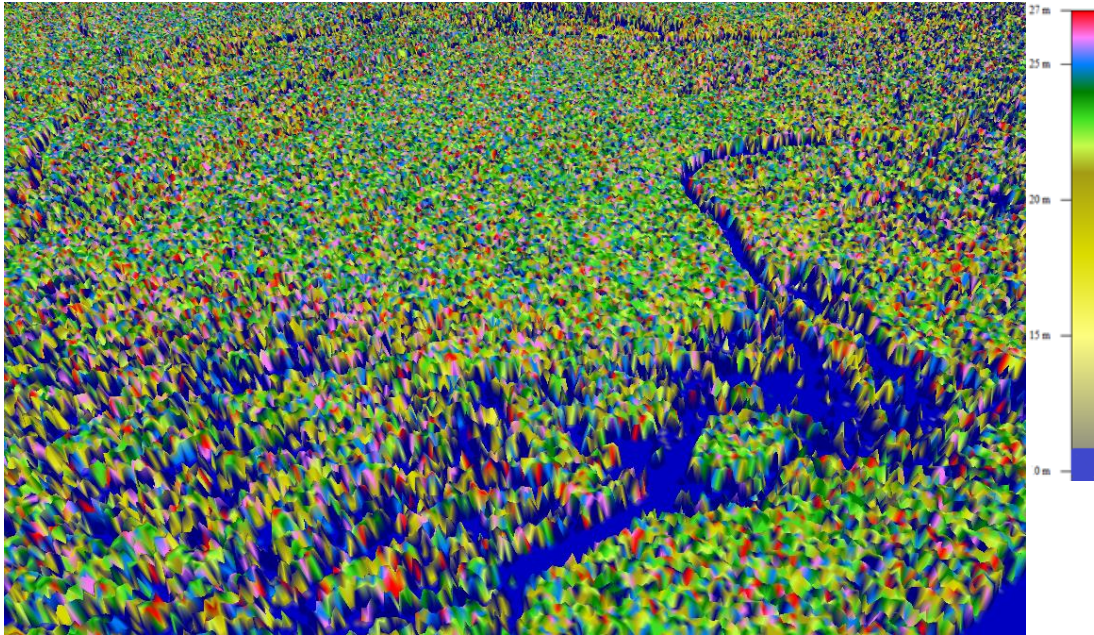


Figure A5.1 3D representation of Forest Height.

The SRTM DEM provides terrain height. The terrain height is added to the PolInSAR derived forest height and LISS IV imagery is draped on the added height. Figure A5.2 shows the 3D image of LISS IV draped over the topographic and vegetation height. The LISS IV image is a FCC, hence red color hues signify vegetation while cyan color depicts urban and dry riverbed areas. The view looks at the Rishikesh City seen as in cyan color. The Barkot forest can be seen, with the forest height above the topographic height. The dry riverbed is seen bordering the Barkot forest range.

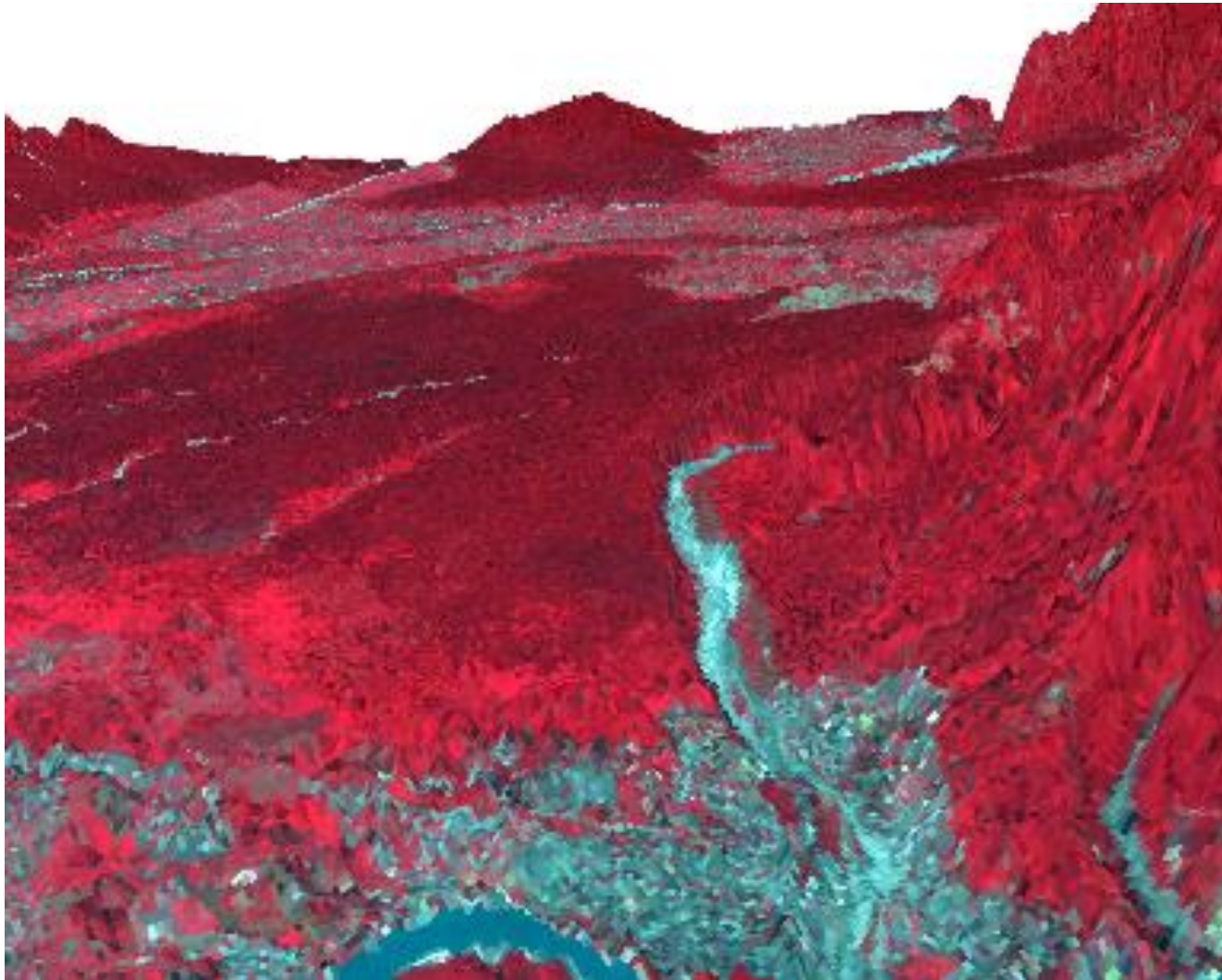


Figure A5.2 Three dimensional view of Barkot forest and Rishikesh City. The LISS IV imagery is overlaid on PollnSAR based forest height and SRTM DEM height

